Advanced optical components for mid-infrared applications

THÈSE N^O 7824 (2017)

PRÉSENTÉE LE 28 NOVEMBRE 2017
À LA FACULTÉ DES SCIENCES ET TECHNIQUES DE L'INGÉNIEUR
LABORATOIRE D'OPTIQUE APPLIQUÉE
PROGRAMME DOCTORAL EN PHOTONIQUE

ÉCOLE POLYTECHNIQUE FÉDÉRALE DE LAUSANNE

POUR L'OBTENTION DU GRADE DE DOCTEUR ÈS SCIENCES

PAR

Grégoire Maxime SMOLIK

acceptée sur proposition du jury:

Prof. C. Moser, président du jury
Prof. H. P. Herzig, directeur de thèse
Prof. B. Lendl, rapporteur
Dr C. Gorecki, rapporteur
Prof. Y. Bellouard, rapporteur

EPFL

ÉCOLE POLYTECHNIQUE
FÉDÉRALE DE LAUSANNE

Suisse
2017

Abstract

The mid-infrared wavelength range, defined from 2.5 µm to 25 µm is of a high scientific and technological interest. One of its main application field is in spectroscopy, since these wavelengths coincide with the fundamental rotational-vibrational modes of many molecules. While the typical optical sensing setup is composed of active elements – detectors and radiation sources – it also requires critical passive components such as lenses, filters and an interface with the medium to be probed. To this day, most of the scientific work in mid-infrared has been mostly focused on active elements such as the quantum cascade laser. While very modern detectors and lasers are now available, the experimental setups still rely on classical and bulky passive optics. The work presented in this thesis explores modern optical technologies for the realization of novel passive mid-infrared optical components. The fabrication of an external cavity tunable quantum cascade laser emitting from 7.6 µm to 8.1 µm is presented. This thesis describes the fundamentals of sub-wavelength structures for optical phase generation. Such structures allow local modifications of the effective refractive index of a dielectric material. Using these concepts, original designs of polarizers, anti-reflective and diffractive micro-optical elements are proposed for high-index dielectrics such as silicon or germanium. In particular, the fabrication and characterization of a novel binary grating in silicon that combines anti-reflective and diffractive functions around 7.85 µm is presented. This component is characterized using the developed tunable light source setup. Another type of optical component is presented, based one dimensional photonic crystals. It consists of a $ZnSe$–YbF_3 multi-layer deposited on top of a CaF_2 substrate. This element allows to observe the first occurrence of Bloch surface waves in the mid-infrared, using the same tunable laser setup. The evanescent field of a surface–propagating wave can be used to probe the surrounding medium. Such structures are promising novel types of substrates for surface–based sensing applications. In addition, a quantum cascade laser–based setup for the detection of cocaine in liquid is presented. This experiment illustrates the great potential of quantum cascade lasers for compact chemical sensing setups.

Key words: mid-infrared; external cavity quantum cascade laser; diffractive optical element; metasurface; Bloch surface wave; mid-infrared spectroscopy

Résumé

Le spectre de l'infrarouge moyen, allant de 2.5 µm à 25 µm, est d'un grand intérêt technique et scientifique. Un de ses principaux champs d'application est la spectroscopie. On trouve dans ce spectre les modes de rotation-vibration fondamentaux de beaucoup de molécules. Un spectromètre ou détecteur optique standard est composé d'éléments actifs – détecteurs et sources – mais également d'éléments passifs tels que des lentilles, filtres ou encore une interface avec le milieu à sonder. À ce jour, la plupart de l'effort scientifique dans ce spectre s'est principalement concentré sur des éléments actifs tels que le laser à cascade quantique. Alors que des composants actifs de dernière génération sont disponibles, les instruments actuels se basent encore sur des éléments passifs anciens et encombrants. Le travail présenté dans cette thèse se concentre sur la réalisation de composants passifs basés sur des technologies optiques modernes. La réalisation d'un laser à cascade quantique accordable à cavité externe émettant de 7.6 µm à 8.1 µm est présentée. Cette thèse décrit également des composants sub-longueur d'onde permettant de réaliser des sauts de phase optique. De telles structures permettent de modifier localement l'indice de réfraction d'un matériel diélectrique. Des concepts originaux de polariseurs, motifs anti-reflets et éléments optiques diffractifs sont proposés sur la base de ce type de structures, destinées à être fabriquées dans des matériaux de haut indice de réfraction tels que le silicium ou le germanium. Plus particulièrement, la fabrication et la caractérisation d'un réseau en silicium combinant des propriétés diffractives et anti-reflets est présentée. Cet élément fonctionne à une longueur d'onde de 7.85 µm. Sa caractérisation est réalisée à l'aide de la plateforme à laser accordable développée. Un autre type de composants est présenté, se basant sur des cristaux photoniques à une dimension. Cet élément est constitué d'un arrangement multi-couches de ZnSe et YbF$_3$ déposés sur un substrat en CaF$_2$. Cet élément permet de réaliser la première observation d'ondes de surface de Bloch dans le spectre de l'infrarouge moyen, entre 7.6 µm et 8.1 µm. La partie évanescente d'une telle onde se propageant à la surface peut être utilisée pour sonder l'environnement extérieur. De tels composants sont un nouveau type d'éléments prometteurs pouvant servir notamment dans le domaine de la détection de surface. Une expérience de détection de cocaine dans un milieu liquide est également présentée. Cette dernière se base sur un laser à cascade quantique, mettant en évidence l'avantage de ces derniers pour la réalisation de dispositifs de détection compacts.

Mots clefs : infrarouge moyen ; laser à cascade quantique à cavité externe ; élément optique diffractif ; métasurface ; onde de surface de Bloch ; spectroscopie infrarouge

Contents

Contents

List of Figures

List of Tables

Acronyms

AR anti-reflective. 15, 16, 17

ATR attenuated total reflectance. 4, 5, 10

BSW Bloch surface wave. 2, 75, 76, 77, 78, 81, 86, 87, 90, 92

CST MWS CST Microwave Studio. 44, 77

CW continuous wave. 5, 19, 20

DBR distributed Bragg reflector. 75

DFB distributed feedback. 3, 4, 5, 13

DOE diffractive optical element. 2, 29, 31, 32, 33, 48, 69

EBL e-beam lithography. 62

EC external cavity. 13, 15, 17, 19, 20, 68

FDFD finite difference frequency domain. 44, 77

FMM Fourier modal method. 25

FP Fabry-Perot. 15, 16, 15, 16, 18, 81, 86, 87

FSR free spectral range. 16

FTIR Fourier transform infrared spectroscopy. 1, 4, 5, 10, 20

GC-MS gas chromatography-mass spectroscopy. 4, 12

GRIN gradient-index. 29

ICP inductively coupled plasma. 62, 63

IPA isopropyl alcohol. 62

MCT mercury cadmium telluride. 5, 19, 68, 81

MEMS microelectromechanical system. 11

MIBK methyl isobutyl ketone. 62

MIR mid-infrared. 1, 2, 3, 4, 11, 21, 31, 32, 41, 42, 48, 72, 75, 77, 90, 92

NIR near-infrared. 1, 31, 75, 90

NMP N-Methyl-2-pyrrolidone. 62

OPL optical path length. 16, 29, 31

PCE tetrachloroethylene. 4, 5, 6, 7, 8, 9, 10, 11, 12

PMMA polymethyl methacrylate. 17, 19

PTFE polytetrafluoroethylene. 5, 7

PV photovoltaic. 81

QCL quantum cascade laser. 1, 2, 3, 4, 5, 10, 11, 12, 13, 16, 15, 16, 17, 19, 21, 28, 31, 32, 68, 69, 81

RCWA rigorous coupled-wave analysis. 14, 21, 25, 27, 28, 34, 35, 36, 37, 38, 41, 44, 48, 54, 58, 60, 62, 69

RIE reactive ion etching. 62, 63, 66

SEM scanning electron microscope. 62, 64, 68, 72, 86

SNOM scanning near-field optical microscopy. 90

SPP surface plasmon polariton. 75, 92

TE transverse-electric. 34, 35, 36, 42, 41, 76, 77, 78, 81, 90

TEC thermoelectric cooler. 16, 17

TIR total internal reflection. 75, 77, 78

TM transverse-magnetic. 14, 34, 35, 36, 37, 42, 41, 54, 76

TMM transfer-matrix method. 26, 27

UV ultraviolet. 31

Introduction

The mid-infrared (MIR) wavelength range, defined from $2.5\,\mu m$ to $25\,\mu m$ is of a high scientific and technological interest. One of its main application field is in spectroscopy, since these wavelengths coincide with the fundamental rotational-vibrational modes of many molecules[1]. This consequently leads to very strong absorption bands, facilitating concentration measurements, as well as identification of molecules. Mid-infrared spectroscopy has a significant potential in label free bio-diagnostics, environmental pollution monitoring, process monitoring, security and defense, as well as research[2, 3].

To this day, most of the scientific work in MIR has been almost exclusively focused on active optoelectronic elements — essentially detectors and radiation sources such as the quantum cascade laser (QCL)[4]. These recent advances along with new diagnostic and treatment approaches such as point-of-care testing are consequently placing new demands on optics. A typical optical sensing setup is composed of a light source, a detector, some passive components such as lenses or filters and another passive element in contact with the medium to be probed. Whereas the experimental setups are based on very modern detectors and lasers, they still rely on classical and bulky passive optics.

The transfer of optical components from the visible to the MIR is however not simply a scaling process, since most materials used in near-infrared (NIR) and visible are not transparent at longer wavelengths and therefore not suitable. Materials such as zinc selenide, silicon or germanium are often used as MIR windows or lenses. Their high refractive index leads to high reflectance. Using these materials for optical parts therefore implies to choose between important reflection losses or the deposition of an anti-reflective coating. The lower demand and need for specific coatings translates in expensive MIR optical elements compared to their visible equivalents. In addition to the higher cost, some specific optical components such as transmission gratings, wave plates or polarizers have scarce commercially available off-the-shelf MIR equivalents.

The first chapter introduces the QCL and an example of its use for the detection of cocaine in liquid. This chapter also describes the realization and characterization of an external cavity setup for a broadband QCL around $7.8\,\mu m$. This tunable laser is the main component of the larger setups used for the characterization of the passive optical devices presented in the following chapters.

In the field of MIR chemical sensing, QCL–based platforms are of great interest as they allow compact and transportable setups compared to Fourier transform infrared spectroscopy (FTIR)[5]. Several applications have been proposed such as the detection of pollutants in the atmosphere and in water, the analysis of blood, saliva or urea of a patient[3]. Another promising emerging technique is QCL–based dual comb spectroscopy[6]. This technique promises high resolution and fast acquisition times, as well as a bright light source.

The second chapter describes the fundamentals of sub-wavelength structures. These structures allow the modification of the effective refractive index of a dielectric material. Using these structures, original designs of polarizers, anti-reflective and diffractive micro-optical elements are proposed for high-index dielectrics such as silicon or germanium.

The third chapter describes the specific design, fabrication and characterization of a novel binary grating in silicon that combines anti-reflective and diffractive functions. The structure is realized in a single lithographic step. The proposed structures are wafer–level micro-optical components, compatible with mass–fabrication.

Quantum cascade laser–based sensing setups could benefit from more efficient and application–specific passive optical components. This problem could be solved by modern optical technologies already successfully implemented at other wavelengths. Among these, the field of micro-optics is particularly interesting. Passive optical devices like digitally coded diffractive optical elements (DOEs) are used for precise illumination control and benefit from small form factors[7]. They require an accurate control of the phase difference along the surface of the optical element. The MIR spectrum allows exploring innovative concepts for phase generation in high-index materials and in metallic structures. In particular, the realization of sub-wavelength elements allowing to artificially modify the refractive index of a medium is of great interest[8]. These elements are easier to fabricate, as their size scales with the long wavelengths. Such elements are also able to control the polarization state of the light, allowing the realization of wave plates and polarizers.

The fourth chapter describes the first observation of Bloch surface waves (BSWs) in the MIR. These surface waves are observed on a QCL–illuminated periodic multi-layer structure, also called one-dimensional photonic crystal.

At the interface of the typical sensing setup lies the element in contact with the substance to be measured. Devices such as absorption cells are common and allow to analyze gases or liquids. The evanescent field of a propagating wave can also be used to probe the surrounding medium, such as in a waveguide[9]. Elements based on surface–wave propagation such as surface plasmons[10] and photonic crystals[11] are also of interest, as they allow new types of substrates for evanescent field sensing. Particularly, BSWs–based structures are good candidates and have been successfully used in the visible[12]. Such structures have so far never been used in the MIR. Combined with a broadband light source such as a tunable QCL, a BSW–based setup would be of great interest for many sensing applications.

1 Methods

1.1 Introduction

This chapter describes the most important tools that are used in the work presented in this thesis. An introduction to the quantum cascade laser (QCL) is given in section 1.2, as well as an example of its use for sensing applications. In particular, a setup for the detection of cocaine in liquid is presented. A broadband tunable QCL setup developed in the frame of this work is described in section1.3, used for the characterization of mid-infrared (MIR) optical components. Finally, the description of a numerical method for the simulation of planar and multilevel gratings is given in section 1.4. This method allows to compute the reflectance, transmittance and diffraction properties of periodic structures.

1.2 Quantum cascade lasers

The first realization of a quantum cascade laser (QCL) was presented by Faist et al. in 1994[4]. Traditional semiconductor lasers emit light based on electron-hole pair recombination from the intrinsic bandgap of the material. The emission wavelength is therefore dependant on the limited materials choice. In the QCL, however, the laser emission results from intersubband transitions between quantum wells. The potential of the quantum wells can be chosen by carefully engineering the multi-layer structure of the laser. The emission wavelength can consequently be chosen at will within a broad range for given materials and is not defined by the intrinsic bandgap[13]. Quantum cascade lasers are therefore able to emit light in spectral range unavailable for usual semiconductor lasers. In particular, QCLs emitting in the MIR range and THz have been demonstrated [14, 15, 16].

In the MIR range, such a light source is of great interest thanks to multiple interesting properties. The addition of a distributed feedback (DFB) to the QCL allows a narrow emission linewidth[17]. The thin emission linewidth of a DFB QCL is of great interest for gas phase and other spectroscopic applications[18, 19, 20]. Another interesting property is the high spectral power density of the QCL. This allows to use them for liquid phase spectroscopy,

where the background absorption is usually high and reduces the possible path length[21]. Continuous wave operation at room temperature allows to build compact setups using QCL light sources[22]. These are of particular interest for the realization of portable devices for in situ sensing and monitoring.

In the following section, the use of a DFB QCL in a custom setup for the detection of trace amounts of cocaine in liquid phase is presented. This example shows the benefits of a QCL for the realization of compact spectroscopic systems.

1.2.1 Liquid phase sensing using quantum cascade lasers

In the frame of the Nano-Tera initiative funded by the Swiss National Science Foundation, a project named IrSens was conducted between different partners and institutions in Switzerland[3]. The aim of this project was to develop and build cost-effective and reliable platforms for optically-based liquid and gas spectroscopy. Concerning the liquid spectroscopy, the detection of cocaine in saliva was selected for the realization of a proof of concept demonstrator. The ideal detector would be able to make fast quantitative measurements of this analyte and be portable. This would allow measurements similar to sideroad blood alcohol content verifications operated by law enforcement. Current methods for measuring cocaine are principally based on immunoassays[23][24], which only provide qualitative results. When a positive result is obtained, the blood or saliva samples need to be further analyzed by gas chromatography-mass spectroscopy (GC-MS) for confirmation[25]. While being the state of the art technique for forensics applications, GC-MS is not portable and requires complicated and time-consuming sample preparation[26]. Precise quantitative on-site testing would therefore be of great interest for forensics and law enforcement.

Since the composition of saliva depends on the substances (food, liquids, drugs) absorbed by the subject, a precise and reliable measurement of an analyte in saliva is a complicated task[3]. Saliva also contains water, a liquid that strongly absorbs in the MIR. A microfluidic platform has been developed at EPFL[27]. Its purpose is to extract cocaine from saliva and mix it with tetrachloroethylene (PCE), a transparent solvent in the MIR. This approach provides a robust platform, avoiding the drawbacks of direct in-saliva sensing. By carefully controlling the flow rates of saliva and PCE in the microfluidic platform, it is possible to achieve extractions ratios higher than 100%, corresponding to an actual pre-concentration of cocaine in PCE. The microfluidic platform is combined with a MIR germanium waveguide[28]. A QCL is coupled into the waveguide and the interaction of the evanescent field at the waveguide interface with the surrounding liquid is measured. This combined setup is used to detect cocaine and reaches a limit of detection of $500\,\mu g/ml$ of cocaine in saliva, extracted in PCE. Using a different fluidic circuit, the germanium waveguide is used to measure PCE in which pure cocaine powder was directly added, without extraction from saliva. This second setup reaches a detection limit of $100\,\mu g/ml$ of cocaine in PCE[9].

In parallel, the optical detection of cocaine directly in saliva using attenuated total reflectance

(ATR) Fourier transform infrared spectroscopy (FTIR) was investigated. A detection limit of $20\,\mu g$/ml of cocaine in saliva was demonstrated[29]. Using an extraction step in PCE, a detection limit of $1.3\,\mu g$/ml of cocaine in saliva could be reached[26].

In this section, we present a method that reaches a detection limit of $1.35\,\mu g$/ml of cocaine in PCE. This value is comparable to the detection achieved by FTIR but benefits from a more compact setup which could allow it to be used on–site. This work was presented at the OSA Optical Sensors conference in 2014 in Barcelona[30].

1.2.2 Development of a platform for cocaine detection in liquid

Liquid medium The selected solvent for the preparation of the cocaine solution is PCE, a solvent commonly used in dry cleaning and spectroscopy. It has a broad transmission window in our region of interest and dissolves well cocaine[27]. Figure 1.1a shows the transmission spectrum of an ATR crystal in contact with a solution of $10\,mg$/ml of cocaine in PCE measured with a Bruker Vertex 70 spectrometer.

Light source We target the carbonyl resonance of cocaine at $1720\,cm^{-1}$, as described in figures 1.1a and 1.1b. This particular resonance provides small cross-talk with other potentially interfering species [29]. The light source used is a single mode DFB QCL operating in continuous wave (CW) fabricated especially for this purpose at ETH Zurich (Switzerland). The emission wavelength of the laser is spectrally aligned with the cocaine absorption band by adjusting its operating current and temperature.

Absorption cell The custom absorption cell used in this experiment is described in figure 1.2. It is realized using a bent stainless steel capillary. The capillary is connected on the input end by a polytetrafluoroethylene (PTFE) tube to a fluidic switch controlling the liquid source. The output end is connected to a waste collection bottle by another PTFE tube. Two chalcogenide mid-infrared fibers are attached through the capillary and act as windows for the sensing light. The interaction length between the fibres inside the cell is $15\,mm$ and the cell volume is approximately $3\,\mu l$.

Setup

The collimated QCL output is modulated using a mechanical chopper for homodyne detection. The light is then focused on the front facet of the input fibre using a 15X/0.28NA gold coated reflective microscope objective. The light propagates inside the cell where it interacts with the liquid and exits through the output fibre. A VIGO PV-8 photovoltaic mercury cadmium telluride (MCT) detector collects the light exiting the output fibre. The signal from the photodetector is amplified by a SRS SR570 current amplifier and sent to a SRS SR830 lock-in amplifier.
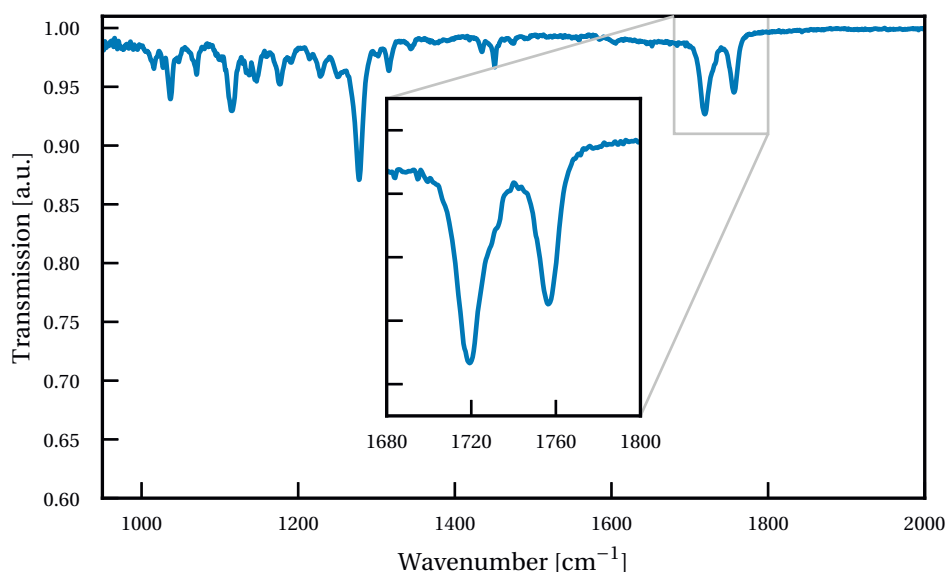
(a) Cocaine transmission spectrum
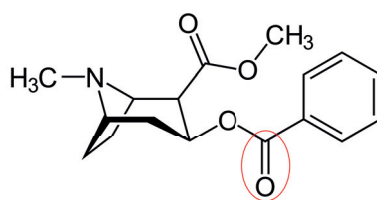
(b) Cocaine chemical structure

Figure 1.1 – (a) Transmission spectrum of a solution of 10 mg/ml of cocaine in PCE measured by ATR FTIR with a Bruker Vertex 70 spectrometer. The inset highlights the targeted carbonyl resonance at 1720 cm^{-1}. (b) Chemical structure of cocaine with the targeted carbonyl group circled.

Two bottles are filled with pure PCE and a solution of cocaine in PCE, respectively. They are connected to the fluidic switch with PTFE tubes. The bottles are pressurized by connecting them to a nitrogen circuit. Once under pressure, the liquid selected by the switch starts flowing from the bottle through the cell. The liquid source can be switched between the reference PCE and the cocaine solution at will.

Operating principle

The signal from the lock-in amplifier is recorded over time as the pure PCE flows through the cell. The source is switched to the cocaine solution for a specific amount of time and then switched back to the pure PCE bottle. After some delay depending on the flow rate and the length of the tube, the cocaine solution reaches the cell and the signal from the detector decreases. The decrease of the signal can be linked to the absorption happening in the cell
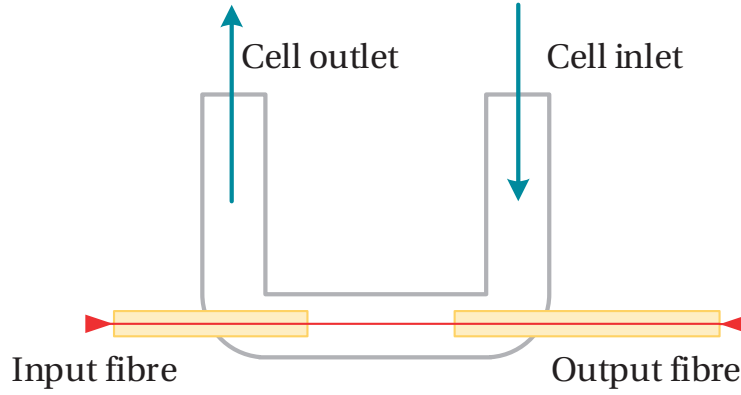
Figure 1.2 – Schematic of the absorption cell consisting of a bent stainless steel capillary with chalcogenide input and output fibre acting as windows. The path length between the fibres is 15 mm and the cell volume is 3 μl

.

through Beer-Lambert's law:

$$I(\lambda, x) = I_{in}(\lambda) \cdot e^{-\alpha x},$$

where I is the intensity of the light at the output of the cell, I_{in} is the intensity of the light at the input of the cell, α is the absorption coefficient and x is the optical path length in the cell. Assuming that I_{in} and x are constant through all the measurements, the only factor affecting the output intensity is the absorption coefficient α, directly proportional to the analyte concentration. The absorption coefficient is also wavelength dependent. The Beer-Lambert's law can therefore be rewritten as

$$\epsilon \cdot C \cdot x = -\log_{10}\left(\frac{I}{I_0}\right),$$

where $\frac{I}{I_0}$ is the transmittance of the cell, ϵ is the absorption coefficient of the analyte at a specific wavelength and C is the concentration of the analyte in the solution[31]. At the resonance wavelength, the light intensity at the output of the cell is therefore expected to decrease exponentially with an increase of cocaine concentration. The intensity measured while the pure PCE is flowing through the cell serves as a reference value. The intensity drop resulting from cocaine absorption is then compared to this reference value.
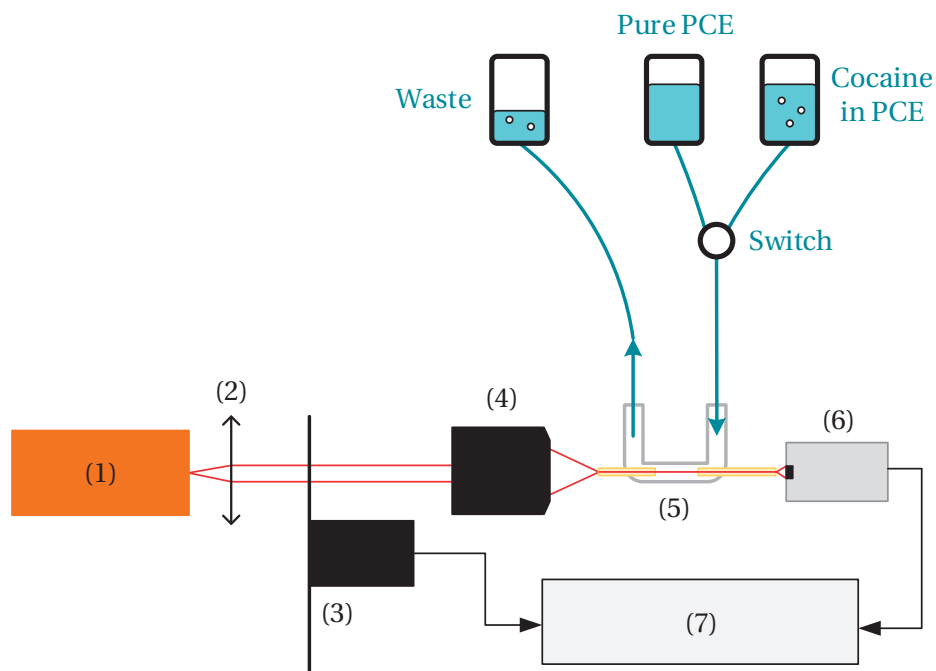
Figure 1.3 – Schematic of the setup with (1) QCL operating at $1719.6 \, \text{cm}^{-1}$, (2) collimation lens, (3) chopper, (4) 15x/0.28NA reflective microscope objective, (5) absorption cell, (6) VIGO PV-8 photovoltaic MCT detector connected to SRS SR570 current amplifier and (7) SRS SR830 lock-in amplifier.

1.2.3   Results

Sample preparation

For this experiment, a highly concentrated solution is prepared using cocaine powder weighed with a precision scale mixed with PCE. From this main solution, different concentrations of cocaine are obtained by different levels of dilution. The pure PCE bottle is filled once for the whole experiment, while the bottle containing the cocaine solution is exchanged for every measured concentration. The PTFE tube connecting the cocaine solution bottle to the switch is flushed with pure PCE between two different concentration measurements.

Measurements

The intensity signal at the output of the cell is recorded over time. At some point, the source of liquid is switched from the reference PCE to the cocaine solution for 120 s and then switched back to the reference. Figure 1.4 shows the intensity at the output of the absorption cell over time when a solution of 25 µg/ml of cocaine in PCE flows through the cell. The intensity starts to decrease approximately 80 s after the source is switched to the cocaine solution. This delay
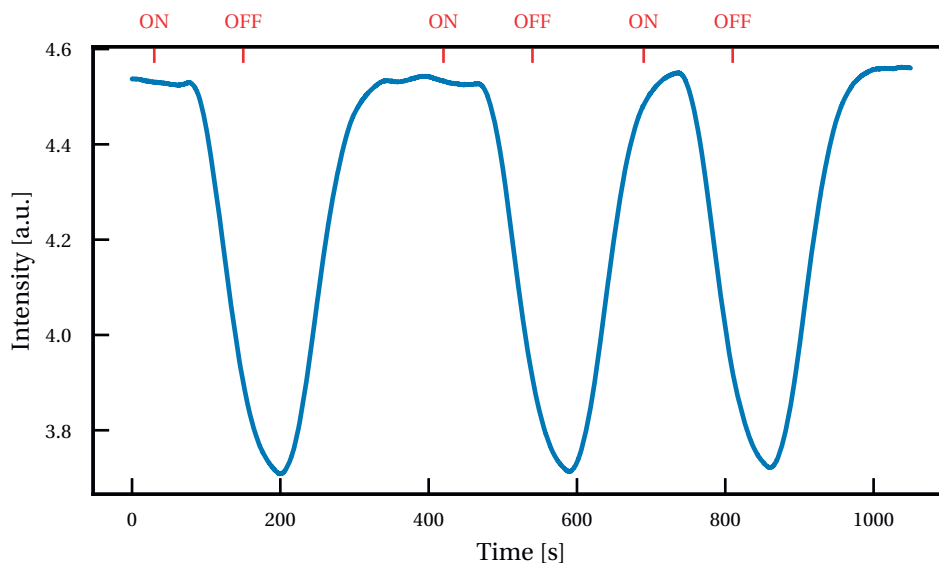
Figure 1.4 – Light transmission of the absorption cell with a solution of 25 μg/ml of cocaine in PCE. The ON and OFF ticks show the instant at which the switch selects the cocaine solution and the PCE reference, respectively.

results from the time required for the cocaine solution to reach the cell. The intensity drop is not immediate, due the integration time of the lock-in amplifier. Another factor impacting the slope of the signal is the dispersion taking place inside the tubes from the cocaine solution into the pure PCE while it is being transferred to the absorption cell. The cocaine concentration is therefore not constant during the whole measurement. The flux of liquid needs to be fast enough for the cocaine solution to reach the cell before too much diffusion occurs. The cell transmission reaches a plateau, which is used as the minimum transmission value for the corresponding concentration. In the calibration phase, the cocaine solution is allowed to flow in the cell for a longer time, in order to determine the minimum time required to reach the plateau. Once this value is determined, the subsequent measurements are made with a flowing time of the cocaine solution as short as possible.

Figure 1.5 compares the signal obtained with an integration time of 3 s on the lock-in amplifier for three solutions of, respectively, 1 μg/ml, 25 μg/ml and 50 μg/ml of cocaine in PCE. As expected, the minimum of light transmission in the cell decreases with higher cocaine concentrations.

The minimum of transmission I_{min} attained is compared to the reference signal I_{ref} when pure PCE is flowing in the cell for every different concentration. Figure 1.6 shows the absorbance $\log(I_{min}/I_{ref})$ for various concentrations of cocaine. The ratio diminishes with increasing concentrations following an exponential curve, as expected from Beer-Lambert law. Concentrations down to 62.5 ng/ml were measured but no signal drop could be reliably discerned
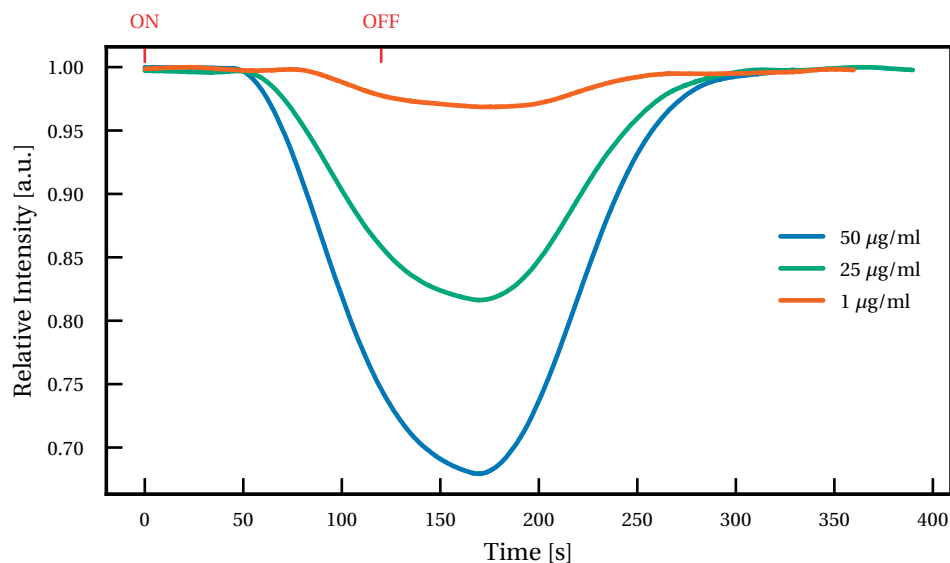
Figure 1.5 – Light transmission of the absorption cell with three different concentrations of cocaine in PCE. For every concentration, the cocaine solution is switched ON for 120 s and then switched back to pure PCE.

from noise under a concentration of 250 ng/ml. At such small concentrations, the dispersion of cocaine in solution in the surrounding of pure PCE becomes too important. A limit of detection of $1.35\,\mu g\,ml^{-1}$ of cocaine in PCE can be derived from the regression line displayed in figure 1.6.

Flow rate incidence

We could observe that a low flow rate of the fluid in the tubes produced a noisy signal as well as a weak absorption dip. The time required for the cocaine solution to reach the cell is also consequently longer. Figure 1.7 shows the measured signal for various flow rates of cocaine solution in the cell. The flow rate can be increased by augmenting the pressurization applied to the bottles. As it can be observed on this figure, when the flow rate is high enough, in this case about $0.187\,ml\,min^{-1}$, the signal keeps its amplitude and the only effect of an increase of flow rate is a faster response time. It is therefore important to keep the flow rate constant over the whole measurements to get comparable results. It is also important to have a high enough flow rate so that the concentration is as close as possible to the initial value.

1.2.4   Outlook

The current results are very encouraging. They offer almost two orders of magnitude improvement in comparison with evanescent field sensing through a germanium waveguide
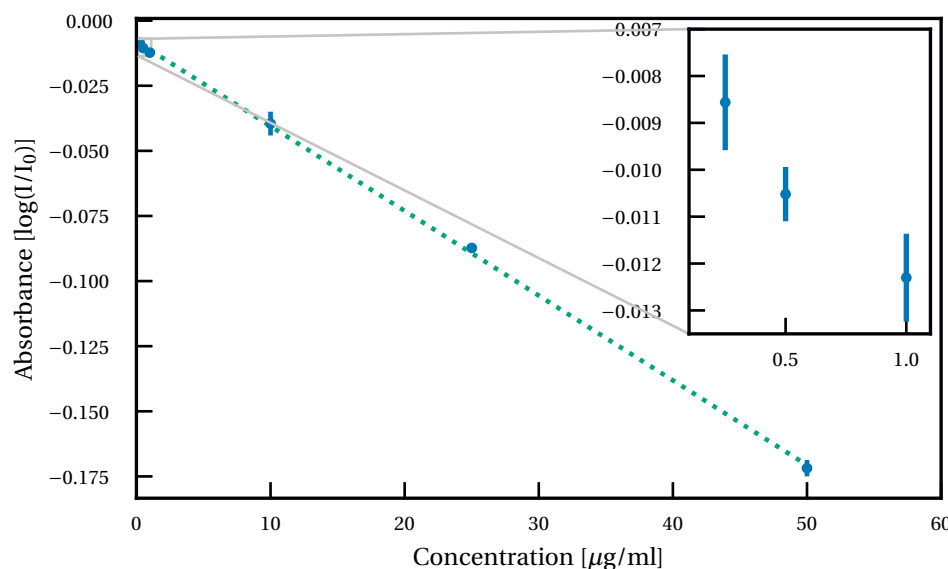
Figure 1.6 – Absorbance (log(I/I_0)) as a function of cocaine concentration in PCE.

using a similar QCL source[9]. They also provide comparable performances with ATR FTIR measurements[32], using a more compact setup. However, the current system suffers from some limitations that can be improved.

Laser source   The QCL used was designed to operate at $1720\,\mathrm{cm}^{-1}$. Unfortunately, its actual emission was closer to $1730\,\mathrm{cm}^{-1}$, slightly off the targeted absorption peak of cocaine, as shown in figure fig:cokeinpce. The emission wavelength can be tuned within a small range by modifying the operating temperature or operating current of the laser. We were able to spectrally align the QCL to the desired wavelength by heating it to $37\,°\mathrm{C}$. Unfortunately, the emission of a QCL diminishes with increased operating temperature which resulted in a rather weak laser output power of $290\,\mu\mathrm{W}$. Another source of noise coming from the laser is the output power fluctuation. The laser was not equipped with any sort of output regulation except for temperature control. Any power variation directly impacts the output signal of the cell. This source of noise can be reduced by actively controlling the laser output power. Another way to mitigate the power fluctuations is to add a beam splitter in the optical path to sample the laser output, such as the device presented in chapter 3. The measured signal can then be corrected accordingly in real time. Considering selectivity, a single wavelength measurement can hardly give specific results. The presence in the liquid of other substances with overlapping absorption bands could lead to erroneous results. It could be beneficial to use a broadband tunable laser such as described later in section 1.3, which could help to precisely identify the target molecule.
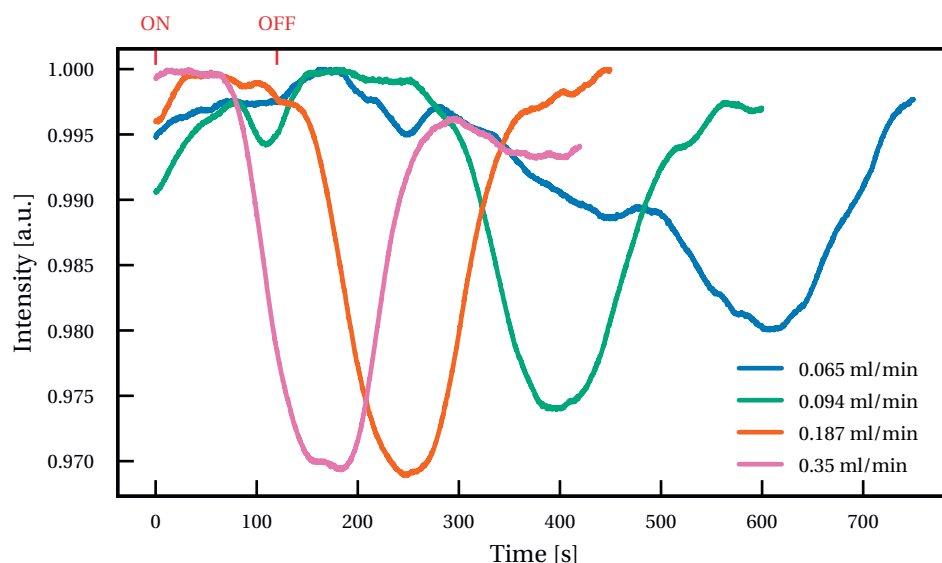
Figure 1.7 – Recorded signal over time for different flux and a concentration of $25\,\mu g/ml$ of cocaine in PCE. When the flux is lower, the cocaine diffuses in the surrounding pure PCE resulting in a weaker signal as well as a longer delay.

Optical path   An important fraction of the laser output is lost while coupling it into the input fibre of the cell. The QCL chip could be directly fibered. This would allow a direct coupling from the laser to the absorption cell. The modulation required for synchronous detection can be provided by an amplitude modification of the laser current or by adding a fibered microelectromechanical system (MEMS) switch[33]. The MEMS switch could also be used for the laser output sampling, replacing a beam splitter. A fully fibered setup would also provide more stability to the signal. The current setup is indeed very sensitive to the surrounding environment and fluctuations of the output signal can be observed. While transparent in the MIR, PCE still absorbs some of the light, which limits the maximum path length inside the cell. A laser source with higher power could allow for a longer interaction path in the absorption cell, enabling better sensitivity.

Fluidic circuit   It was observed that the flow rate has an impact on the measurements and should be precisely controlled. The fluidic path between the reservoirs and the absorption cell should also be reduced. This would limit the dispersion of cocaine happening within the tubes before reaching the cell and would also reduce the response time of the sensor. The volume of analyte solution required for the measurement could therefore also be reduced.

1.2.5 Summary

We demonstrated the feasibility of a direct absorption based optical sensor for the detection of cocaine in liquid phase using a QCL. The current setup provides an improvement of the detection limit by about two orders of magnitude compared to the previous record with a similar laser source [9]. We reached a detection limit of 1.35 µg/ml of cocaine in PCE. This result is comparable to the value obtained by [26]. This detection limit is however two to three orders of magnitude larger compared to established measurement techniques such as GC-MS capable of sensing several ng/ml, but close to actual concentrations found in drug users[26]. The setup is also considerably smaller than a typical GC-MS instrument and can be portable.

As mentioned previously, a drawback of a DFB QCL in such measurements is its lack of specificity. A laser such as the one used in this experiment can be tuned by a few tens of nanometers around the central wavelength by modifying its operating temperature. It is preferable to be able to detect multiple specific absorption peaks to correctly identify the substance. Unfortunately, these other absorption bands are likely to be outside of the narrow emitting range of a DFB QCL. It is therefore difficult to make specific measurements using only one such laser. It is possible to use multiple lasers combined on the same chip, extending the range of detection[34]. Another possibility is to use a tunable laser, which is specifically designed for a much broader range of operation. The following section describes the design and fabrication of a tunable QCL setup.

1.3 External cavity quantum cascade laser

Thanks to the broad gain mediums achievable by design, the emission wavelength of QCLs can be tuned over a large spectral range using an external cavity (EC) setup. The first EC tunable QCL was reported by Luo et al. in 2001[35]. In this paper, the tunable range of the laser is reported to be $34\,\mathrm{cm}^{-1}$ around $5.1\,\mu\mathrm{m}$ at an operating temperature of $80\,\mathrm{K}$. A broadband tuning range of $150\,\mathrm{cm}^{-1}$ around $10\,\mu\mathrm{m}$ was reported by Maulini et al. in 2004[36]. More recently, in 2014, a QCL with a $303\,\mathrm{cm}^{-1}$ tunability range around $8\,\mu\mathrm{m}$ has been reported[37].

1.3.1 Principle

External cavity

An electromagnetic wave incident on a reflection grating is diffracted in multiple waves at various angles. The grating equation (1.1) gives the angle of the maxima of the reflected diffraction orders, where d is the line spacing or period of the grating, θ_i the incidence angle of the wave with respect to the normal of the grating surface, θ_m the angle of the diffracted beam, m is an integer that represents the order of the diffracted beam, λ_0 the vacuum wavelength of
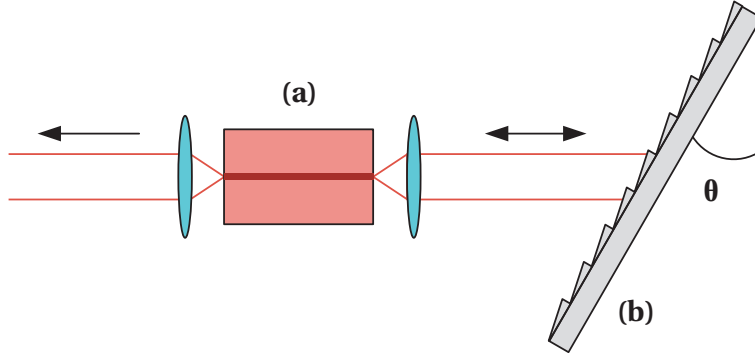
Figure 1.8 – Littrow tunable laser configuration with (a) gain medium and (b) blazed grating. The black arrows indicate the direction of light propagation. The tuning of the output wavelength is achieved through the modification of the angle θ of the grating.

the light and n the refractive index of the surrounding medium

$$d\left(\sin\theta_i + \sin\theta_m\right) = m\frac{\lambda_0}{n}. \tag{1.1}$$

This equation gives the following values for maxima angles:

$$\theta_m = \arcsin\left(\frac{m\lambda_0}{dn} - \sin\theta_i\right). \tag{1.2}$$

The external cavity setup is realized using a Littrow configuration, described in figure 1.8. The gain medium is coated on the grating end with an anti-reflective coating and left uncoated on the output end. In this configuration, the first-order diffracted beam on the grating is reflected back into the laser cavity, the incident and diffracted angles must therefore be equal. This constrains equation (1.2) and gives the following relationship between the incident angle, the wavelength and the grating period

$$\theta = \arcsin\left(\frac{\lambda_0}{2dn}\right). \tag{1.3}$$

Using a so-called blazed grating, it is possible to maximise the percentage of light diffracted in the first order and minimise the power in all other orders. The blazed grating in the Littrow configuration possesses a saw tooth profile in which the angle between the tilted surfaces and the grating surface matches the incident angle. The incident light is therefore perpendicular to the tilted surfaces. This combines the reflected and first-order diffracted waves which yields a higher efficiency compared to a binary grating where a lot of light is diffracted into the zero order. Figure 1.9 illustrates the geometry difference between a binary and a blazed grating and an example of the changes in efficiency between these two types of gratings is given in table 1.1. The efficiencies are simulated using rigorous coupled-wave analysis (RCWA)[38, 39, 40, 41, 42],

Table 1.1 – Comparison of the reflection efficiency of metallic binary grating and blazed grating at 7.8 μm wavelength with 35° incidence angle, 6.8 μm grating period and 3.2 μm grooves depth in transverse-magnetic (TM) polarization. The simulation is made by RCWA.

Grating type	Zero order efficiency	First order efficiency
Binary	82.43 %	13.62 %
Blazed	2.29 %	94.01 %

(a) Binary grating   (b) Blazed grating
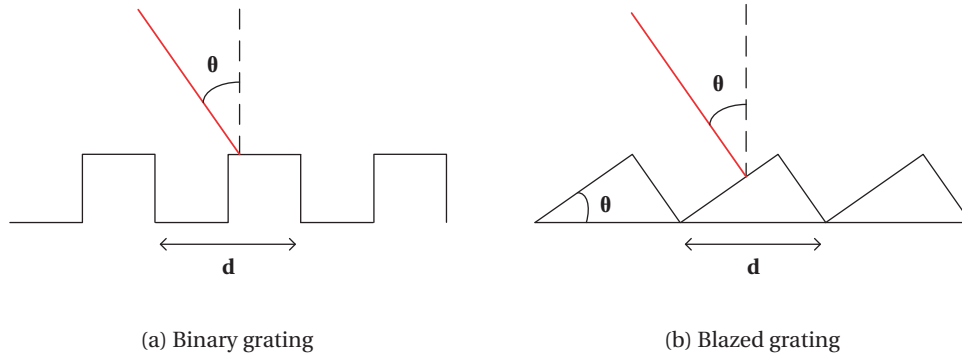
Figure 1.9 – Comparison between (a) binary grating and (b) blazed grating geometries in Littrow configuration, where d is the grating period and θ the blaze angle, equal to the incident angle and first-order diffracted angle.

a method described later in section 1.4.

Tunability

The wavelength tuning of the laser is realized through the rotation of the grating. This modifies the incident angle on the grating. Assuming that $n = 1$, rewriting equation (1.3) yields the following relationship between the wavelength and the grating angle:

$$\lambda_0 = 2d \sin\theta. \tag{1.4}$$

The laser output wavelength can therefore be selected by a simple rotation of the grating. The achievable spectrum of emission depends principally on the gain medium used. The grating period and blaze angle are chosen for maximum efficiency around the emission spectrum of the gain medium.

Mode hopping

Because of the multiple Fabry-Perot (FP) resonances present on the tunable laser setup, it is expected that mode hopping occurs. The main FP resonances are described in figure 1.10. The
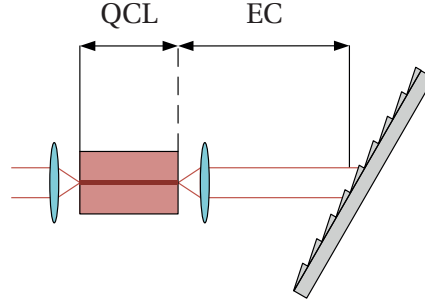
Figure 1.10 – Fabry-Perot cavities present in the tunable QCL setup. The internal FP cavity of the laser chip is labelled QCL and is 3 mm long. The external FP cavity of the setup is labelled EC and is 120 mm long.

internal FP cavity is bound by the two facets of the 3 mm long QCL chip. The external FP cavity is bound by the grating and the anti-reflective (AR) coated facet of the QCL and is 120 mm long. The two cavities are coupled. If the influence of FP resonance is too important, the laser output wavelength does not follow equation (1.4) but stays locked on the same FP resonance for a short range of grating angles. In this case, a continuous and precise tuning of the laser wavelength is not possible and the output wavelength jumps between the modes allowed by the FP resonances. This effect can be cancelled by actively moving the FP resonances together with the grating angle[43]. The chip FP resonance can be modified by changing the current, which changes the temperature and the optical length of the chip. The FP resonance of the EC can be modified by changing the length of the EC. The strength of the internal cavity FP strongly depends on the reflectivity of the AR coated facet. A good quality AR coating suppresses the internal cavity FP mode hops[13].

The free spectral range (FSR) between the FP peaks or can be approximated by

$$\Delta\lambda \approx \frac{\lambda_0^2}{2nl\cos\theta},$$ (1.5)

with λ_0 the vacuum wavelength, n the refractive index of the medium inside the cavity, l the cavity length and θ the incidence angle[44]. In this case, θ is equal to 0 (normal incidence). The optical path length (OPL) of the internal and external cavities are 9.6 mm and 120 mm, respectively. At a wavelength of 7.8 μm, the FSR of the internal and external cavities are 3.167 nm and 0.253 nm, respectively.

1.3.2 Setup description

The complete setup is illustrated in figure 1.11 and the main components are described in the following paragraphs.
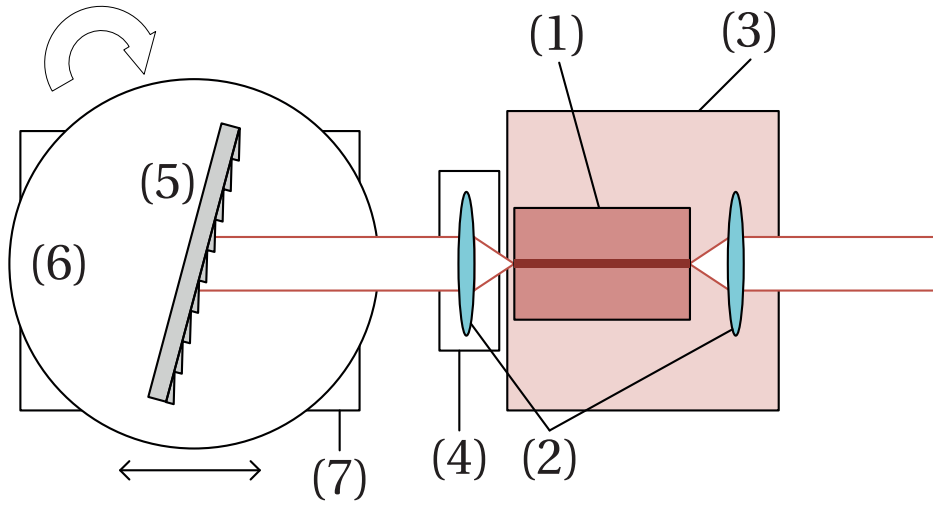
Figure 1.11 – External cavity tunable QCL setup: (1) QCL chip on copper mount; (2) collimation lenses; (3) copper heatsink on top of thermoelectric cooler (TEC) element; (4) piezoelectric–actuated 3-axis stage for lens alignment; (5) diffraction grating; (6) motorized rotational stage; (7) motorized linear stage.

Gain medium

The QCL chip is provided by Alpes Lasers S.A. (Switzerland). It is designed to have a broad gain spectrum around $1270\,\mathrm{cm^{-1}}$. The initial laser characteristics before deposition of the AR coating show emission from $1250\,\mathrm{cm^{-1}}$ to $1340\,\mathrm{cm^{-1}}$ at an operating temperature of $-30\,°\mathrm{C}$ in pulsed operation. The bandwidth is reduced from $1260\,\mathrm{cm^{-1}}$ to $1300\,\mathrm{cm^{-1}}$ at $0\,°\mathrm{C}$. After application of the AR coating on one facet, the bandwidth is further reduced from $1270\,\mathrm{cm^{-1}}$ to $1310\,\mathrm{cm^{-1}}$ at $-30\,°\mathrm{C}$.

Temperature control

The QCL is designed for operation at sub-zero temperatures. The chip must therefore be cooled and its temperature controlled. We achieve this by using a TEC device between the chip holder and a heatsink. Both chip holder and heatsink are made of copper, chosen for its high thermal conductivity. A water chiller pumps cold water at $5\,°\mathrm{C}$ through the heatsink.

Since the operating temperature of the laser is below $0\,°\mathrm{C}$, condensation and ice can form on the chip and its holder in a humid environment. Water and ice deposition on the chip can damage or destroy it. The setup is therefore enclosed in an air-tight polymethyl methacrylate (PMMA) frame filled with nitrogen. In order not to alter the EC feedback, the whole setup is enclosed, including the grating and its stage.

Lens alignment

The lenses used for collimation of the laser output and feedback are molded aspherical lenses with 0.85NA, 1.873 mm focal length and 4 mm clear aperture. The lenses are AR coated. Since the enclosed setup offers no direct access for manual control of the feedback lens alignment, we use a P-611.30 piezoelectric actuated stage from Physik Instrumente (PI). The stage has a range of 100 μm and a resolution of 100 nm in all three axes. The output lens is glued on a holder.

Current source

The current source is a QCL1500 driver from Wavelength Electronics. It provides ultra low noise current control and the ability to modulate the current from an external reference.

External cavity length control

The length of the external cavity can be modified using a M-110.1DG motorized linear stage from PI. The stage has a range of 5 mm and a resolution of 50 nm.

Grating angle control

The grating is mounted on a 8MR191-28 motorized rotational stage from standa. The stage is equipped with a stepper motor that gives a resolution of 0.01° per step. The motor can be moved in 1/8 steps to increase the resolution.

1.3.3   Characteristics

Resolution

The spectral position of the laser output depend on the angular resolution of the grating position. Using equation (1.4) and knowing the angular resolution of the rotational stage, the wavelength steps can be calculated. Using the stepper motor in full or 1/8 steps, the resolution at 7.8 μm wavelength is 1.887 nm or 0.236 nm, respectively.

Spectral precision

The grating can be considered as a filter with a specific bandwidth[43]. The bandwith of the grating is given by

$$\Delta\lambda = \frac{\lambda_0 d \cos\theta}{a},$$
(1.6)

where d is the grating period and a the beam width on the grating. In our system, the estimated bandwidth is 10.54 nm or 7.73 cm^{-1}. The strongest FP resonance of the combined internal and external cavities within that bandwidth can be the lasing mode of the laser. The grating bandwidth is therefore a worst estimate of the spectral precision of the laser. Since the bandwidth is larger than the resolution calculated in the previous section, it is possible that the lasing mode and therefore the wavelength stays constant for a range of grating angles until a new mode is preferred. This mode hopping diminishes the accuracy of the laser wavelength.

1.3.4 Measurements

Pulsed operation

The EC setup is initially assembled outside of its PMMA enclosure for practical reasons. Originally, the QCL chip is designed for CW operation at sub-zero temperatures. However, at such temperatures, the setup is subject to condensation or deposition of water present in the atmosphere. To avoid this effect, the initial alignment of the EC grating and collimation lens is realized at room temperature. At this temperature, the QCL chip does not emit light in CW but pulsed operation is possible for short pulse widths. Figure 1.12 represents the output intensity of the laser in EC configuration as a function of the grating angle. The laser is driven with 12 V pulses of 100 ns width at 200 kHz repetition rate. Using the grating equation (1.4), the emission spectrum is determined to range approximately from 6.90 μm to 8.15 μm or 1225 cm^{-1} to 1450 cm^{-1}.

Once the external cavity grating is aligned, the output collimation lens is fixed and the setup can be sealed by the PMMA enclosure filled with nitrogen. A hygrometer placed inside the enclosure helps to determine if the setup is in an environment dry enough to be cooled down without any risk of condensation. Figure 1.13 shows the effect of increased operation temperature on the output power of the laser. For these measurements, the laser is driven with 12 V pulses of 100 ns width at 200 kHz repetition rate. The grating is set at an angle of 36.423°, for which the measured output intensity is the highest. One can observe a decrease of the average output power by 25% between −15 °C and 20 °C. This decrease of performance with increased operating temperature can also be observed in figure 1.14, where the output power of the laser is measured as a function of the pulse voltage at different temperatures. It can be observed that the lasing threshold voltage, around 8.5 V, increases with temperature.

Figure 1.15 represents the output power in pulsed operation at −15 °C for different duty cycles. The pulse width being fixed at 100 ns, the duty cycle is increased through a higher repetition rate. The lasing threshold voltage is stable for all duty cycles. It can be observed that for higher duty cycles, the output power does not increase linearly with applied voltage anymore, due to heating of the laser.
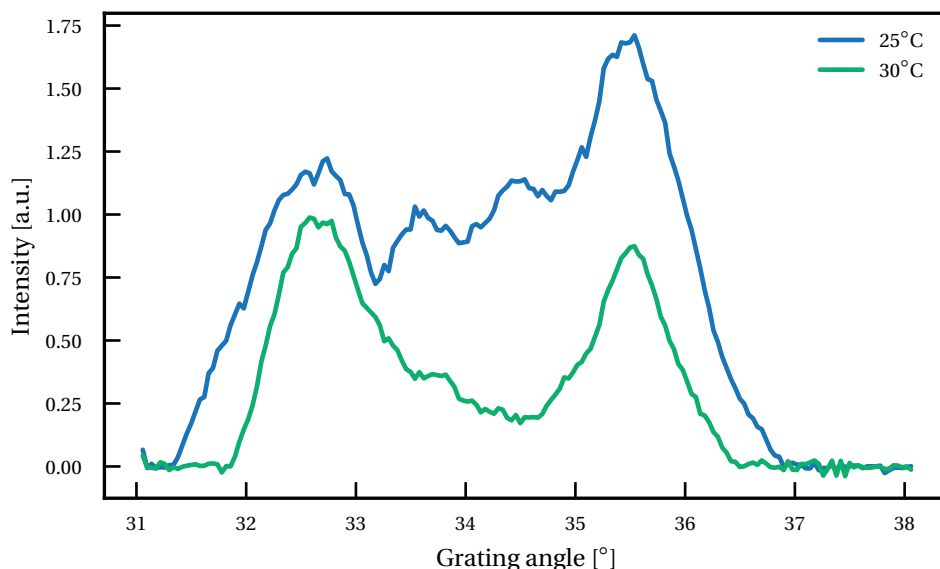
Figure 1.12 – Laser output intensity at different temperatures in pulsed operation with 2% duty cycle, 200 kHz repetition rate (100 ns pulse width), 12 V operating voltage. The intensity is measured with a Vigo PV-8 photovoltaic MCT detector at the output facet of the laser. A lock-in amplifier with a chopper positioned inside the external cavity are used for homodyne detection. The grating is rotated during the measurement to evaluate the emission spectrum.

Continuous wave operation

The laser output is characterized in CW operation with a grating angle at 36.423°. Figure 1.16 shows the output power of the laser at different operating temperatures as a function of operating current. Compared to pulsed operation described in figure 1.15, the laser output is much more affected by the operating temperature. In pulsed operation, the output power suffers a drop of roughly 4% going from $-15\,°C$ to $0\,°C$ whereas in CW operation, the drop reaches 60%. As in pulsed operation, the decrease in output power is related to the laser heating.

The output intensity is measured as a function of the grating angle at an operating temperature of $-20\,°C$. Figure 1.17 shows the resulting emission spectrum obtained for different operating currents. Using the grating equation (1.4), the emission spectrum is determined to range approximately from $7.55\,\mu m$ to $8.25\,\mu m$ or $1215\,cm^{-1}$ to $1320\,cm^{-1}$. Compared to the pulsed emission range, the CW range is approximately halved and slightly red-shifted.

The actual emission spectrum is then measured using a Bruker Vertex 70 FTIR spectrometer. For this measurement, the laser operates at $-13.5\,°C$ and is driven by a 0.6 A current. Figure 1.18 shows the resulting spectra obtained.

Figure 1.13 – Collimated laser output power at 2% duty cycle, 200 kHz repetition rate (100 ns pulse width), 12 V operating voltage for different operating temperatures. The EC grating angle is selected for maximum output power. The laser is enclosed in a sealed PMMA box under nitrogen atmosphere to avoid water condensation.

Mode hopping

The spectra displayed in figure 1.18 can be matched to the grating equation to determine the spectral accuracy of the laser output wavelength. Figure 1.19 shows the difference between the theoretical wavenumber given by the grating equation (1.4) and the actual FTIR measurement. The largest difference measured is $1.37\,\mathrm{cm}^{-1}$ or 8.79 nm, which is within the calculated bandwidth of the grating.

1.3.5 Summary

An external cavity setup for broadband QCL emission has been presented. The setup emits linearly polarized light from 7.55 µm to 8.25 µm. Such lasers are of great interest for spectroscopic applications but also simply as MIR light sources. The setup presented here is used for the optical characterization of MIR optical elements, taking advantage of the linearly polarized output, low divergence and high power spectral density.

The following section introduces the RCWA method, used for the simulation of the optical properties of periodic structures.
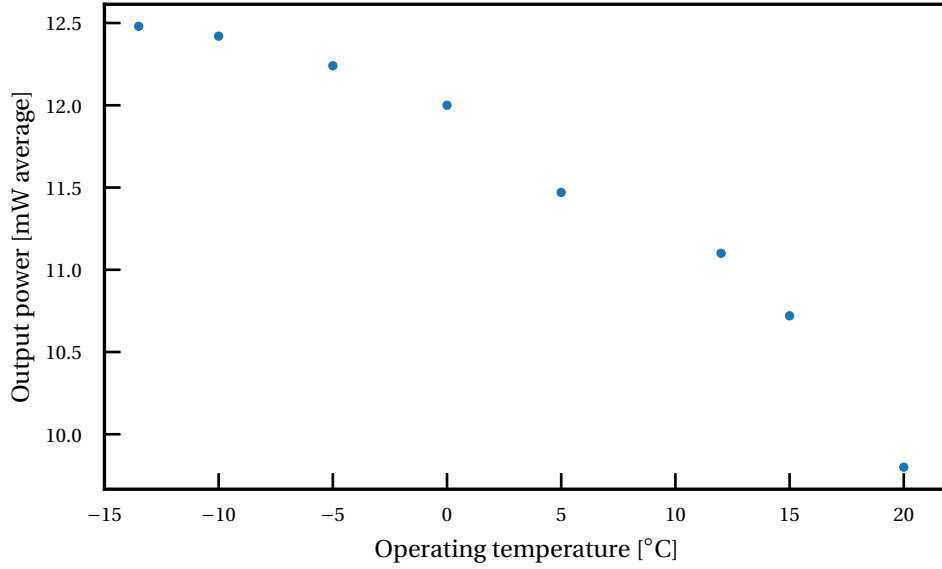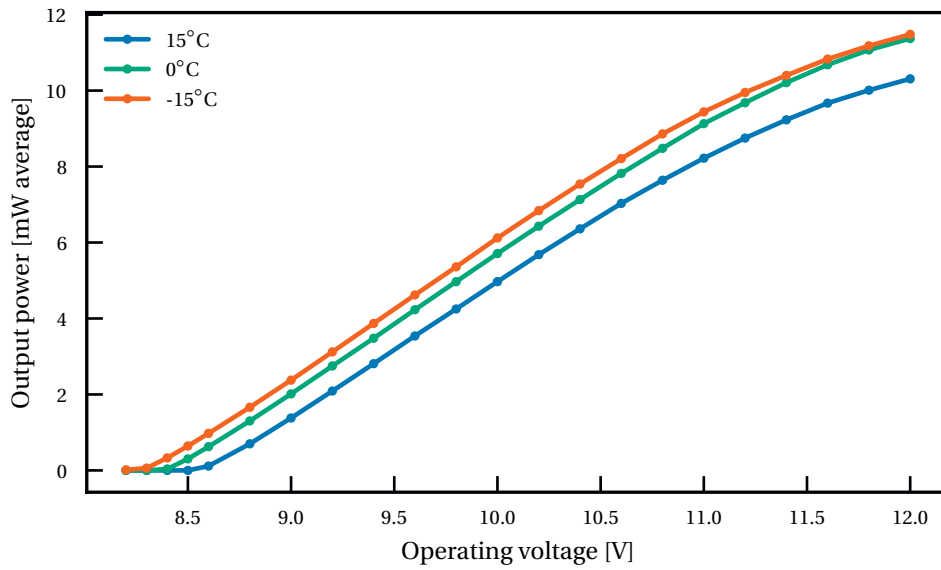
Figure 1.14 – Collimated laser output power at 2% duty cycle, 200 kHz repetition rate (100 ns pulse width) as a function of operating voltage for different operating temperatures.
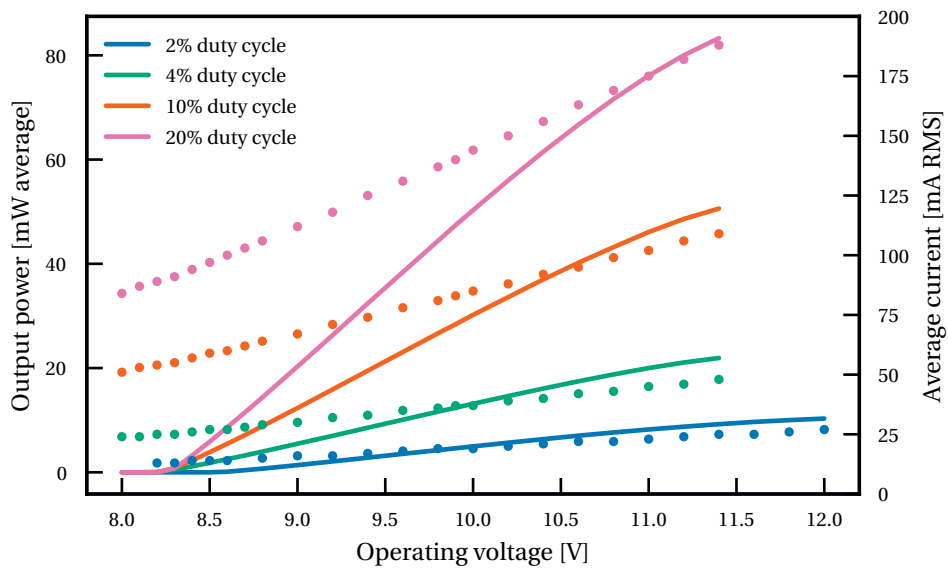
Figure 1.15 – Collimated laser output power with 100 ns pulse width measured at different duty cycles and for different operating voltages at −15 °C operating temperature (left scale). The dots represent the average current measured for each operating voltage (right scale).
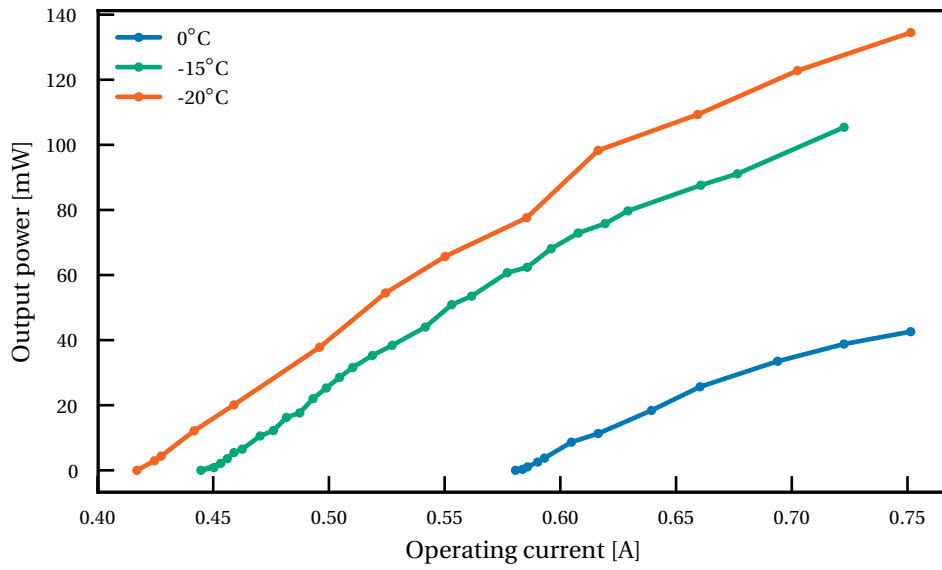
Figure 1.16 – Maximum power output measured for the collimated laser in CW operation at different operating temperatures for different operating currents.
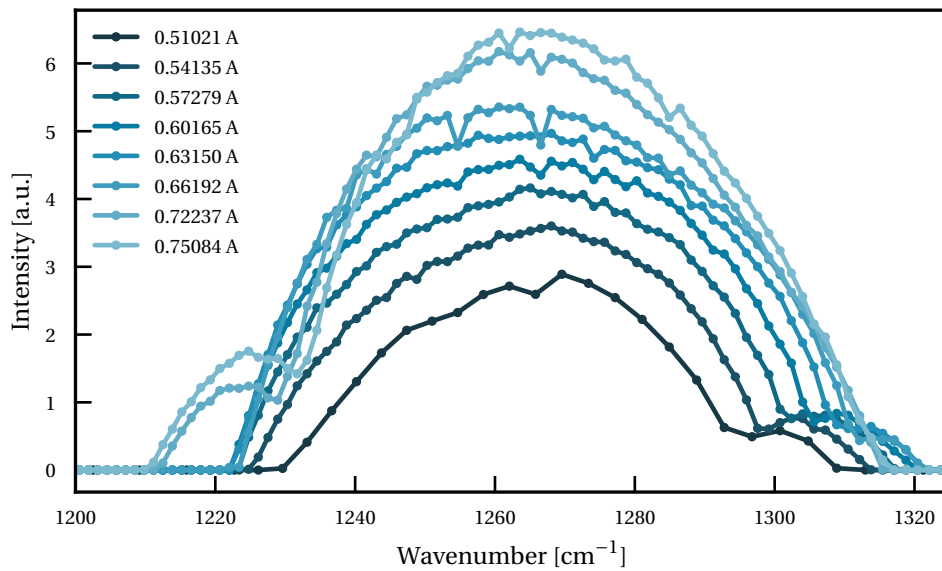
Figure 1.17 – Spectral range of the collimated laser for different operating currents at −20 °C operating temperature.
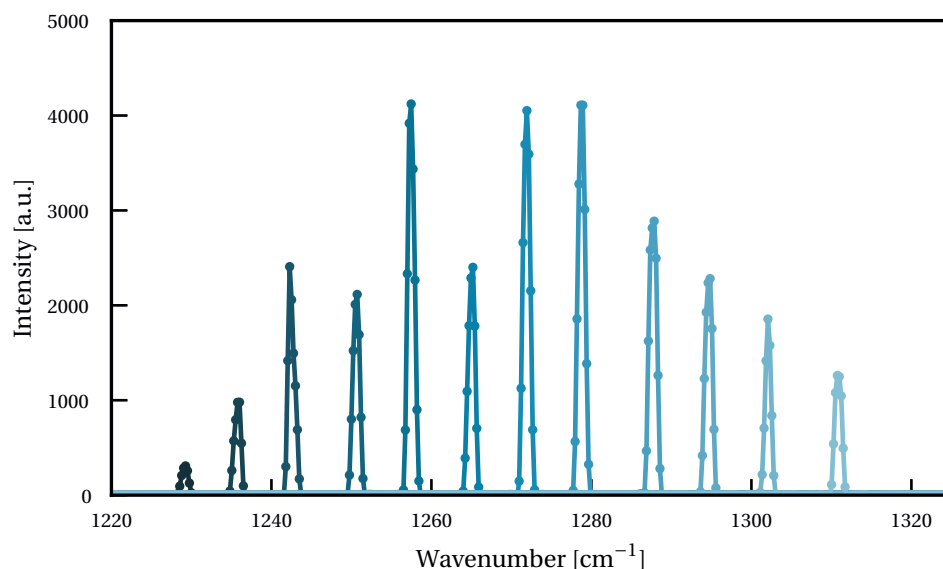
Figure 1.18 – Collection of FTIR spectra measured with a Bruker Vertex 70 spectrometer. For each spectrum, the angle of the EC feedback grating is modified. The laser is operating at $-13.5\,^{\circ}$C with a 0.6 A current.
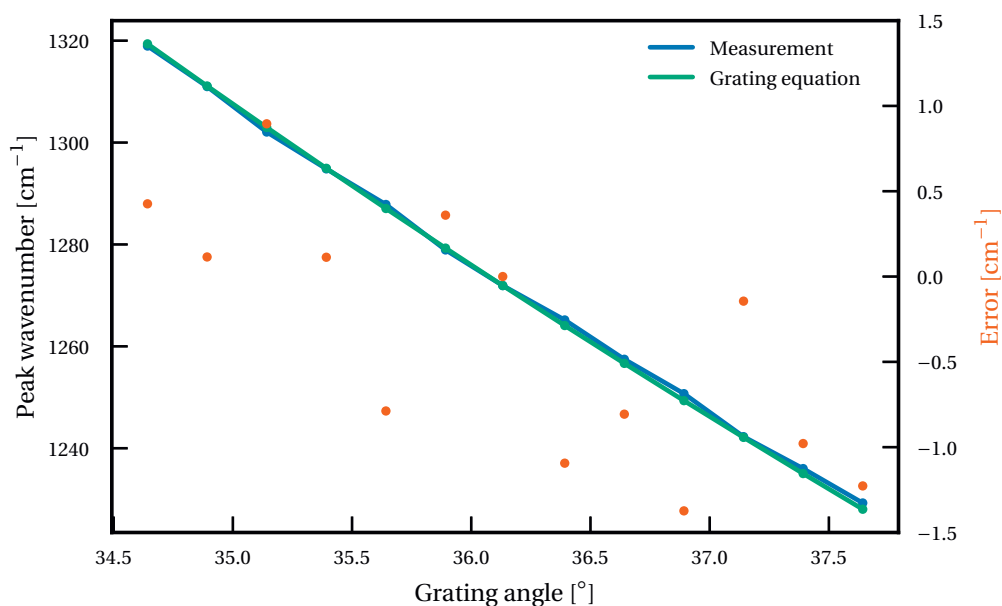
Figure 1.19 – Measured and theoretical output wavenumber of the tunable laser as a function of the grating angle. The orange dots represent the difference between the measurement and the theoretical value, caused by mode hopping of the laser setup.

1.4 Rigorous coupled-wave analysis

1.4.1 The planar grating problem

In this thesis, the properties of sub-wavelength binary gratings is studied and described in chapters 2 and 3. In order to study such gratings, it is necessary to be able to calculate their properties with a precise and efficient tool. Rigorous coupled-wave analysis (RCWA), also called Fourier modal method (FMM), is a semi-analytical method particularly useful for the analysis of the optical properties of planar gratings[38, 39]. For a detailed explanation of the method, we refer the reader to the work of Rumpf[45]. The method models the scattering of electromagnetic waves through a periodic dielectric layer or grating as described in figure 1.20. The layer is bound by two semi-infinite regions of constant refractive index. The grating layer of thickness d can be periodic in the x-y plane and is homogeneous in the z direction. The dielectric constant of the grating varies in the plane with a period Λ. In a binary grating for example, the period consists of two regions of different refractive indices. Since the grating layer is periodic, its dielectric constant is expandable in a Fourier series. An exact solution to the problem is given by solving Maxwell's equations in the three regions along the z direction and matching the boundary conditions at the interfaces. To do so, the electric and magnetic fields in the grating layer are also expanded in a Fourier series. Combining the expanded field equations with Maxwell's equations gives an equation system that can be put in matrix form.

Practically, the solution of the RCWA calculation provides a solution for the electromagnetic fields inside the periodic layer in the form given by equation (1.7):

$$\boldsymbol{\psi}(z) = \begin{bmatrix} \mathbf{e}_x(z) \\ \mathbf{e}_y(z) \\ \mathbf{h}_x(z) \\ \mathbf{h}_y(z) \end{bmatrix} = \begin{bmatrix} \mathbf{W} & \mathbf{W} \\ -\mathbf{V} & \mathbf{V} \end{bmatrix} \begin{bmatrix} e^{-\boldsymbol{\lambda} z} & \mathbf{0} \\ \mathbf{0} & e^{\boldsymbol{\lambda} z} \end{bmatrix} \begin{bmatrix} \mathbf{c}^+ \\ \mathbf{c}^- \end{bmatrix}, \tag{1.7}$$

where $\mathbf{e}_x(z), \mathbf{e}_y(z), \mathbf{h}_x(z), \mathbf{h}_y(z)$ are column vectors describing the amplitude of the expanded field harmonics or modes[45]. The terms $\mathbf{W}$ and $\mathbf{V}$ are matrices describing the eigenmodes of the electric and magnetic fields, respectively. The terms $e^{-\boldsymbol{\lambda} z}$ and $e^{\boldsymbol{\lambda} z}$ are diagonal matrices describing the propagation of the modes. The terms $\mathbf{c}^+$ and $\mathbf{c}^-$ are column vectors representing the amplitude coefficient of the forward and backward propagating modes, respectively. To be exact, the calculation should take into account an infinite number of harmonics and equation (1.7) would be composed of infinite matrices. Therefore, a finite number of harmonics or modes has to be selected before the computation, which can limit the accuracy of the method. The result converges to the proper solution with an increased number of modes[39]. The number of orders considered for the computation has to be chosen by studying the convergence of the solution.

The coefficients in the vectors $\mathbf{c}^+$ and $\mathbf{c}^-$ are particularly useful for the analysis of diffraction gratings. They represent the amplitudes of each forward and backward propagating modes. The relative efficiencies of the diffraction orders can be derived from these values[39, 45]. The
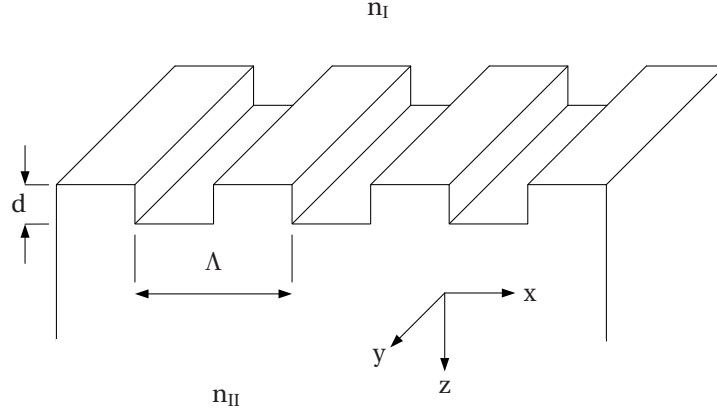
Figure 1.20 – Two-dimensional binary grating with period Λ and thickness d surrounded by two semi-infinite regions of refractive indices n_I and n_II

reflectivity and transmittance can also be used for the calculation of the effective refractive index of a sub-wavelength grating, as explained in more details in chapter 2.2.1.

1.4.2 Extension to multi-layer structures

The transfer-matrix method (TMM) or scattering matrices can be used to efficiently compute the propagation of electromagnetic waves through layers that are uniform in the propagation direction[46, 47, 40]. The grating layer is represented in matrix form by equation (1.7). This layer can be connected to the input and output regions by matching the boundary conditions at the interface. A representation of the concept is described in figure 1.21. In this case, the regions I and II are semi-infinite homogeneous dielectrics.

The boundary conditions at the interface of the grating layer are represented by equations (1.8) and (1.9) for the input and output regions, respectively:

$$
\begin{bmatrix} \mathbf{W}_\mathrm{I} & \mathbf{W}_\mathrm{I} \\ \mathbf{V}_\mathrm{I} & -\mathbf{V}_\mathrm{I} \end{bmatrix} \begin{bmatrix} \mathbf{c}_\mathrm{I}^+ \\ \mathbf{c}_\mathrm{I}^- \end{bmatrix} = \begin{bmatrix} \mathbf{W}_i & \mathbf{W}_i \\ \mathbf{V}_i & -\mathbf{V}_i \end{bmatrix} \begin{bmatrix} \mathbf{c}_i^+ \\ \mathbf{c}_i^- \end{bmatrix} \tag{1.8}
$$

$$
\begin{bmatrix} \mathbf{W}_i & \mathbf{W}_i \\ \mathbf{V}_i & -\mathbf{V}_i \end{bmatrix} \begin{bmatrix} e^{-\lambda_i L_i} & \mathbf{0} \\ \mathbf{0} & e^{\lambda_i L_i} \end{bmatrix} \begin{bmatrix} \mathbf{c}_i^+ \\ \mathbf{c}_i^- \end{bmatrix} = \begin{bmatrix} \mathbf{W}_\mathrm{II} & \mathbf{W}_\mathrm{II} \\ \mathbf{V}_\mathrm{II} & -\mathbf{V}_\mathrm{II} \end{bmatrix} \begin{bmatrix} \mathbf{c}_\mathrm{II}^+ \\ \mathbf{c}_\mathrm{II}^- \end{bmatrix}, \tag{1.9}
$$

where $\mathbf{c}_\mathrm{I}^+$, $\mathbf{c}_\mathrm{I}^-$, $\mathbf{c}_\mathrm{II}^+$, $\mathbf{c}_\mathrm{II}^-$ are the mode coefficients of the fields in the input (I) and output (II) regions in the forward (+) and backward (−) directions[45]. Combining equations (1.8) and (1.9), the electromagnetic fields at the output of the grating can be derived from the input fields. A detailed solution using TMM and scattering matrices can be found in Refs. [39] and [45], respectively.
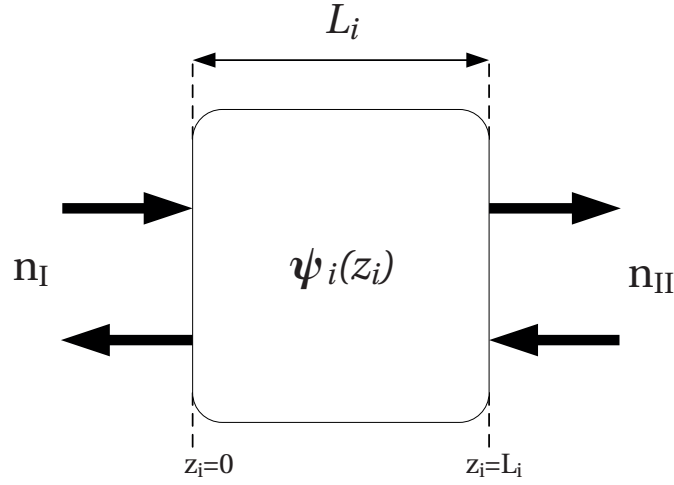
Figure 1.21 – Matrix representation of the grating layer of thickness L_i with forward and backward propagating inputs and outputs. The electromagnetic fields inside the grating layer are described by the equation system $\boldsymbol{\psi}(z)$. The semi-infinite input and output regions are homogeneous and of refractive indices n_I and $n_I I$, respectively.

Using the matrix approach, multiple grating layers can also be combined[48, 40, 45]. This is useful to model gratings that are not homogeneous in the z direction. To solve the problem, a staircase approximation can be used, which is described in figure 1.22. With this approximation, the grating region is decomposed in thin slices locally homogeneous in the z direction. A grating of thickness d and period Λ is sliced in an arbitrary number of layers of thickness L_i. The thickness of the individual layers can be different. Each layer is homogeneous in the propagation direction but composed of different refractive indices. For each layer, the boundary conditions can be solved using equations (1.8) and (1.9), replacing the surrounding medium by the previous and next layer. A larger number of layers gives a more precise solution at the cost of an increase in computational complexity[40].

1.4.3 Summary

The RCWA method is a semi-rigorous method for the simulation of planar gratings. It is extensively used in chapters 2 and 3, as it allows to accurately evaluate the properties of sub-wavelength gratings and diffractive optical elements. Combined with TMM, it can also be used to simulate multi-layer structures such as the ones described in chapter 4.
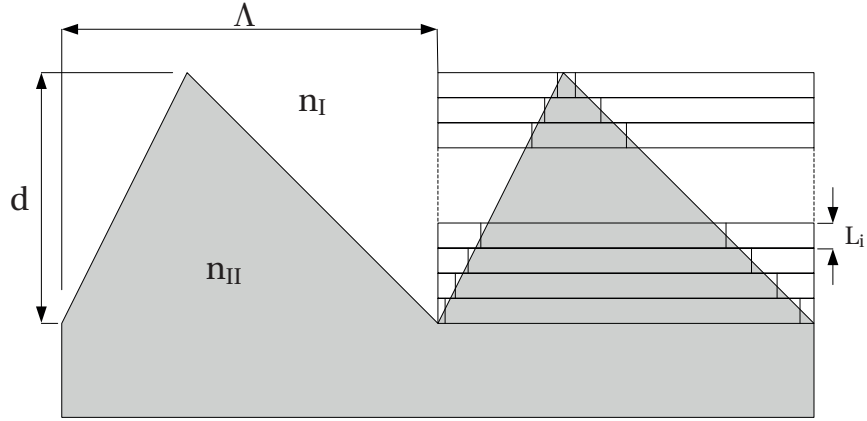
Figure 1.22 – Decomposition of a grating layer of thickness d and period Λ in multiple layers of thickness L_i, also called staircase approximation.

1.5   Conclusion

This chapter presented the key tools and methods used for the work presented in this thesis. The use of a QCL for the detection of trace amounts of cocaine in liquid phase has been presented. This demonstration exhibits the interesting properties of QCLs for the realization of compact sensing setups. An external cavity setup for broadband QCL emission has been introduced. This setup is used for the optical characterization of the fabricated passive optical components described in chapters 3 and 4. Additionally, the RCWA method for the semi-rigorous simulation of periodic gratings has been described. It is extensively used in chapters 2 and 3 for the analysis of the optical properties of periodic sub-wavelength structures.

The following chapter describes the use of sub-wavelength effective index structures to design diffractive optical elements. Elements such as beam-splitters, wave plates and polarizers can be realized using these structures.

2 Optical phase generation on a flat surface

2.1 Introduction

Refractive or reflective optical elements are often used to modify the path of electromagnetic radiation. One of the most common optical elements available is the lens, which can collect or distribute light. Other widely used components that can modify optical radiation include mirrors or prisms. Passive components can be refractive or reflective. For example, curved mirrors can be used to focus light instead of a refractive lens. Such components rely on geometrical optics laws to alter the light path. Except from the material dependant dispersion occurring in refractive elements, their function is not wavelength dependant.

Refractive optical elements locally modify the phase of an incoming wavefront. The phase of light propagating through an optical medium is given by

$$\phi = \frac{2\pi n d}{\lambda_0},$$ (2.1)

where n is the refractive index of the medium, d is the propagation length or thickness and λ_0 the wavelength in vacuum. The product nd is also called OPL. The phase of the the wavefront can be modified by changing the propagation length d, the refractive index n or both. For example, the thickness of a lens varies in the direction perpendicular to the optical axis, which leads to a phase variation when the light passes through the element.

Diffractive optical elements (DOEs) are thin optical elements that generate a 0 to 2π phase shift over their surface. In some cases, it can also be a multiple of 2π. In a DOE, the optical function is encoded by the position of the steps in the phase function. The phase shift over the surface of the DOE is usually defined by locally modifying its thickness. The thickness modifications can be continuous or made of discrete steps. The resulting optical function is wavelength dependent. For example, the focal length of a diffractive lens will vary depending on the illumination wavelength. A comparison between refractive and diffractive optical elements is shown in figure 2.1a. On the top is a refractive lens followed by three different DOEs. In the DOE, the phase function can be: (I) continuous, with 2π steps; (II) discrete, made of

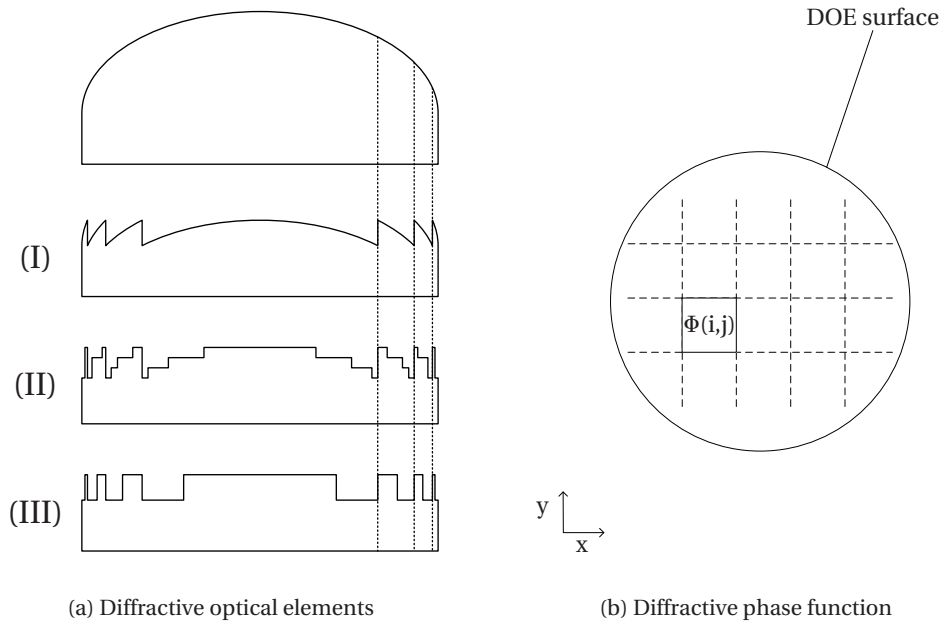(a) Diffractive optical elements   (b) Diffractive phase function

Figure 2.1 – (a) Comparison between a refractive lens (top) and three different refractive DOEs phase functions: (I) continuous profile, (II) multilevel profile and (III) binary profile. (b) Decomposition of the phase function in discrete phase steps over the surface of the DOE.

multiple steps; (III) binary[49]. The surface-relief of lenses or parabolic mirrors is macroscopic compared to the wavelength. On the contrary, DOEs can be much thinner, in the order of the wavelength, because the phase function is decomposed in smaller 2π phase steps. Binary or multi-step profiles yield lower efficiencies compared to continuous but are easier to fabricate. Lithographic techniques can be used to make DOEs in a cost efficient way. The ability to locally control the phase shift of light is of great interest and can be applied to realize different optical functions such as polarizers, beam shaping elements or diffractive lenses. Figure 2.1b represents the discretized phase function over the surface of a DOE. Each area of the surface of the element provides a specific phase change that eventually produces the desired diffraction pattern when illuminated. The design of such DOEs relies on the generation of discrete phase steps over the surface, which are usually made by thickness variations. Knowing the refractive index of the material, one is therefore able to assign the desired phase shift to each part of the surface. According to equation (2.1), if the thickness of the optical element remains constant - i.e. the surface is flat - the phase can still be modified by a variation of the refractive index. The local change of index can be achieved by a modification of the material itself such as in gradient-index (GRIN) optical components[50]. Another possibility is to use sub-wavelength structures, which modify the refractive index perceived by the light. There are different kind of sub-wavelength structures with different operating principles and properties. Such structures are nowadays called metasurfaces. They have also been called artificial index structures or zero-order gratings. When the structures are smaller than the wavelength, the refractive index

perceived by the light can be tailored to take an artificial value. In a metasurface, the thickness remains constant and the phase varies locally through the sub-wavelength modifications of either the 2D geometry or pattern or the polarization state[8]. Metasurfaces can be sorted in different categories such as geometric-phase holograms, Huygens' metasurfaces or effective index structures.

Geometric-phase holograms   In geometric-phase elements, the phase shift does not come from a variation of OPL but by variation of the polarization state of the light[51, 52, 53, 54]. Using circularly polarized light and an artificially birefringent material, it is possible to locally change the orientation of the optical axis of the surface[55, 56]. The local 'geometric' orientation of the optical axis generates a phase shift in the circularly polarized waves[57]. Geometric-phase holograms working in the MIR and near-infrared (NIR) using metallic sub-wavelength structures have been previously demonstrated[58, 59]. In the visible, geometric-phase holograms have been demonstrated using liquid crystals[60]. Geometric-phase holograms have the ability to cover a complete phase shift from 0 to 2π with great transmission efficiencies, theoretically up to 100 % for polarized light[52, 59].

Huygens' metasurfaces   It was demonstrated in 2012 that nanometric silicon cylinders exhibit magnetic dipole resonances at visible wavelengths[61, 62]. By changing the size of the sub-wavelength cylinders, also called 'Mie resonators', or the materials used, the resonance can be adjusted to a desired wavelength. Periodic arrangements of these structures can be used as anti-reflective coatings[63]. In this particular case, the magnetic and electric resonances of the structures overlap and change the scattering profiles of the sub-wavelength structures. The scattering becomes unidirectional and no reflection occurs. The period of the structures and diameter can be modified to locally change the phase shift of the metasurface, which are also called 'Huygens' surfaces[64]. The demonstration of phase holograms in the NIR based on this effect have been reported[65, 66]. Huygens' surfaces are promising elements that can offer efficient transmission and a continuous phase shift from 0 to 2π[67]. In the MIR, their use as collimation lens for a QCL has been recently demonstrated[68].

Effective index structures   Effective index structures or zero-order gratings use sub-wavelength gratings to modify the refractive index of the surface. They are described in more detail in the following sections of this chapter.

The recent developments in metasurfaces renew the interest in DOEs. The main advantage is the reduction of lithographic steps required for the fabrication. If the thickness is constant, a single etch step is sufficient to shape the element. The use of sub-wavelength features is also particularly interesting in the MIR, given the larger dimensions. However in general, if the desired optical function is feasible, refractive elements are better than DOEs. The main advantage of DOEs consists of a precise control of the diffraction angle. This property is

extremely useful for the realization of precise illumination patterns[49]. These elements are used for example in deep ultraviolet (UV) lithography for beam homogenization or in NIR 3D sensors for the projection of a specific pattern.

Mid-infrared optical elements are made of exotic materials that are often expensive. Diffractive elements allow to greatly reduce the thickness of an optical element compared to its refractive equivalent. This eventually helps to miniaturize systems. With wafer-scale sources and detectors available, the passive optical components can indeed be the limiting factor of the compactness of a system. There are few existing micro-optical MIR components. Germanium micro-lenses have been proposed for the collimation of QCLs[69]. A similar function using Huygens' metasurfaces has been demonstrated[68]. Metasurface-based MIR components can potentially help to realize compact sensors or systems.

Geometric-phase holograms require circularly polarized light because the phase function is coded in the polarization state, which adds extra complexity in the setup. Huygens' meta-surfaces require heterogeneous materials and are therefore more complex to fabricate. They require a high index material in a low index matrix or substrate, which restricts the possibilities in MIR[67]. This chapter focuses on the generation of phase differences using sub-wavelength dielectric gratings. These zero-order gratings allow to shape the phase by directly structuring the bulk material, which greatly simplifies the fabrication process. For example, widely available silicon wafers can be directly patterned to produce MIR DOEs.

2.2 1-D effective index structures

2.2.1 Theoretical background

Light incident on a diffraction grating produces forward and backward diffracted waves at distinct angles. In transmission, these angles are given by the grating equation

$$m\lambda = \Lambda\left(n_1 \sin\theta_i + n_2 \sin\theta_m\right), \tag{2.2}$$

where λ is the vacuum wavelength of the light, θ_i is the incidence angle of the light in the surrounding medium of index n_1, θ_m is the angle of m order diffracted wave in the grating medium of index n_2 and Λ is the period of the grating. Sub-wavelength gratings, also called zero-order gratings, consist of periodic structures that exhibit no diffraction orders other than the zero order [70]. Using equation (2.2), the angle at which the mth order is diffracted can be expressed as

$$\theta_m = \arcsin\left(\frac{m\lambda}{\Lambda n_2} - \frac{n_1}{n_2}\sin\theta_i\right). \tag{2.3}$$

Assuming that the light is at normal incidence ($\theta_i = 0$), there are no real solutions to this equation for orders other than $m = 0$ if $\lambda/(\Lambda n_2) > 1$ or $\Lambda < \lambda/n_2$. As a result, diffraction gratings with a sufficiently small period compared to the wavelength will only transmit and reflect
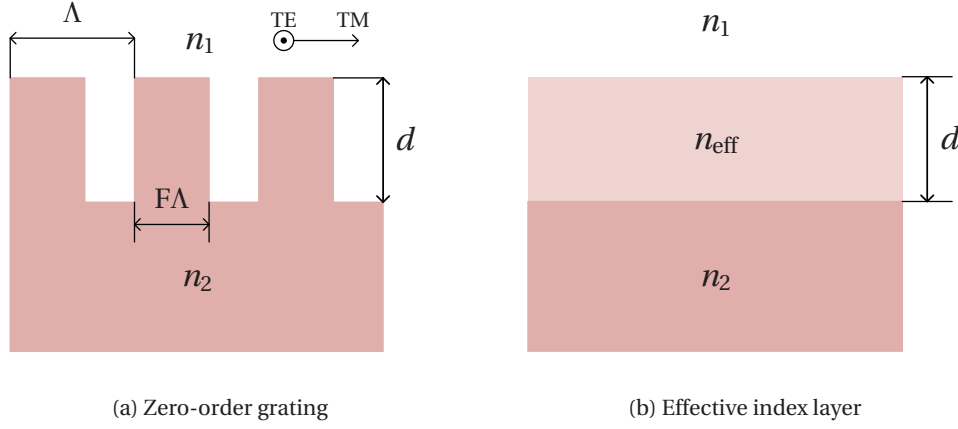
(a) Zero-order grating

(b) Effective index layer

Figure 2.2 – (a) Zero-order grating with period $\Lambda < \lambda/n_2$, fill factor F and thickness d. The refractive index of the surrounding medium and grating material are n_1 and n_2, respectively. (b) Equivalent representation of the zero-order grating with thickness d and refractive index n_{eff}.

incident light in the zero order, without diffraction. A binary grating with such properties is described in figure 2.2(a). Since there are no diffracted orders present, it is convenient to represent the grating as a homogeneous layer with an index of refraction n_{eff}, as described in figure 2.2(b). This effective refractive index is an artificial value that allows to model the behaviour of the light propagating through such grating. The optical properties of a thin layer of effective index n_{eff} and thickness d are those of a thin interference layer. The reflection coefficient at wavelength λ of a thin layer at normal incidence is given by the equation

$$r = \frac{r_a + e^{i2\delta} r_b}{1 + e^{i2\delta} r_a r_b}, \tag{2.4}$$

where $r_a = \frac{n_1 - n_{\text{eff}}}{n_1 + n_{\text{eff}}}$, $r_b = \frac{n_{\text{eff}} - n_2}{n_{\text{eff}} + n_2}$ and

$$\delta = \frac{2\pi d}{\lambda} n_{\text{eff}}. \tag{2.5}$$

The reflectance is given by $R = |r|^2$. Equation (2.5) gives the phase change of the light going through the the thin layer. It is therefore possible to tune the phase of the light going through the zero-order grating by modifying its effective index without changing its thickness. The actual value of the effective index depends on the refractive indices of the surrounding medium and grating material, the fill factor, the period and the thickness of the grating. It is also dependent on the polarization of the light.

The ability to convert the structural parameters of a zero-order grating directly to an effective index value is crucial for the design of a DOE. A number of methods are available to estimate the effective index according to these parameters[70]. They provide an approximate value of

the equivalent refractive index given various grating parameters.

Effective index method The most straightforward approach is to treat the effective index as directly proportional to the ratio of surrounding medium n_1 and grating material n_2 such as

$$n_{\text{eff}} = n_1 + F(n_2 - n_1), \tag{2.6}$$

where F is the fill factor. This rough approximation is more accurate for transverse-electric (TE) polarization. For TM polarization, it is preferable to use other approximations for more accurate results.

TM approximation method Another approximation for TM polarization is given by Gaylord[70]. It considers the electric displacement in the the grooves and tranches of the grating to be the same for periods much smaller than the wavelength. The average effective index in the grating region is expressed as

$$n_{\text{eff}} = \left[(1 - F)/n_1^2 + F/n_2^2 \right]^{-1/2}, \tag{2.7}$$

where F is the fill factor, n_1 and n_2 are the refractive indices of the surrounding medium and grating material, respectively.

Fourier expansion method Another method based on the Fourier series expansion of the electric field in the periodic grating is given by Lalanne[71]. The equation for TM polarisation is

$$n_{\text{eff}} = \left[\frac{1}{a_0} + \frac{\pi^2}{3} \left[F(1 - F) \frac{(\epsilon_2 - \epsilon_1)}{\epsilon_2 \epsilon_1} \right]^2 \frac{\epsilon_0}{a_0^3} \alpha^{-2} + O(\alpha^{-4}) \right]^{1/2}, \tag{2.8}$$

where F is the fill factor, n_1 and n_2 are the refractive indices of the surrounding medium and grating material, respectively, $a_0 = F/\epsilon_2 + (1 - F)/\epsilon_1$, $\epsilon_0 = \epsilon_2 F + \epsilon_1 (1 - F)$, $\alpha = \lambda/\Lambda$ $\epsilon_1 = n_1^2$ and $\epsilon_2 = n_2^2$.

All of these approximations expect the grating period to be much smaller than the wavelength. In addition, the thickness of the layer is not taken into account. An article by Lalanne describes the behaviour of the effective index for small thicknesses, i.e. $d < \lambda/2$[72]. It concludes that for thicknesses smaller than 0.2 wavelengths, it is recommended to use rigorous computation instead of approximations to determine the effective refractive index. A rigorous method will therefore provide more accurate results, at the cost of requiring more computing power. The effective index can indeed be numerically calculated by a rigorous method such as RCWA, described in more details in chapter 1.4. Since the RCWA simulation provides the reflectance of the grating, it is possible to determine the effective index by finding the grating thickness providing the lowest reflectance. Considering thin film interference, the lowest reflectance

thickness corresponds to an optical thickness of $\lambda/4$ or odd multiples of it. The effective index is therefore obtained through the equation

$$n_{\text{eff}} = \frac{(2m+1)\lambda}{4d_{\text{rcwa}}}, m \in \mathbb{N},$$ (2.9)

where d_{rcwa} is the minimum reflectance thickness obtained by RCWA simulation. The value given by the RCWA method is the most accurate, provided that enough orders are taken into account in the computation.

Figure 2.3 compares the value of the effective refractive index from the approximation equations (2.6), (2.7) and (2.8) with the numerical value obtained by RCWA simulation. The grating material possesses a refractive index of 3.419, corresponding to the index of silicon at $7.8\,\mu$m[73]. The calculations are made for TM polarization. Except for the effective index method, better suited for TE polarization, the other models and the rigorous numerical value match well for large thicknesses and small periods with respect to the wavelength. However, the models diverge from the numerical value for large periods or small thicknesses. For the actual fabrication of zero-order structures, it is more convenient to use a period as close as possible to λ/n_2 and keep the thickness as small as possible. The fabricated grating period cannot be infinitely small and high aspect ratios structures are difficult to realize. While requiring more computational power, the rigorous numerical method is therefore preferred to the approximation methods for the determination of the effective index of zero-order gratings. The following sections describe the dependency of the effective refractive index on the main parameters, calculated by RCWA simulation.
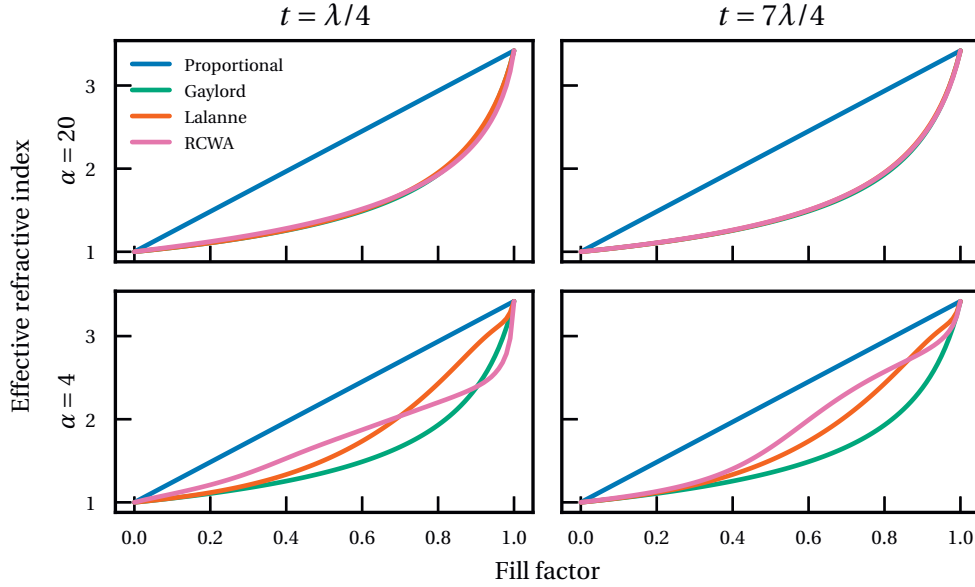
Figure 2.3 – Comparison of the effective index values for TM polarization obtained by equations (2.6) (Effective index method), (2.7) (TM approximation method), (2.8) (Fourier expansion method) and RCWA simulation. The grating material is silicon and its refractive index taken at 7.8 μm wavelength. Two values of the optical thickness t of the grating are compared, as well as two period ratios $\alpha = \lambda/\Lambda$.

2.2.2 Polarization

For one-dimensional structures, it is not possible to make polarization independent zero-order gratings because of their non-symmetrical features. A comparison between the effective index in TE and TM polarization is shown in figure 2.4. In TE, TM polarization, the electric field is parallel, perpendicular to the grooves and ridges of the grating, respectively, as described in figure 2.2a. It can be observed that for TE polarization, the effective index increases rapidly at low fill factor values, whereas in TM polarization the steep part of the slope is shifted towards larger fill factors. For actual structures, it is preferable to work in areas where the slope is smaller in order to reduce the impact of fabrication errors. Since we generally want to obtain small refractive indices compared to the substrate index, it more convenient to work in TM polarization.

2.2.3 Fill factor

The approximation models rely mostly on the fill factor for the determination of the effective index of a zero-order grating. It is indeed the parameter that impacts the most the value of the effective index. Figure 2.5 shows the evolution of the effective index as a function of the
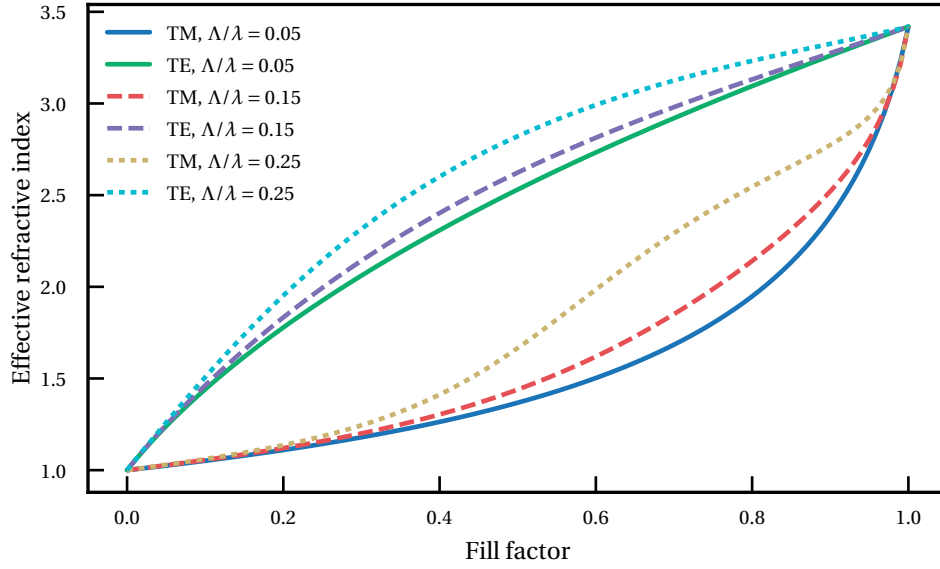
Figure 2.4 – Comparison of the effective index of a zero-order grating as a function of fill factor for TE and TM polarization. The grating refractive index is 3.419 at 7.8 μm wavelength.

fill factor for a grating material of index 3.419 and a wavelength of 7.8 μm for TM polarization. An increase in fill factor always increases the effective index. However, the effective index also depends on the optical thickness and the period to wavelength ratio. While shorter periods tend to the same effective index value, the large period behaviour of the effective index constrains the use of rigorous calculations rather than a model.

2.2.4 Period

As mentioned earlier, the period to wavelength ratio has an influence on the effective index. Figure 2.6 describes the relationship between the period to wavelength ratio and the effective index. All other parameters constant, a larger period increases the effective index. The single layer homogeneous representation of the zero-order grating is also less accurate for larger periods close to the sub-wavelength limit.

2.2.5 Thickness and surrounding medium

Figure 2.7 compares the effective index of the zero-order grating for different period to wavelength ratios, as a function of the optical thickness. The effective index is higher for small thicknesses and tends to stabilize for larger values.

In all these simulations, the thickness of the equivalent homogeneous layer is assumed to be the same as the thickness of the zero-order grating. The effective index is determined by finding the lowest reflectance thickness. Figure 2.8 compares the effective index of the
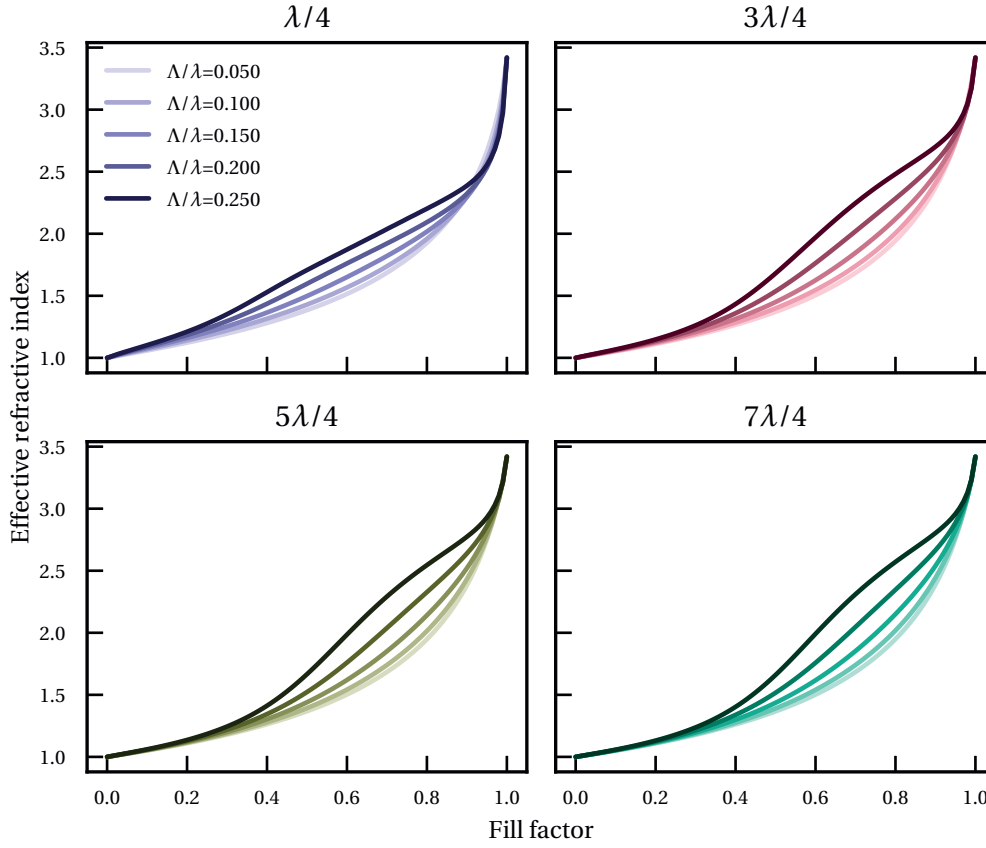
Figure 2.5 – Effective index of a zero-order grating as a function of fill factor calculated by RCWA simulation. The grating material possesses a refractive index of 3.419 at 7.8 µm wavelength. The results are compared for different optical thicknesses ranging from $\lambda/4$ to $7\lambda/4$ as well as different period to wavelength ratios Λ/λ.

layer obtained for a zero order grating of refractive index 3.419 with the index of a theoretical grating of same thickness and ridges material but surrounded by air. For this second grating, the effective index is also determined by equation (2.9) but this time the thickness obtained by RCWA corresponds to the maximum transmittance value. Although the gratings possess the same features, the change of refractive index behind the grating modifies the effective index value obtained. For a given thickness, the effective index can also be extrapolated by calculating the refractive index of a thin layer that would yield the same reflectance. This approach gives slightly different results, especially for small layers, because the effective thickness of the equivalent layer is not exactly equal to the actual grating thickness. The effective index is an artificial representation that does not exactly correspond to reality and should therefore be used with caution.
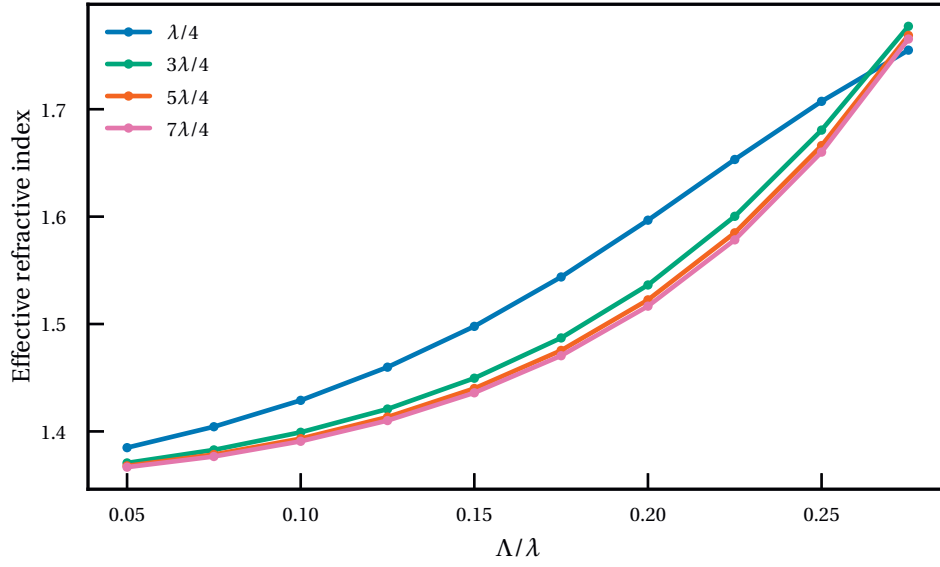
Figure 2.6 – Comparison of the effective index values for TM polarization obtained by RCWA simulation. The grating material has a refractive index of 3.419 and the fill factor is set to 0.5. The period to wavelength ratio dependance of the effective refractive index is displayed for different optical thicknesses of the layer ranging from $\lambda/4$ to $7\lambda/4$
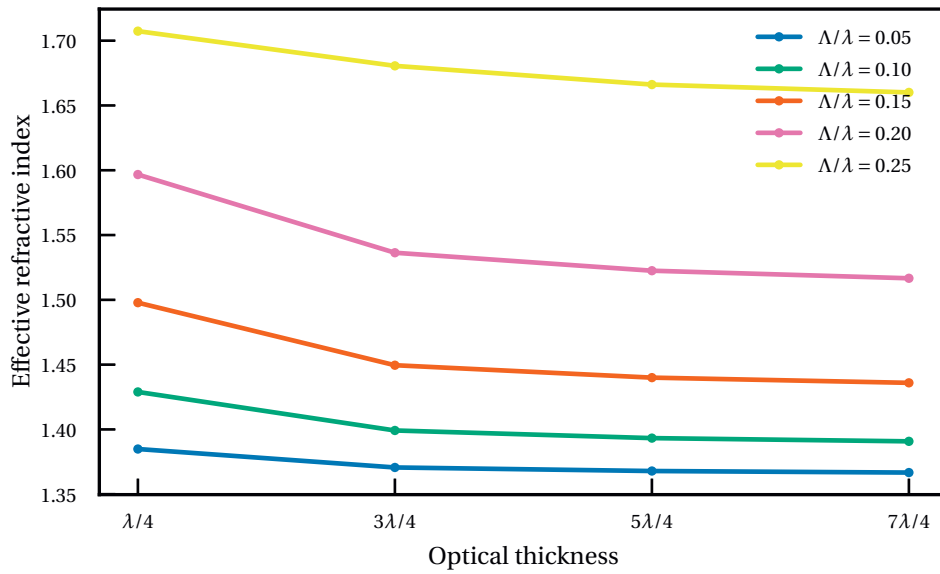
Figure 2.7 – Effective index of a zero-order grating as a function of optical thickness by RCWA simulation. The grating material possesses a refractive index of 3.419 at 7.8 µm wavelength and the fill factor is set to 0.5. The results are compared for different period to wavelength ratios Λ/λ.

Figure 2.8 – Comparison of the effective index obtained by RCWA simulation for a grating with refractive index of 3.419 and a grating with the same index floating in air. The first grating is noted R and the second is noted T.

2.3 Anti-reflective binary structures

2.3.1 Elements based on zero-order gratings
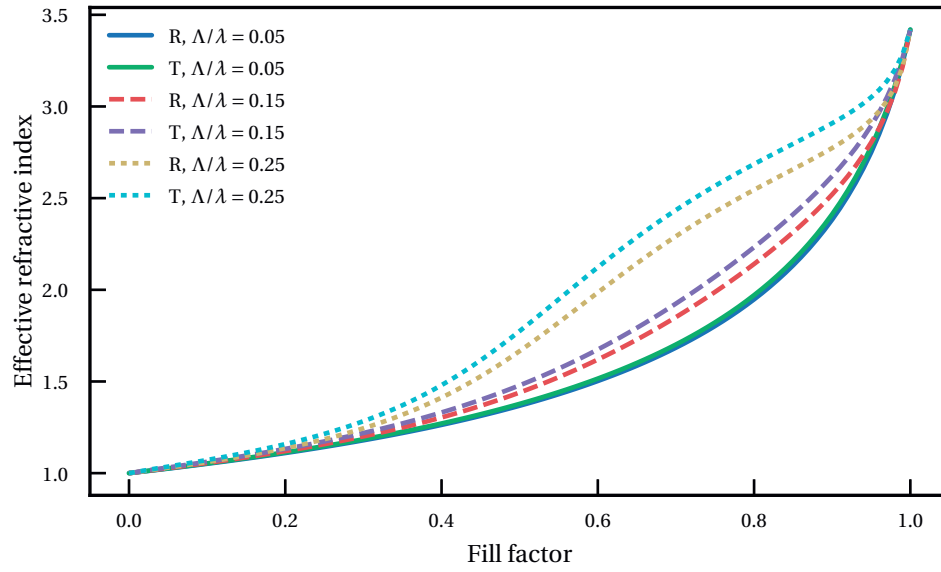
The fabrication of optical elements based on zero-order gratings has been demonstrated[72]. A variety of functions such as birefringent materials[74, 75, 76] or diffractive elements[77, 78, 79] can be realized. The realization of diffractive elements is of particular interest because the zero-order grating allows a single step fabrication. Discrete phase steps can be realized by locally changing the periodicity or the fill factor of the grating while keeping the same thickness for the whole element.

For traditional diffractive elements, the phase steps are realized by the presence or not of the grating material. The phase difference at every layer of thickness d is given by

$$\frac{2\pi d}{\lambda}\Delta n, \tag{2.10}$$

where Δn is the difference between the refractive indices of the substrate and the surrounding medium. The total phase difference should be 2π. Using an effective index medium, multiple phase steps can be achieved by local changes of the refractive index, allowing to combine them in a single layer. Highly efficient diffractive elements such as blazed gratings can be realized with this method[80].

2.3.2 Anti-reflective layer

From the Fresnel equations, the reflectance of an interface between media of index n_1 and n_2 at normal incidence is given by the equation

$$R = \left|\frac{n_1 - n_2}{n_1 + n_2}\right|^2. \tag{2.11}$$

A substrate of refractive index 1.5 in air has a reflectance of 4%. Silicon and germanium are transparent materials in the MIR which possess a refractive index around 3.5 and 4, respectively. They are commonly used for the fabrication of MIR lenses and windows. Using their refractive index values into equation (2.11) gives a reflectance of approximately 30.36 %, respectively. With a reflectance so high, it is mandatory to use an anti-reflective layer on the surface of the optical element.

A perfect anti-reflective layer between two media of index n_1 and n_2 possesses a refractive index of $\sqrt{n_1 n_2}$ and an optical thickness of $\lambda/4$ or a thickness of

$$d = \frac{\lambda}{4\sqrt{n_1 n_2}}. \tag{2.12}$$

Inserting these values into equation (2.4) yields zero reflectivity. Since it is difficult to find a material for an anti-reflective layer that has the exact refractive index required, an effective
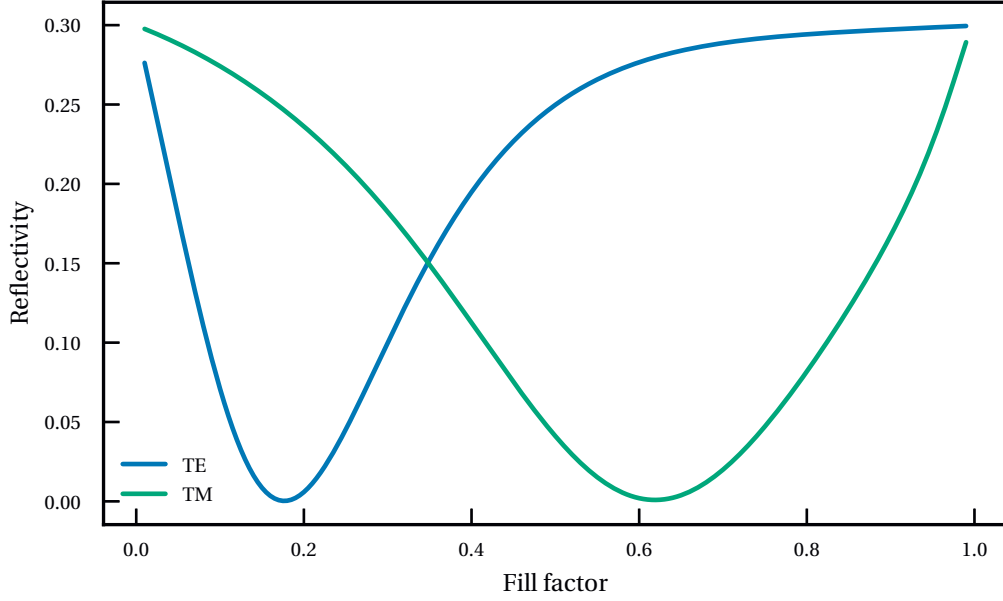
Figure 2.9 – Simulated reflectivity of a silicon binary grating as a function of its fill factor for TE and TM polarizations. The thickness of the grating is $\lambda_0/(4\sqrt{n_{\text{Si}}})$.

index layer is a potential good candidate for this function. The use of zero-order gratings as anti-reflective layers has been previously demonstrated[70, 81, 82]. Even if the zero-order grating properties do not exactly match equation (2.12), the reflectance will still be attenuated because the index difference at each interface will be smaller. Figure 2.9 shows the reflectivity of a grating as a function of the fill factor for TE and TM polarization simulated by RCWA. The thickness is set using equation (2.12). The lowest reflectivity corresponds to an effective index of $\sqrt{(n_1 n_2)}$. In this case, n_1 is equal to 1 (air) and n_2 is the refractive index of silicon at $7.8\,\mu$m. It can be observed that the zero reflectivity fill factor value is strongly dependant on the polarization.

2.3.3 Combining anti-reflective and diffractive functions

The realization of diffractive elements in silicon or germanium for the MIR suffers from the high reflectance of these materials. It is however possible to combine diffractive and anti-reflective properties of a zero-order grating under certain conditions. We propose here a novel approach to design anti-reflective structures within a diffractive design.

According to equation (2.4), the reflectivity coefficient of a thin layer is minimized when the optical thickness of the layer is equal to $(2m+1)\frac{\lambda}{4}, m \in \mathbb{N}$. In this case, the phase given by equation (2.5) becomes $(2m+1)\frac{\pi}{2}$ and destructive interference occurs at the first interface,
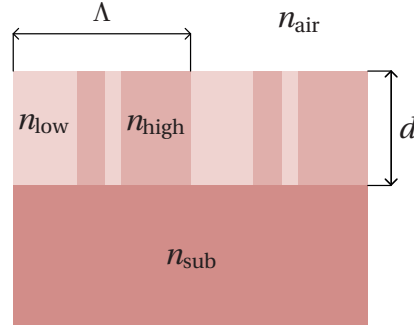
Figure 2.10 – Single layer binary diffractive optical element with period Λ and thickness d.

minimizing the reflectivity coefficient. This constrains the values of n_{eff} to

$$n_{\text{eff}} = \frac{(2m+1)\lambda}{4d}, m \in \mathbb{N}. \tag{2.13}$$

A single layer binary diffractive element consists of the periodic arrangement of two materials of index n_{low} and n_{high} in a single layer, as described in figure 2.10. The phase difference between the two regions is given by equation (2.10) and is equal to π. Usually, the low index material is air and the high index material is the substrate. Using a zero-order grating, it is possible to generate two different effective refractive indices other than n_{air} and n_{sub} by locally changing the fill factor the sub-wavelength structures.

Combining a phase change of π and the low reflectivity coefficient condition on n_{eff}, the two refractive indices are given by

$$n_{\text{low}} = \frac{(2m+1)\lambda}{4d} \tag{2.14}$$

$$n_{\text{high}} = \frac{(2m+3)\lambda}{4d}. \tag{2.15}$$

Using these values in the reflectivity coefficient equation (2.4), we obtain

$$r_{\text{low}} = \frac{16\left(\frac{d}{\lambda}\right)^2 n_1 n_2 - (1+2m)^2}{16\left(\frac{d}{\lambda}\right)^2 n_1 n_2 + (1+2m)^2} \tag{2.16}$$

$$r_{\text{high}} = \frac{16\left(\frac{d}{\lambda}\right)^2 n_1 n_2 - (3+2m)^2}{16\left(\frac{d}{\lambda}\right)^2 n_1 n_2 + (3+2m)^2}. \tag{2.17}$$

Since the reflectivity coefficient of the whole pattern should be the same, the thickness of the grating is constrained. When equations (2.16) and (2.17) are equal, the thickness is constrained by

$$\frac{d}{\lambda} = \frac{\sqrt{4m^2 + 8m + 3}}{4\sqrt{n_1 n_2}}. \tag{2.18}$$

It is therefore possible to use a zero-order grating with two different effective indices to generate a binary diffractive element. The parameter m defines the thickness of the grating, the value of the two effective indices as well as the reflectivity coefficient of the grating. A higher value of m results in a lower reflectivity coefficient and a larger grating thickness.

The fill factors corresponding to the two desired effective indices can be easily found by calculating the reflectance of a grating at the thickness given by equation (2.12) by RCWA simulation. The reflectance shows two minima, each corresponding to the quarter wave optical thicknesses. A practical example will be presented in the following chapter.

2.4 2-D effective index structures

Two-dimensional sub-wavelength structures allow the realization of polarization dependent or independent structures. Birefringent materials based on sub-wavelength gratings have been previously demonstrated[76, 70, 83, 84]. While the one-dimensional grating is inherently polarization dependent, two-dimensional symmetrical structures can be used to design polarization independent zero-order gratings. Two-dimensional structures also allow more flexibility in the the choice of the periodicity of the sub-wavelength arrangement. The period can be different for each axis, as well as the shape of the sub-wavelength structures.

2.4.1 Lattice and shape

Symmetrical two-dimensional sub-wavelength gratings can be used as a polarization independent anti-reflective coating. We compare here square and hexagonal lattices of two-dimensional gratings in silicon. Square, hexagonal and circular structure shapes are also compared in combination with the two lattices. Figure 2.11 shows the different structures analyzed. The diameters d of the circular shapes and the parameters a of the hexagonal and square shapes can take any value between 0 and the lattice parameter. The fill factor or volume ratio is defined as the surface of the structure divided by the area of the lattice unit cell. The configurations (a) and (c) described in figure 2.11 do not allow to reach a volume ratio of 1. Their respective maximum volume ratios are $\pi/4$ and $\pi/(2\sqrt{3})$.

Figure 2.12 shows the reflectivity of an interface of air and a patterned silicon surface. An infinite array of pillars is simulated. The shape and lattice combinations of the pillars are described in figure 2.11. The structures are simulated by finite difference frequency domain (FDFD) using the commercial software CST Microwave Studio (CST MWS). The reflectivity is

calculated at normal incidence at 7.8 μm wavelength. A single cell of the lattice is represented and is infinitely periodic. The period or lattice constant is set to 1.95 μm. The grating thickness corresponds to an optical thickness of $\lambda/4$ with a refractive index equal to $\sqrt{n_{Si}}$, given by equation (2.12). The effective indices are directly related to the grating reflectivity by equation (2.4). For the square lattices, the parameters p_x and p_y are equal. For the square structure, the parameters a_x and a_y are equal. The structures are therefore symmetrical and polarization-independent. It can be observed that all the shape-lattice combinations are able to provide zero reflectivity. The square lattice shows zero reflectivity at a volume ratio of 0.49, while the hexagonal lattice shows zero reflectivity at 0.52. These values do not depend on the shape of the structures but only on the chosen lattice. It can however be observed that the curves (a) and (c) diverge from (b) and (d), respectively, for volume ratios close to the maximal value for the cylinders.

We also compare inverted structures made of holes instead of pillars. Figure 2.13 shows the reflectivity of a sub-wavelength structure composed of holes with a shape and lattice described in figure 2.11. The parameters are the same as for the pillars described in the previous paragraph. It can be observed that the pattern of holes also reaches zero reflectivity. In this case, the volume ratio at which the reflectivity is minimal is similar for all lattice and shape combinations and equal to 0.29. As for the pillars, the curves (a) and (c) diverge from (b) and (d), respectively, for volume ratios close to the maximal size of the cylindrical holes.
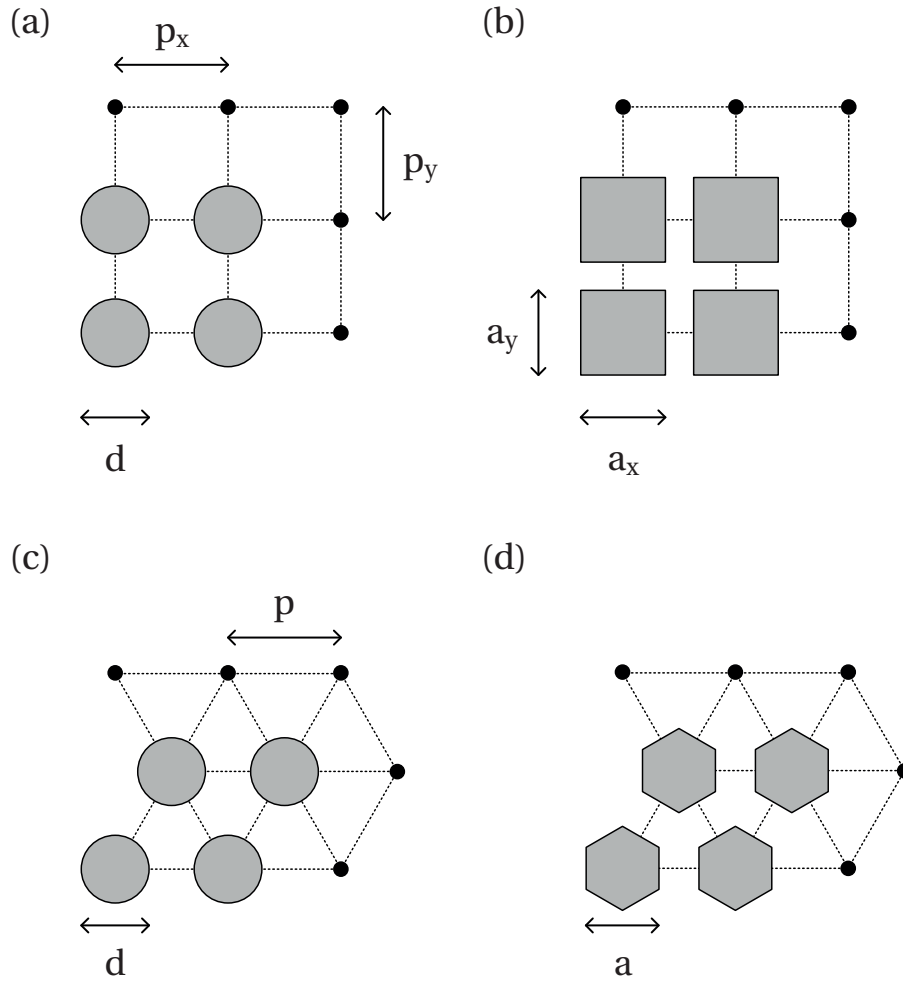
Figure 2.11 – Two-dimensional lattices and structures combinations: (a)square or rectangular lattice with lattice parameters p_x and p_y and circular structures of diameter d; (b)square or rectangular lattice with lattice parameters p_x and p_y and square or rectangular structures of length a_x and a_y; (c)hexagonal lattice with lattice parameter p and circular structures of diameter d; (d)hexagonal lattice with lattice parameter p and hexagonal structures with diameter of inscribed circle a.
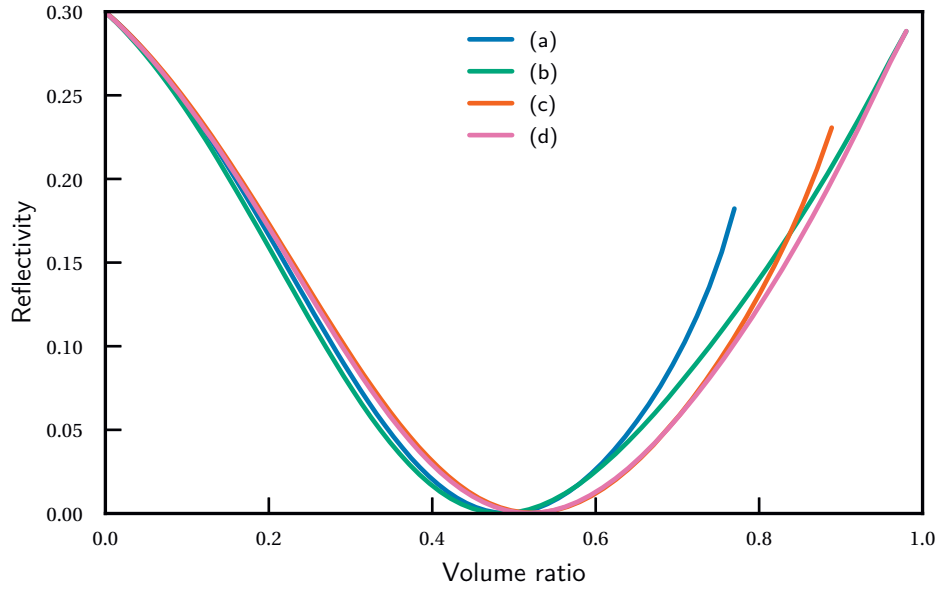
Figure 2.12 – Simulated reflectivity of an infinitely periodic array of sub-wavelength structures in silicon. The shape of the structures and periodic lattice used are described in figure 2.11. The thickness of the structures is $\lambda_0/(4\sqrt{n_{\mathrm{Si}}})$.
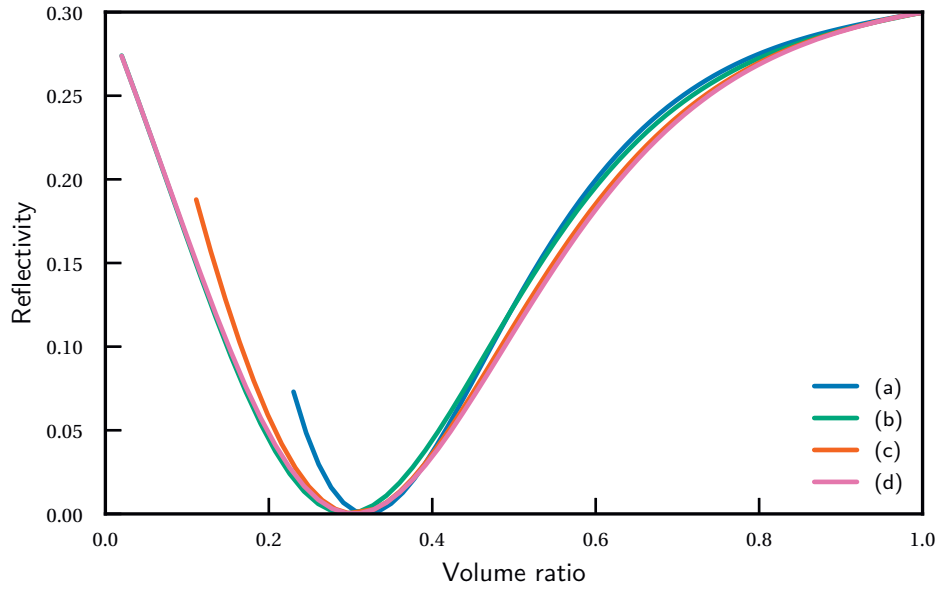

Figure 2.13 – Simulated reflectivity of an infinitely periodic array of sub-wavelength holes in silicon. The shape of the holes and periodic lattice used are described in figure 2.11. The depth of the holes is $\lambda_0/(4\sqrt{n_{\mathrm{Si}}})$.

2.4.2 Polarization dependence

Non-symmetrical two-dimensional sub-wavelength gratings can be used as a polarizers and form a birefringent effective index layer. Figure 2.14 shows the simulated reflectivity of an infinite array of rectangular silicon pillars. The simulations are made by RCWA. The shape of the pillars is described in figure 2.11 (b). The sides a_x and a_y of the rectangular pillars are varying. The light is linearly polarized in the x direction at 7.8 μm. The periods p_x and p_y are both equal to 1.95 μm. The height of the pillars is chosen using equation (2.18) with a value of $m = 1$, which corresponds to 4.08 μm. The two circled low-reflectivity areas visible in this figure correspond to optical path lengths of $3\lambda/4$ and $5\lambda/4$ for the x polarized light.

Figure 2.15 shows the simulated reflectivity of the structures described in the previous paragraph with linearly polarized light at 45°. The circles areas correspond to the intersection of the low reflectivity areas of figure 2.14 for x and y polarized light. In these areas, the phase difference between the two components of the polarized light is noted ϕ. When $\phi = \pi$, the periodic structure acts as a low reflectivity half-wave plate.

2.5 Conclusion

Zero-order gratings or sub-wavelength structures in one or two dimensions can be used to generate arbitrary optical phase profiles on a surface. These structures can be patterned in silicon, germanium or other transparent materials in the MIR. It is a cost efficient way to fabricate MIR optical elements, because the structure is binary and can therefore be patterned with a single fabrication step. The large wavelength is also an advantage for the precise fabrication of sub-wavelength structures. The following chapter will describe a practical application of zero-order gratings in the MIR. It covers the design, fabrication and characterization of a MIR binary DOE in silicon. The binary structure combines anti-reflective properties and a specific diffractive function.
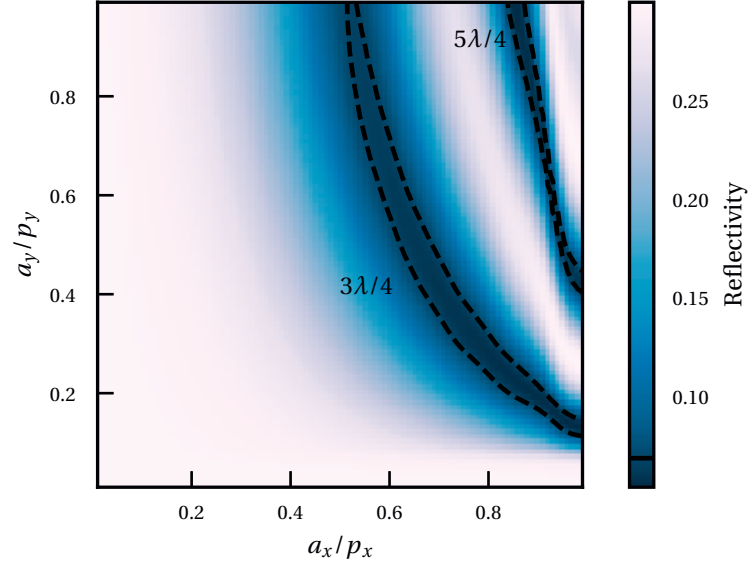
Figure 2.14 – Simulated reflectivity of an infinitely periodic array of rectangular silicon pillars under linearly polarized light along the x axis at 7.8 μm wavelength. The sides of the rectangles are equal to a_x and a_y. The thickness of the structures is 4.08 μm. In this case the lattice constants p_x and p_y are both equal to 1.95 μm. The optical length of the periodic structures is approximately equal to $3\lambda/4$ and $5\lambda/4$ in the circled areas.
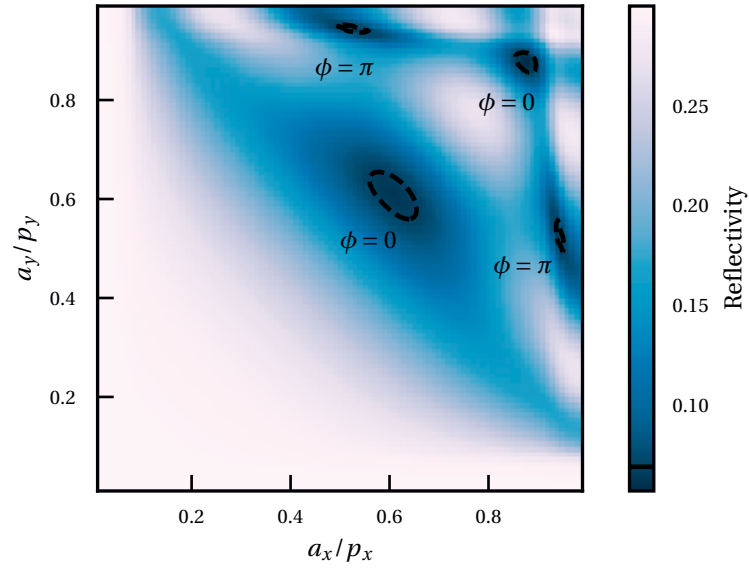
Figure 2.15 – Simulated reflectivity of an infinitely periodic array of rectangular silicon pillars under linearly polarized light at 45° at 7.8 μm wavelength. The sides of the rectangles are equal to a_x and a_y. The thickness of the structures is 4.08 μm. In this case the lattice constants p_x and p_y are both equal to 1.95 μm. The ϕ value corresponds to the phase difference in the circled areas between the x and y components of the polarized light.

3 Binary diffractive and anti-reflective structures

3.1 Introduction

In this chapter the design, fabrication and characterization of an anti-reflective binary phase grating in silicon are described. Historically, binary diffractive optical elements can refer to optical elements with a discrete structure composed of N layers or levels, by opposition to continuous profile diffractive elements where the number N approaches infinity[85]. The phase steps of the discrete structures are usually $2\pi/(N+1)$, which allows to cover the 0 to 2π range and approximate a continuous profile. In this chapter, the term 'binary structure' refers to a single layer discrete diffractive structure ($N = 1$) that can therefore be fabricated in a single lithographic step. The scalar binary diffractive design therefore generates a phase shift of 0 and π.

In this chapter, we describe the design, fabrication and characterization of a binary grating in silicon that combines anti-reflective and diffractive functions. The contents of this chapter have been reported at the 2016 EOS Topical Meeting on Diffractive Optics in Berlin[86] and have been published in the journal Optics Letters[87].

3.2 Design of binary phase gratings

Binary phase gratings can be used to generate an array of waves of homogeneous intensity from a single incoming wave. Such gratings producing homogeneous patterns are also called Dammann gratings[88]. They can be used for example as multiple beam-splitters.

When a grating is illuminated by a plane wave, the Fourier transform of the grating transmission function gives the amplitude of the diffraction orders. The binary grating is designed using the method described by Dammann[88]. In that case, the transmission function of the grating is $t(x, y)$ and can be spatially separated in x and y, such that $t(x, y) = t_1(x) t_2(y)$. It corresponds to the phase part of the transmission so that $t(x, y) = \exp{-i\phi(x, y)}$, where $\phi(x, y)$ is the local phase shift. For a one-dimensional grating, we only consider one axis and

Table 3.1 – List of inflection points for different Dammann gratings generating $2N+1$ homogeneous diffraction orders. The efficiency η_{th} is the ratio of light transmitted in the $2N+1$ orders over the total transmitted light. The efficiency η_{refl} takes into account the reflectivity losses of the surface and therefore $\eta_{\text{th}} > \eta_{\text{refl}}$. The parameter δ represents the smallest feature size of the design normalized by the grating period. This list is a partial reproduction from the table that has been published by Krackhardt and Streibl[90].

N	x_1	x_2	x_3	x_4	η_{th}	η_{refl}	δ
1	0.367629				66.42%	46.52%	0.13
2	0.019304	0.367657			77.39%	54.44%	0.019
3	0.104582	0.155223	0.377125		65.52%	46.24%	0.051
4	0.099750	0.159152	0.369009	0.491743	66.32%	47.19%	0.0083

$t(x, y) = t_1(x)$. For a binary phase pattern, the transmission function can take two values, $+1$ and -1, which correspond to a phase shift of 0 or π, respectively. The transmission function is symmetrical and ranges from $-1/2$ to $1/2$, with the period p normalized to 1[89]. It contains N symmetrical inflection points $x_1, x_2, ..., x_N$ where its value switches from -1 to $+1$ or inversely, as described in figure 3.1. The diffraction orders are given by the Fourier transform which takes the form

$$T_0 = 2 \sum_{n=0}^{N} (-1)^n (x_{n+1} - x_n), \tag{3.1}$$

$$T_m = \frac{1}{m\pi} \sum_{n=0}^{N} (-1)^n \left[\sin 2\pi m x_{n+1} - \sin 2\pi m x_n \right], \tag{3.2}$$

with $x_0 = 0$ and $x_{N+1} = 1/2$[90]. Since the intensity of the diffraction orders must be equal, $|T_0|^2 = |T_1|^2 = |T_N|^2$. This gives a set of N equations that can be solved numerically to find the positions of the inflection points x_n. Table 3.1 shows a non-exhaustive list of solutions for the transmission function that has been published by Krackhardt and Streibl[90]. Using these values, a binary diffractive element generating $2N+1$ diffraction orders of equal intensity can be designed.

Figure 3.1 shows the transmission functions described in table 3.1 and the resulting distribution of their diffraction orders. The design efficiency is the ratio of light transmitted in the $2N+1$ homogeneous orders over the total incident light. This efficiency value neglects the reflectivity of the surface and assumes that all the light goes through. This is not the case in reality, especially if the grating is made of a high index material such as silicon. Table 3.1 also compares the design efficiency η_{th} with η_{refl}, the efficiency including the reflectivity of a grating made of silicon.
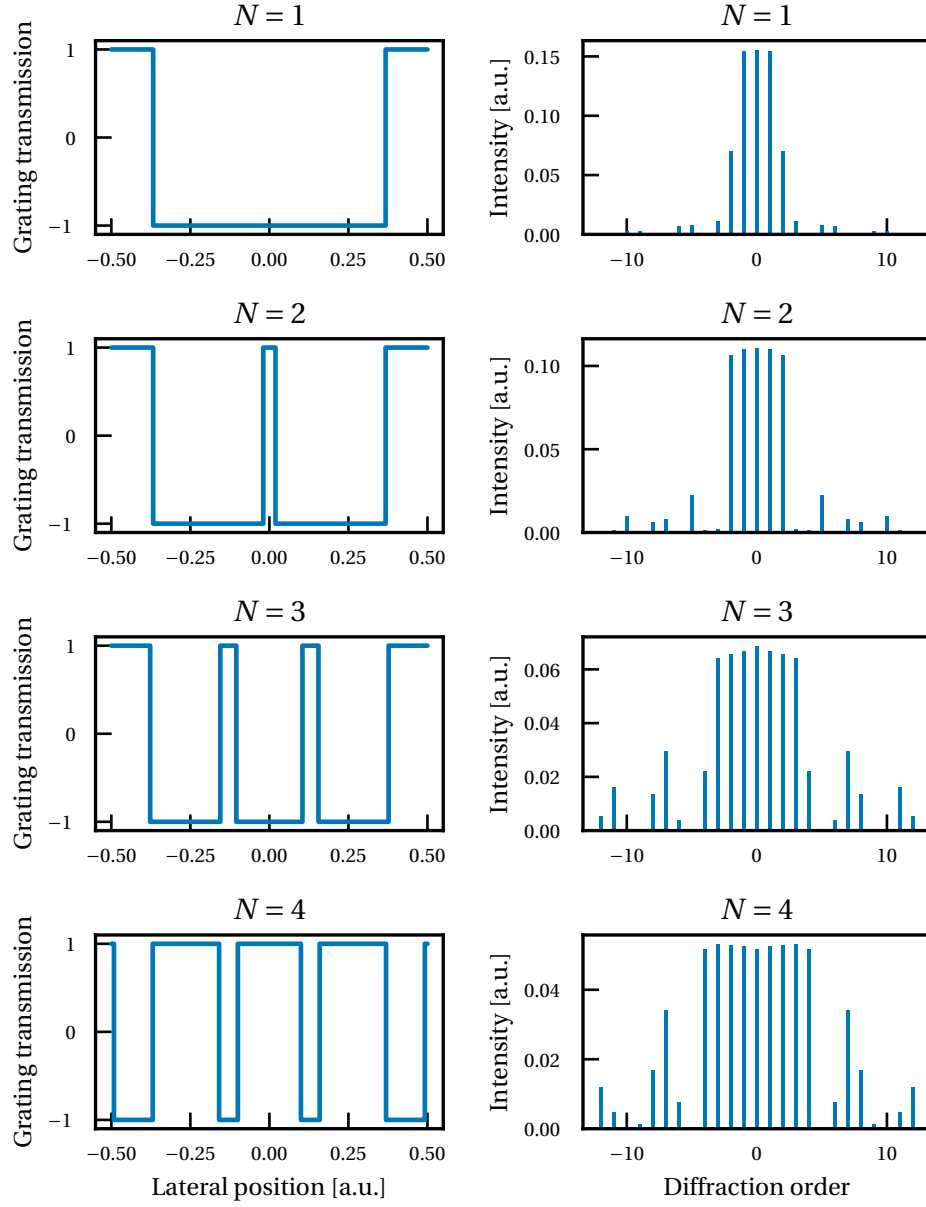
Figure 3.1 – Transmission functions with N symmetrical inflection points (left) and correspon-ding diffraction patterns of the Dammann gratings producing $2N+1$ homogeneous diffraction orders (right). The positions of the transmission function phase jumps are normalized over one grating period.

3.3 Anti-reflective Dammann grating design

3.3.1 Principle

The anti-reflective and diffractive design combines a traditional binary scalar grating design with an embedded sub-wavelength grating. Figure 3.2 describes this design process. The binary scalar design is characterized by its depth, period and positions of the inflection points. The embedded sub-wavelength grating is characterized by its sub-period and the fill factors of its low and high index areas. The actual depth of the final grating depends on the effective indices of the sub-wavelength grating. This approach allows to shift at will the optical phase difference generated by the different areas of the grating. While the binary scalar design is limited to the generation of 0 and π phase shifts, the sub-wavelength grating allows to move the phase shifts to $\pi/2$ and $3\pi/2$ for example. A critical part of the design is the smallest feature size of the scalar design. The feature should be large enough to contain multiple sub-periods of the sub-wavelength grating. While the sub-period can be arbitrarily chosen, it is preferable to keep it as large as possible for the fabrication of the structure.

Using equation 2.18, it is possible to generate a binary pattern having a beam splitter as well as anti-reflective function. The design parameters of the grating are its period, the positions of the phase jumps, the period of the sub-wavelength structure, the fill factors of the phase-coding areas and the thickness. The positions of the phase jumps are determined by the binary scalar design itself, taken from table 3.1. The period of the grating affects the angle between the diffraction orders following the grating equation 2.2. Once the grating period Λ is set, the fill factors corresponding to the desired effective indices are found by calculating the minima of reflectivity by RCWA simulation[38]. The thickness is calculated according to the design parameter m, using equation 2.18. Figure 3.3 shows the reflectivity of an infinite binary silicon grating as a function of its fill factor. The grating thickness is set to 4.084 μm, corresponding to the parameter $m = 1$. The wavelength is 7.8 μm and the grating period is 1.95 μm. At this thickness, the two reflectivity minima should theoretically be of equal amplitude. The actual thickness at which the two minima are equal is computed and found to be 3.942 μm. The thickness and fill factor values are then used in the Dammann grating design.

The complete grating structure is then simulated by RCWA. Since the grating is designed to produce homogeneous beams, its performance is evaluated by calculating the homogeneity or contrast of the diffraction orders. The contrast is defined as

$$\frac{I_{max} - I_{min}}{I_{max} + I_{min}}, \tag{3.3}$$

where I_{max} and I_{min} are the maximum and minimum values of the diffraction orders intensity, respectively. At this point, a global optimization is performed to find the fill factors that minimize the contrast in the vicinity of their initial values. The thickness is kept constant to simplify the computation.

The design process can be summarized as follows. The grating period and sub-periods are
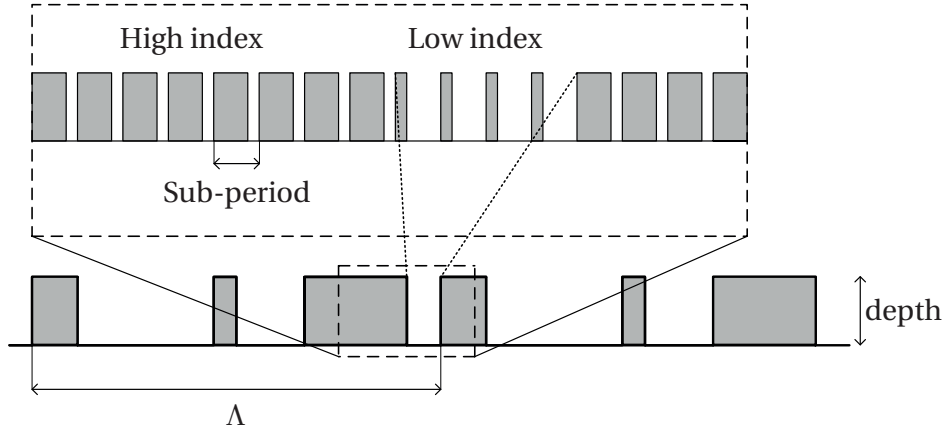
Figure 3.2 – Design principle of the anti-reflective and diffractive grating. The bottom curve represents the profile of an arbitrary binary diffractive scalar design with its period $Llambda$ and depth. The grating depth is chosen so that the phase difference between the plain and empty areas of the design is equal to π. The top curve represents the replacement of the plain and empty areas with a sub-wavelength grating with its own sub-period and two different fill factors. The thickness of the sub-wavelength grating is not necessarily equal to the depth of the binary scalar design.

first set. The fill factors and thickness are obtained from by RCWA simulation and optimized for minimum reflectivity. These values are then used to design the Dammann grating. The complete grating is then simulated by RCWA and optimized for minimum contrast.

3.3.2 Thickness

As previously described in chapter 2.3.3, the thickness of the anti-reflective grating can only take discrete values defined by equation 2.18. Table 3.2 lists the resulting grating depth according to the design parameter m. The values are calculated for a silicon grating at a 7.8 μm wavelength. For $m = 0$, the effective indices of the sub-wavelength structures are close to those of air and silicon, which explains the poor improvement in reflectivity. The depth of the structure increases with m, as well as the optical length. For $m = 1$, the optical length of the structure with low and high refractive index are $3\lambda/4$ and $5\lambda/4$, respectively. For $m = 2$, the low and high indices are $5\lambda/4$ and $7\lambda/4$, respectively.

The first step of the design defines two fill factors that correspond to an infinite grating. The thickness is corrected from the initial guess given by equation 2.18, so that the reflectivity obtained with both fill factors is equal. The three beam Dammann grating design is simulated for different thicknesses according to the parameter m. The contrast of the grating as a function of depth is compared in figure 3.4. The design method provides good results for various m values. The contrast decreases with increasing depth. This decrease of performance
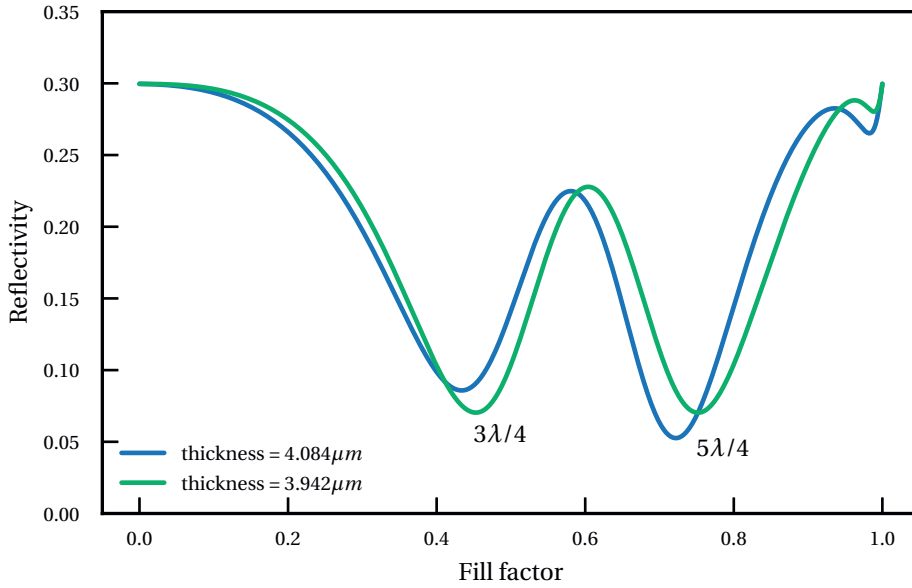
Figure 3.3 – Reflectivity of an infinite silicon binary grating as a function of its fill factor calculated by RCWA. The wavelength is 7.8 μm and the polarization is TM. The grating period is 1.95 μm. Two different thickness values are simulated, 4.084 μm and 3.942 μm. On each curve, the first and second reflectivity minima correspond to an optical path of $3\lambda/4$ and $5\lambda/4$, respectively. At these particular values, the destructive interference of the reflected waves is maximized, which results in a minimum of reflectivity.

can be explained by the increase of optical path length. An error on the fill factor and consequently on the effective index has a greater impact on the phase when the optical length is larger. The reflectivity of the grating as a function of depth is compared in figure 3.5. As expected, the reflectivity is reduced with increased structure thickness.

3.3.3 Number of sub-periods

The effective index calculations assume an infinite number of sub-wavelength periods. However, the fabricated structure contains a finite number of sub-periods in each design area. To determine the minimum number of sub-periods required in an area to act as an effective medium, a nine beam Dammann grating is simulated with different grating periods. The periods are chosen such that the minimum feature size corresponds to 1, 2, 4 and 8 sub-periods of the effective index sub-structure. The sub-period size is $\lambda/4$. Figure 3.6 compares the design performance according to the number of sub-periods in the smallest grating region. The performances after optimization are also compared. The grating simulation matches very well with the theoretical values of reflectivity and contrast for eight sub-periods. Under that value, the design can still be optimized by tuning the fill factors.

Table 3.2 – Depth, reflectivity and effective refractive indices of anti-reflective diffraction gratings in silicon at 7.8 μm according to equation 2.18. At this wavelength, the refractive index of silicon is 3.419.

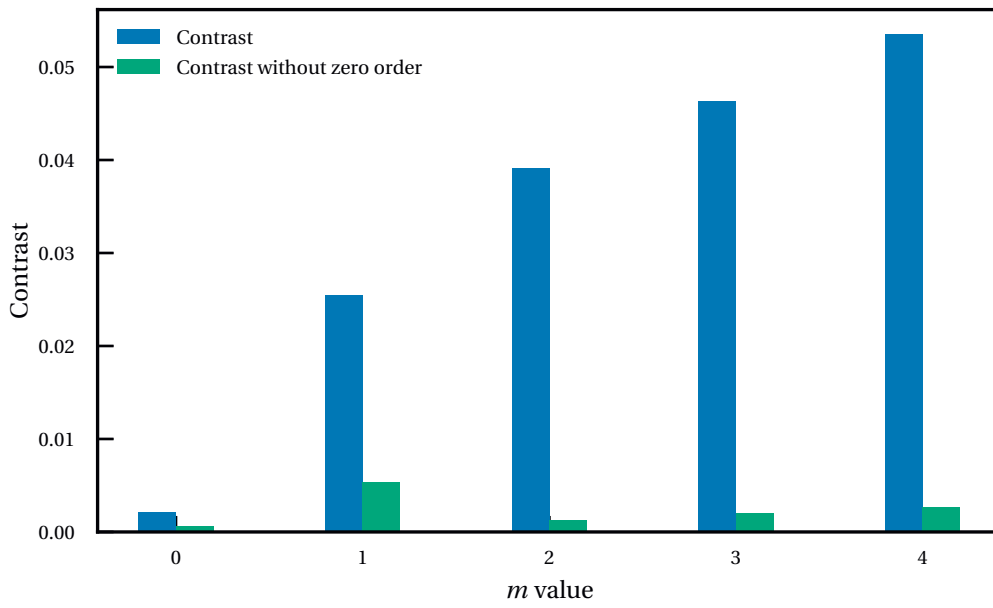| m	depth [μm]	$\lvert r \rvert^2$	n_{low}	n_{high}
0	1.827	0.2500	1.068	3.203
1	4.084	0.0625	1.432	2.387
2	6.239	0.0278	1.563	2.188
3	8.371	0.0156	1.631	2.097
4	10.493	0.0100	1.673	2.044

Figure 3.4 – Contrast of a binary anti-reflective Dammann grating producing three homogeneous diffraction orders. The contrast is given by equation 3.3.

3.3.4 Inverted binary pattern

The Dammann grating design sets the amplitude of the diffraction orders but not their phase, which can be inverted[89]. The binary grating phase coding areas can therefore be inverted without changing the diffraction pattern. This means that the fill factors can be switched. The surfaces of the two phase coding areas are not equal for these designs, which can be observed in figure 3.1. Figure 3.7 compares the contrast of different Dammann grating designs and different grating periods. The normal and inverted designs assign the low and high index fill factor to the largest area of the grating, respectively. The gratings are simulated with a sub-period of 1.95 μm at 7.8 μm wavelength. Two grating periods are compared for each design, in which the smallest design feature contains 4 or 8 sub-periods. The inverted design generally provides a poor contrast performance compared to the normal design. This effect is also more
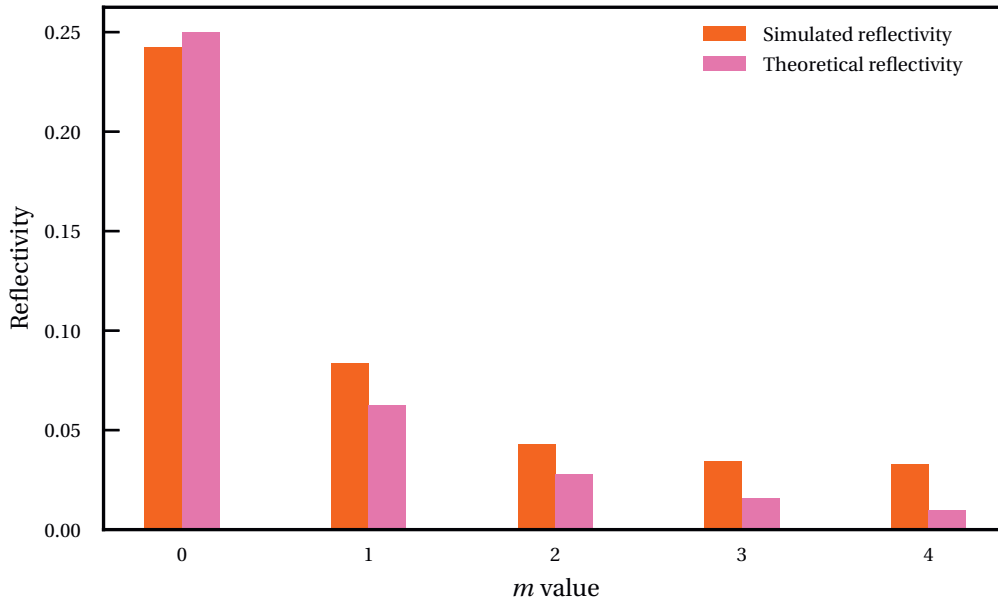
Figure 3.5 – Simulated reflectivity of a binary anti-reflective Dammann grating producing three homogeneous diffraction orders, compared with the theoretical value.

important when the Dammann grating period is smaller. It is therefore preferable to assign the low index fill factor to the largest phase coding area of the grating. The smallest feature size with respect to the period can be found in table 3.1. The periods of the simulated gratings with 8 sub-periods are 59 μm, 404 μm, 308 μm and 944 μm for the 3, 5, 7 and 9 beam designs, respectively. The periods are halved for the 4 sub-period designs. Since the Dammann grating design is based on scalar theory, the angle between the diffraction orders should be small to keep it valid[85, 91]. The grating design therefore performs better for large periods, which generate smaller diffraction angles.
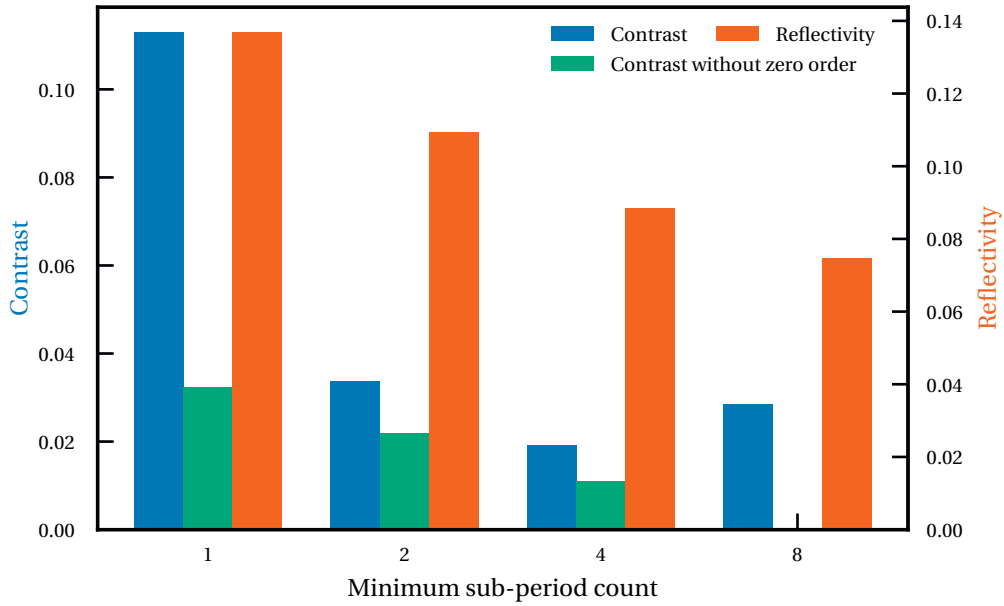
Figure 3.6 – Performance of a binary anti-reflective Dammann grating producing nine homogeneous diffraction orders. The contrast is given by equation 3.3. The grating period is increased such that the smallest design feature contains 1, 2, 4 or 8 sub-periods.
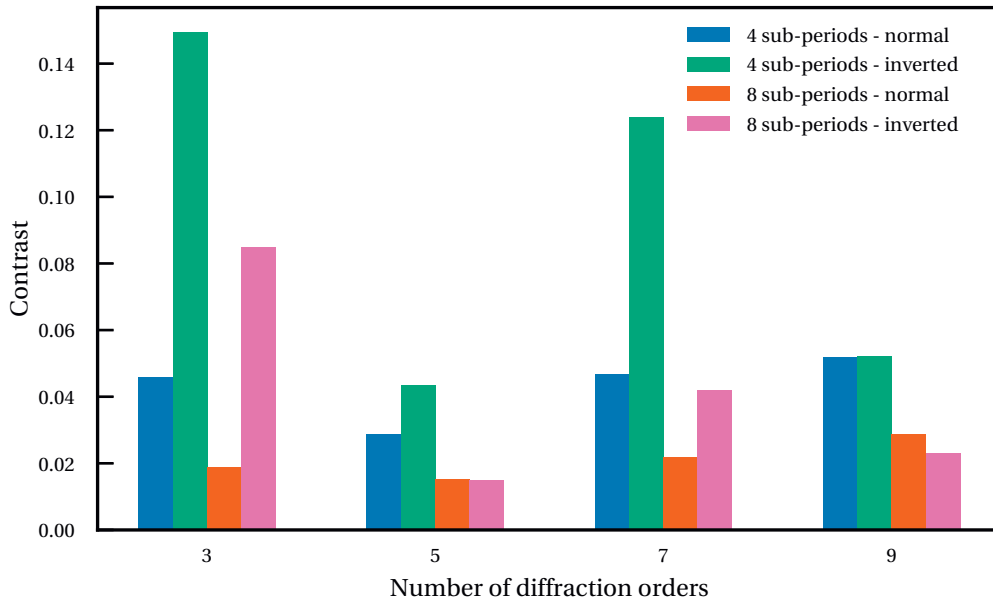

Figure 3.7 – Contrast of different Dammann gratings producing 3, 5, 7 and 9 homogeneous diffraction orders. The gratings are simulated by RCWA with a sub-period of size 1.95 μm and 7.8 μm wavelength. The grating periods are 59 μm, 404 μm, 308 μm and 944 μm for the 8 sub-periods designs, respectively. These values are halved for the 4 sub-periods designs.

3.3.5 Error sensitivity

The sensitivity of the design towards errors in fabrication is evaluated by modifying the optimized fill factor and thickness values. Figure 3.8 shows the effect on contrast and reflectivity of an error on the fill factors. The RCWA simulations are realized for a three beam Dammann grating with 200 μm period, 1.95 μm sub-periods at 7.8 μm wavelength. Since the design is originally optimized for contrast, the zero position does not exactly correspond to the lowest reflectivity. An error on the low index fill factor is less damaging to the contrast than an error on the high index fill factor. This can be explained by the fact that the optical path is proportional to the effective index and therefore changes more for the high fill factor. When both fill factors are changed in the same way, the contrast increases less than when only the high fill factor value is modified. In terms of phase difference, this means that the error is less important. However, since both optical paths are moved away from the $\lambda/4$ value, the reflectivity increases dramatically. Figure 3.9 shows the effect on contrast and reflectivity of an error on the fill factors.
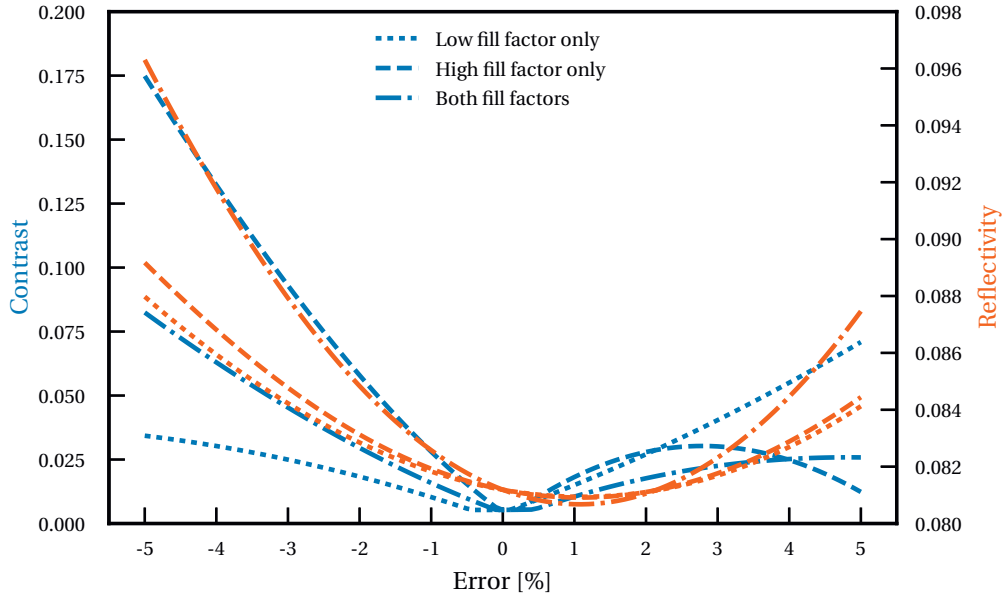
Figure 3.8 – Effect of a fill factor value error on the contrast (blue) and reflectivity (orange). The simulations are realized for a three beam Dammann grating with 200 μm period and 1.95 μm sub-periods at 7.8 μm wavelength. The curves show the variation of only the low fill factor, only the high fill factor and both fill factors at the same time.
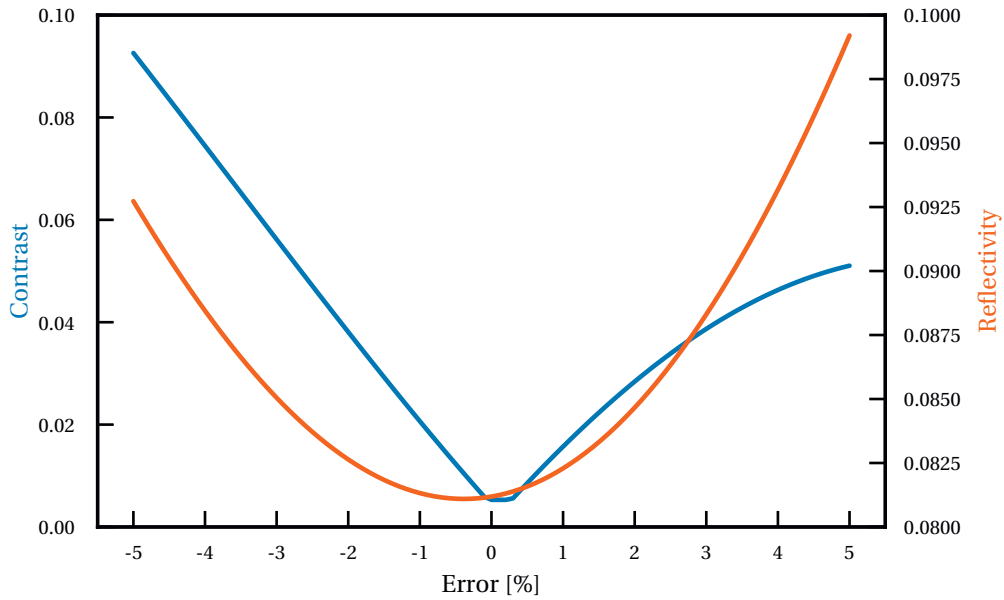

Figure 3.9 – Effect of a thickness error on the contrast (blue) and reflectivity (orange). The simulations are realized for a three beam Dammann grating with 200 μm period and 1.95 μm sub-periods at 7.8 μm wavelength.

3.4 Fabrication

3.4.1 Process steps

The grating is fabricated in silicon. The main process steps are described in figure 3.10. The silicon wafer is first coated with e-beam resist. The resist is then patterned and developed. A chromium mask layer is evaporated on the substrate. A lift-off procedure is applied to the mask. The pattern is etched through silicon using a reactive ion etching process with a plasma of C_3F_8 and SF_6 gases. The remaining chromium is removed with $HClO_4$ and $(NH_4)_2Ce(NO_3)_6$. The following sections describe in more details the fabrication steps.

3.4.2 Patterning

The patterning of the structure is realized with a Raith 150 e-beam lithography (EBL) system. We use a layer of ZEP520A positive EBL resist spin-coated at 7000 rpm and pre-baked for 5 min at 180 °C. The exposure mask file is realized using a script that generates a Dammann grating design according to table 3.1. The script defines the areas to be exposed by EBL. The sub-periods and fill factors are set according to the RCWA simulations. The script fits an integer number of sub-periods into the different phase areas, rounding the desired period. Every sub-period is itself a binary structure with the required fill factor. The resulting mask design is shown in figure 3.11. In this example, the design period is 1.4 μm and 2.2 μm and the fill factors are 0.525 and 0.69 for the low and high index areas, respectively.

The EBL resist is then exposed to the electron beam. The required dose is determined by a dose test in which the same test pattern is repeated with different exposures. It was found that a dose of $32.4\,\mu C\,cm^{-2}$ and $30\,\mu C\,cm^{-2}$ provided the best results for the low index and high index areas, respectively. The lower dose required for the high index area can be explained by the larger fill factor. Some of the electrons are backscattered after reaching the silicon and expose the resist outside of the pattern. When the exposed surface is larger, there are more electrons leaking into the neighbouring area and the required dose diminishes slightly.

After exposure, the resist is developed for one minute in n-amyl-acetate and rinsed for one minute in a mixture of methyl isobutyl ketone (MIBK) and isopropyl alcohol (IPA) with a 9:1 ratio. The exposed resist dissolves in amyl-acetate and leave the silicon under it open. After this step, the sample is cleaned for 30 seconds in a O_2 plasma in order to remove residual resist[92].

3.4.3 Dry etching

The most critical part of the fabrication process is the dry etching. The inductively coupled plasma (ICP) reactive ion etching (RIE) can be used for silicon etching. The advantage of RIE over wet etching is the generally more anisotropic behaviour. It relies on the the generation of a plasma from gas molecules that are accelerated towards the substrate. The accelerated ions

ZEP520A

Si

270nm

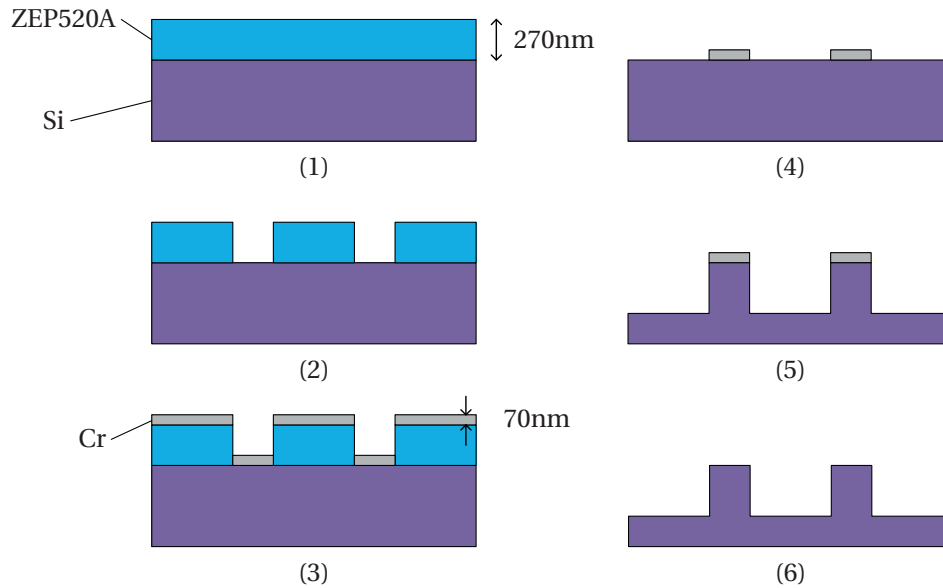(1)

(2)

Cr

70nm

(3)

(4)

(5)

(6)

Figure 3.10 – Main fabrication process steps of the binary structures: (1) spin-coating of ZEP520A resist on a silicon wafer at 7000 rpm followed by 5 min pre-bake at 180 °C; (2) e-beam patterning and development of the resist in amyl-acetate for 1 min; (3) evaporation of a chromium mask on the substrate; (4) removal of the ZEP520A and excess chromium by lift-off in N-Methyl-2-pyrrolidone (NMP); (5) dry etching of the substrate (6) Removal of the chromium mask with mixture of perchloric acid and ceric ammonium nitrate.

chemically interact with the substrate surface and alter it. The Bosch process is a particular technique of dry etching which takes advantage of sidewall passivation[93]. The passivation results from the condensation of etching by-products on the walls[94], protecting them from the reactive ions. This effect increases the anisotropy of the etching process and allows to etch deep structures with great aspect ratios.

The Bosch process is realized in two alternating steps. In the first step, silicon is etched with a SF_6 plasma for several seconds. The gas is then switched to C_4F_8, which produces a passivation layer on the structure. When the gas is switched back to SF_6, the passivation layer on the bottom of the trenches is damaged by the incoming ions. This leaves the bottom of the trenches open to the chemical etch while the sidewalls are kept protected. The Bosch process has been used to etch structures as deep as a full wafer thickness[94]. A similar effect can be obtained by using a mixture of those gases at the same time without the alternating steps. This etching method is called pseudo-Bosch. The etching depths achieved are much smaller than with the Bosch process. However, the process is less complex to implement and is therefore preferred. The C_4F_8 can also be replaced with C_3F_8. For the fabrication of our structures, we use the pseudo-Bosch method with a plasma of C_3F_8 and SF_6 gases. The etching is realized with a STS Multiplex ICP RIE machine. The following sections describe the effects of the main process parameters on the final structures. The detailed etching recipe used is described in
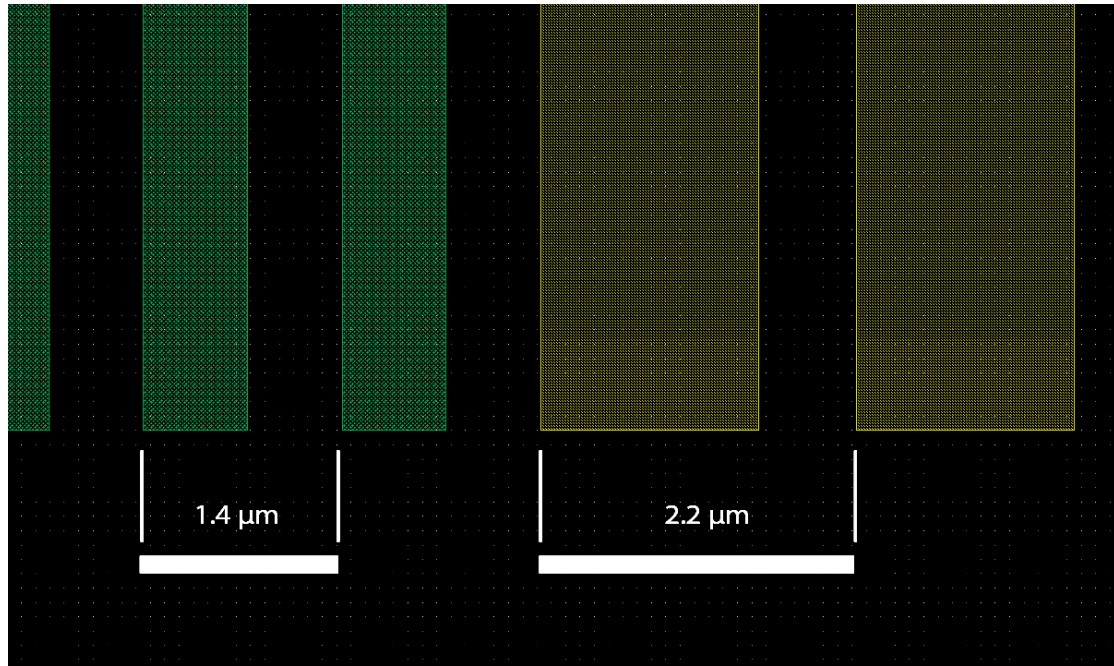
Figure 3.11 – Bottom edge of the EBL exposure pattern showing both sides of an inflection point of the design with two different phase coding areas. The green sub-grating has a period of 1.4 µm and a fill factor of 0.525. The yellow sub-grating has a period of 2.2 µm and a fill factor of 0.69. The exposure doses are $32.4\,\mu\mathrm{C\,cm^{-2}}$ and $30\,\mu\mathrm{C\,cm^{-2}}$ for the green and yellow areas, respectively.

appendix A.

Gas ratio and flux

The parameter that has the most influence on the etching process is the gas ratio. With a large SF_6 concentrations, the protective layer does not form and the etching becomes isotropic. On the contrary, with large C_3F_8 concentrations, the protective layer diminishes the etch rate and gives an inverse taper shape to the structure. Figure 3.13 shows the effect of the SF_6:C_3F_8 ratio on the etching process. An increase of gas flux increases the etch rate but is eventually limited by the capacity of the vacuum pump to keep the low process pressure constant.

Etch mask

The mask used for the etching step should offer a good selectivity with silicon. The effect of etch mask on aspect ratio and wall angle has been extensively studied by Henry[95]. Masks made of resist or SiO_2 are usually preferred because they require less processing steps. Unfortunately they tend to provide lower selectivity which limits the etch depth. For high aspect ratios, metallic masks are preferred. Nickel, alumina and chromium were considered for the etch
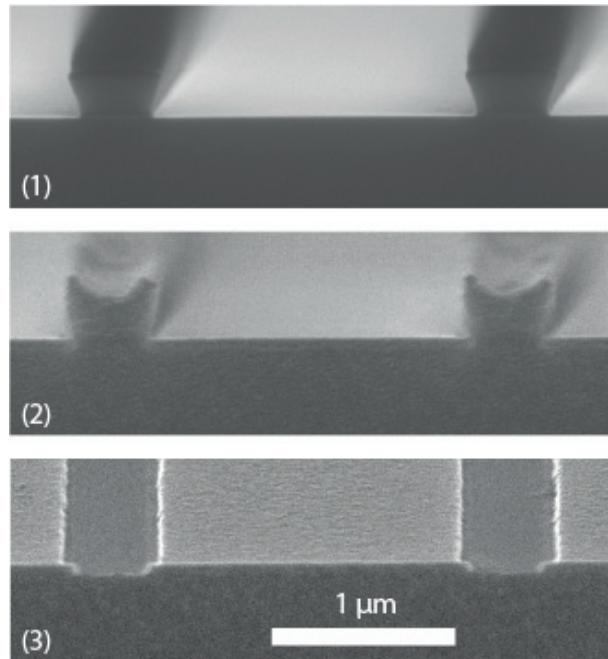
Figure 3.12 – Scanning electron microscope (SEM) pictures of the chromium mask deposition steps: (1) patterned and developed ZEP520A resist on top of a silicon wafer; (2) evaporated chromium layer on top of the substrate and e-beam resist; (3) chromium layer left on the substrate after lift-off.

mask. Nickel and chromium masks offer virtually infinite selectivity because they are very hard and chemically resistant. This allows to etch deep trenches while keeping a small mask thickness. However, some undercutting occurs close to the mask, possibly due to electric field perturbation effects caused by the metal[95]. Alumina offers an alternative to nickel or chromium which causes less undercutting. The alumina mask is less resilient to milling than the metals and its thickness diminishes during the etching process. The selectivity of an alumina mask for silicon etching was measured to be 1:142, which requires a larger thickness than the metal masks. We could observe that the alumina mask was also more brittle and had a tendency to break during etching close to its edges. This results in an unwanted enlargement of the trenches. Another inconvenient of alumina is the high temperature required for its evaporation on the substrate. The heat generated by the evaporation process is too high and alters the patterned resist. The etch mask is made of chromium, which was found to cause less undercutting than nickel.

Feature size

When etching small features - smaller than $2\,\mu m$ approximately - the etch depth depends on the gap size. A larger gap size results in a deeper etching. Figure 3.14 shows the differences in etching depth with different mask openings. Since the anti-reflective design is based on two different fill factors, the mask openings should be different if the sub-period is kept constant.
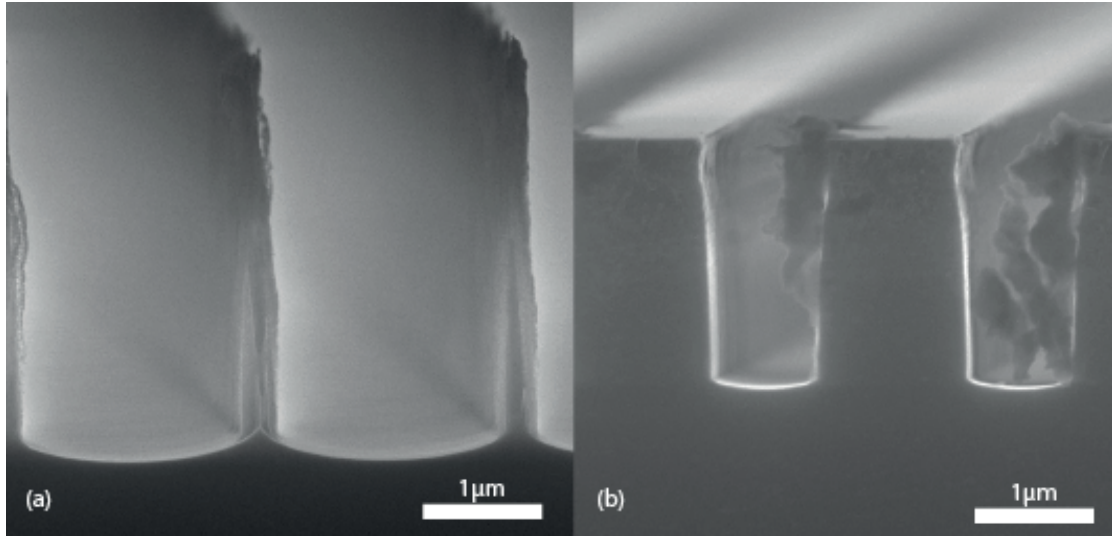
Figure 3.13 – SEM pictures of etched structures: (a) etching result with a 10:40 ratio of SF_6:C_3F_8; (b) etching result with a 6:34 ratio of SF_6:C_3F_8. The flakes that can be observed are part of the passivation layer forming during the etching process. They detach when the sample is cleaved for the observation.

This would result in different etching depths for the different areas of the grating. To avoid this effect, the sub-period of the small index area is reduced so that the openings in both regions are of similar size.

Pressure

At low pressures, the etching is more physical than chemical because the ions have more energy. An increase of pressure lowers the physical etching and increases the chemical etching. When the pressure is too high, the ions are less directional and the etching becomes more isotropic.

The effect of process pressure on the sidewall angle is described in figure 3.15. From this graph, the process pressure providing the best results in terms of sidewall angle is 21 mtorr. At lower pressures, the ions are more ballistic and should therefore give a better sidewall angle. However, less passivation layer forms on the walls, which in turn reduces the anisotropy. A larger under-etching effect was observed at lower pressures.

Etching duration and sample temperature

The platen holding the sample to be etched inside the RIE machine is cooled with an external chiller. It was observed that lowering the chiller temperature from 20 °C to 10 °C provided straighter walls while keeping all other process parameters constant. The passivation layer formation is increased at lower temperatures, which explains these results. It could also be
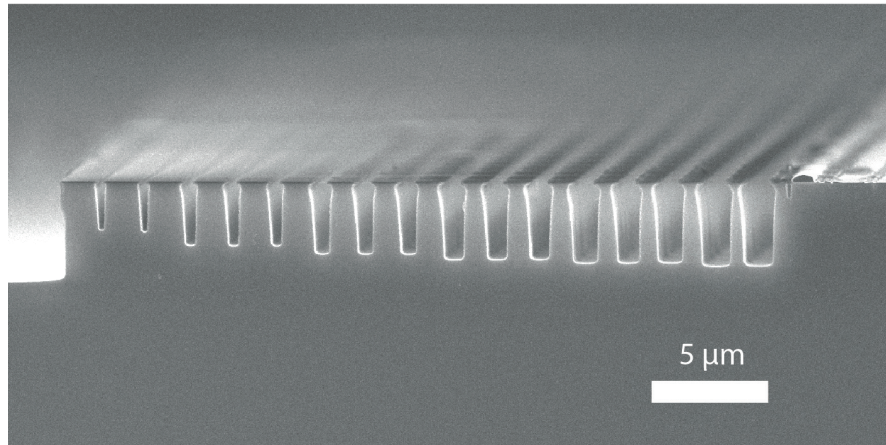
Figure 3.14 – Effect of mask gap size on the etching depth. The feature period is $2\,\mu$m.

observed that splitting the etching process in two or three parts with a 5 min pause provided better results than a single step of the same overall length. This is probably due to the sample overheating during the process, which inhibits the formation of the passivation layer.
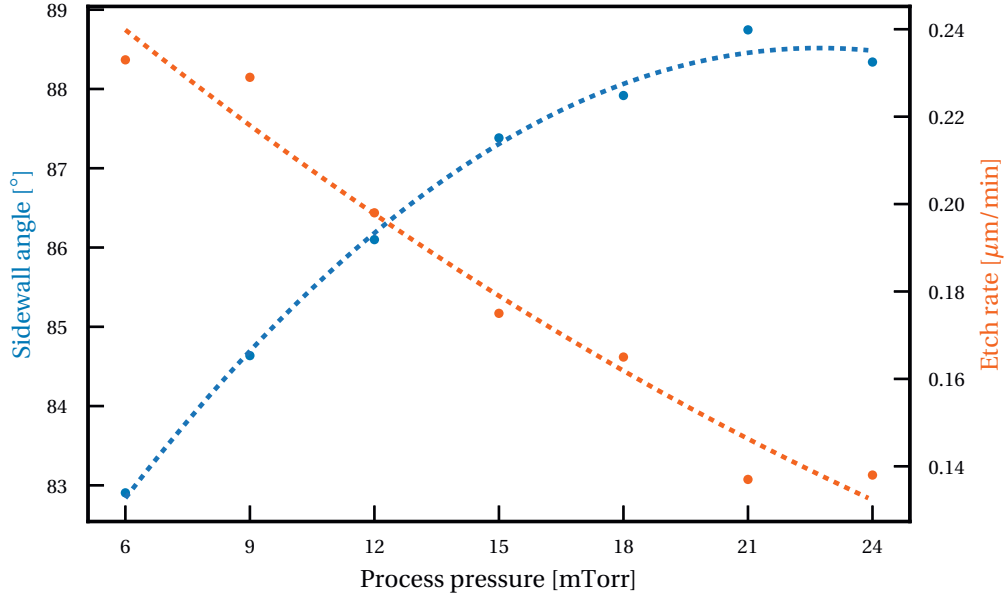
Figure 3.15 – Effect of the process pressure on the sidewall angle (blue) and etch rate (orange) of the fabricated structures.

3.5 Results

3.5.1 Fabrication

The fabricated three beam Dammann grating is shown in figure 3.16. The grating thickness is 3.863 µm, which is 2.00 % smaller than the design value. The small fill factor is 0.510, which is 2.93 % smaller than the design value. The high fill factor is 0.653, which is 5.35 % smaller than the design value. The small period is 1.39 µm and the large period is 2.22 µm.

3.5.2 Setup

The setup is described in figure 3.17. The laser source is a EC QCL set at 7.8 µm producing a linearly polarized output. The detailed laser setup is described in chapter 1, figure 1.11. The beam intensity is modulated by a mechanical chopper. The collimated laser beam is focused using a 152.4 mm focal length 90° off-axis gold coated parabolic mirror. The beam is filtered using a 300 µm pinhole at the focal point. The sample is positioned 150 mm away from the focal point and pressed against a thin aperture of 3 mm diameter. In theory, the sample should be illuminated by a collimated beam but for practical reasons the light is slightly diverging (0.57°). The divergence is however smaller than the angle between the diffracted beams (2.24°), which doesn't affect the final measurement. A photovoltaic MCT detector is mounted on a two axis scanning stage positioned 150 mm away from the sample. The detector is connected to a SR830 lock-in amplifier synchronized with the chopper. The detector is
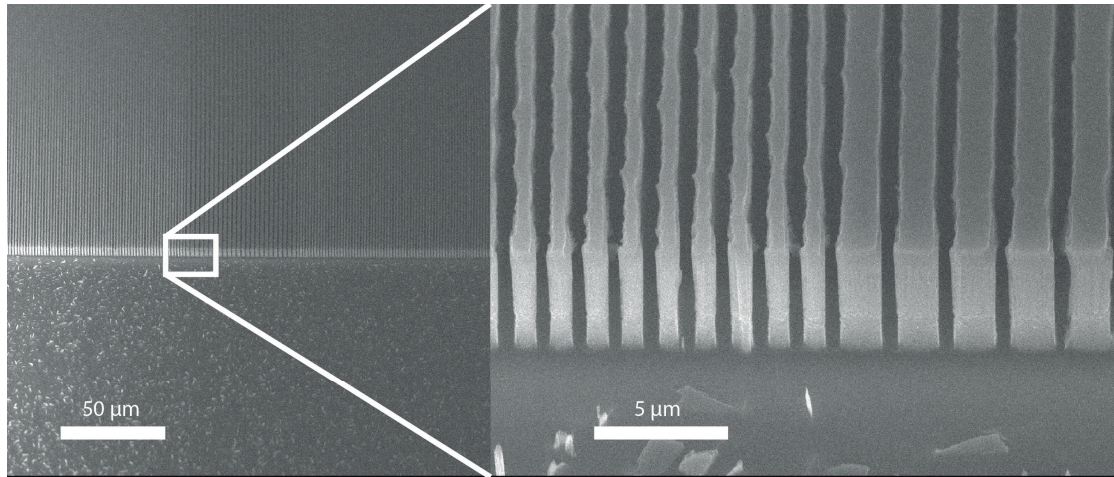
Figure 3.16 – SEM image of the fabricated Dammann grating. The areas on the left and right parts of the inset are the low and high refractive index areas, respectively. The grating thickness is 3.863 μm. The small fill factor is 0.510 and the high fill factor is 0.653. The small period is 1.39 μm and the large period is 2.22 μm. The bottom of the picture shows some 'grass', which only appears in the non-patterned area.

scanned using the two-axis stage to form an image of the far field pattern generated by the grating. For the reflectivity measurement, the detector is replaced by a power meter pressed against the sample and aperture. The power transmitted through the grating is compared to the transmission of an unpatterned silicon wafer.

3.5.3 Measurements

Figure 3.18 (a) shows the far-field intensity measured for the three-beam Dammann grating. The concentric disks are caused by the circular aperture placed after the sample. Figure 3.18 (b) shows the vertical line average of the far-field pattern. The intensity of the diffraction orders is evaluated by integrating the beam profiles. Figure 3.18 (c) compares the relative intensity of the diffraction orders between the design simulation and the measurements. The diffraction grating transmits 18 % more light than the plain silicon wafer.

3.5.4 Discussion

The diffraction orders intensity and contrast are in good agreement with the simulations. The measured contrast is 10.4 % and the contrast without the zero order is equal to 2.4 %. The simulated values are 4.3 % and 0.01 % with and without zero order, respectively. The transmitted light with the grating is increased by 18.0 %, which is lower than the expected 28.8 % from the RCWA simulation. These values correspond to a reflectivity of 17.4 % and 9.8 %, respectively. The reflectivity of the structure is inferior to the simulated value. This can be explained by the thickness error in the fabrication process, as well as the fill factor error. An
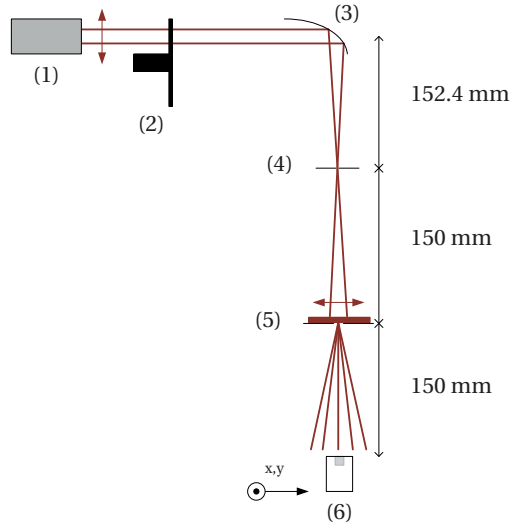
Figure 3.17 – Schematic of the measurement setup: (1) Tunable QCL setup (2) Mechanical chopper (3) Parabolic mirror (4) Pinhole (5) Sample and aperture (6) Photovoltaic detector on two-axis stage. The double arrows represent the light polarization.

error in thickness modifies the optical path of both areas at the same time. This has a higher impact on the reflectivity than on the contrast because the phase difference is not significantly modified. In addition to this, the Dammann grating design itself is relatively robust in terms of phase difference error, thanks to the general properties of DOEs[49]. If the grating thickness is not correct, the phase error will mostly affect the zero order amplitude, keeping a low contrast of the other symmetrical diffraction orders.

(a) Far-field pattern
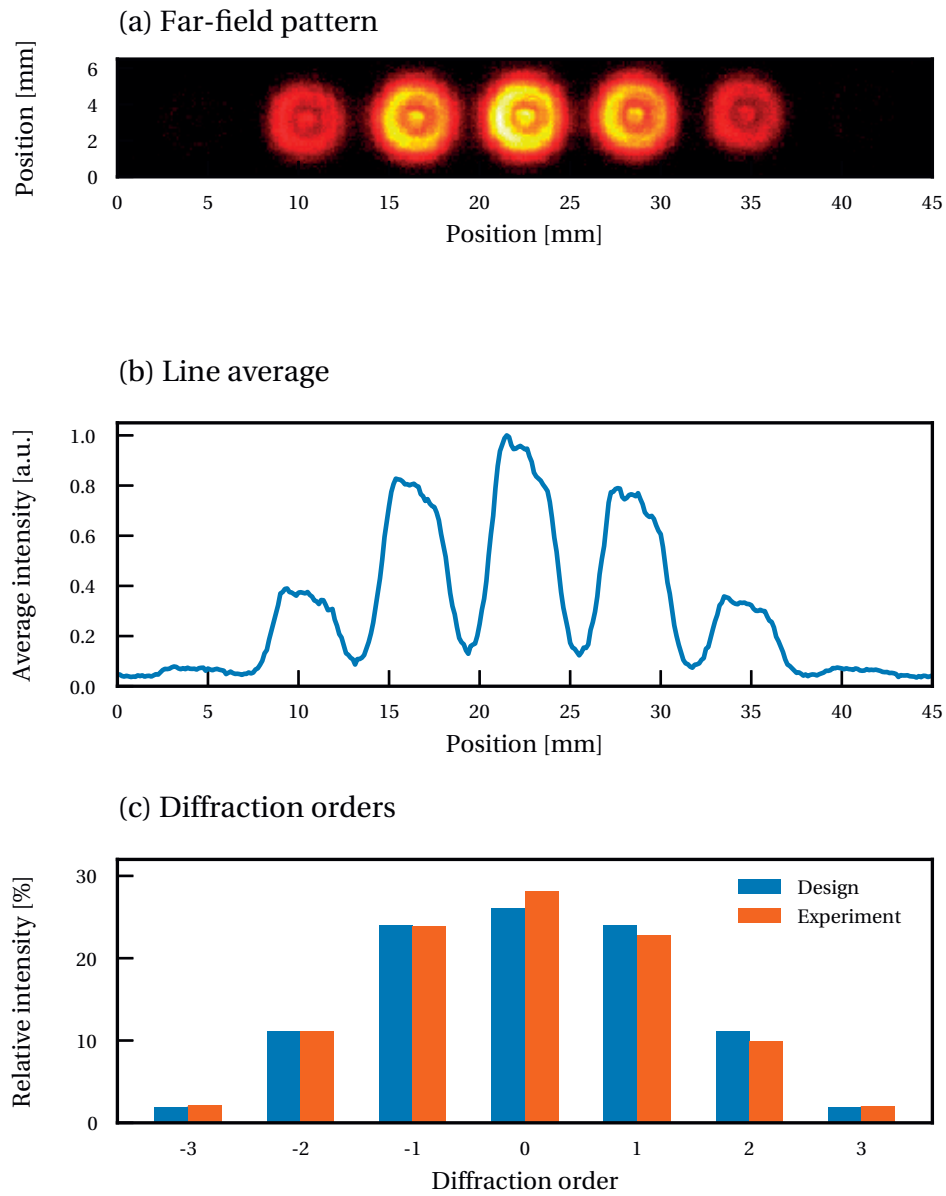

(b) Line average

(c) Diffraction orders

Figure 3.18 – (a) Measured intensity of the far-field pattern produced by the three-beam sub-wavelength Dammann grating; (b) vertical line average of the far-field pattern; (c) relative intensity of the measured diffraction orders compared with the RCWA simulation of the design.

3.6 Outlook

The dry-etching process can be further improved to better match the design. An etching made with the Bosch process could also be used to produce deeper structures with larger aspect ratios. A better control of the e-beam resist patterning and mask deposition could enable the fabrication of structures with smaller sub-periods, which provide better contrast.

The fabrication of two-dimensional patterns can be further studied. Some attempts have been made with two-dimensional Dammann gratings with circular or square features, as described in figure 3.19. The etching process however requires improvement because the achieved thickness is currently not large enough. The fabrication of birefringent structures such as half-wave plates and other diffractive designs can be further developed.

3.7 Conclusion

In this chapter, a method to design low reflectivity binary diffractive elements using sub-wavelength structures is presented. This method is particularly interesting for optical elements made of high refractive index materials in the MIR. The performance of the designed gratings is analyzed according to different parameters such as grating depth and period. The fabrication of a three diffraction orders Dammann grating in silicon is described. The fabricated element is measured and provides 18 % more light transmission than a similar silicon wafer with no patterning. The contrast provided by the diffractive element is 10.4 percent, which is higher than the expected value but can be explained by the mismatch between the design and the fabricated structure. Finally, further developments of diffractive structures containing sub-wavelength features are proposed.

The following chapter introduces a different type of passive optical components. Multi-layer structures allowing the propagation of surface waves are presented. As with diffraction gratings, they rely on a periodic structure. In this case however, the periodic arrangement of thin layers – also called one-dimensional photonic crystal, is parallel to the surface of the optical element.
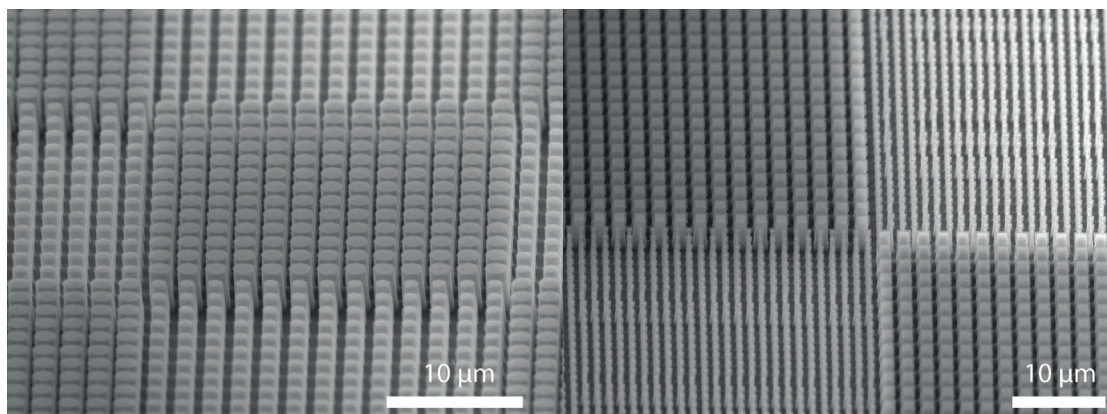
Figure 3.19 – SEM images of two-dimensional Dammann gratings made of cylindrical and square sub-wavelength silicon pillars.

4 Observation of mid-infrared Bloch surface waves

4.1 Introduction

The term Bloch surface wave (BSW) refers to an electromagnetic wave propagating at the interface of a periodic stack of dielectric materials deposited on a substrate. The multi-layer stack is composed of two materials having a refractive index difference. The periodic stack acts as a distributed Bragg reflector (DBR). Under certain conditions, light can be guided in a surface mode, at the interface between the DBR stack and the outside medium under total internal reflection (TIR).

The first experimental observation of a BSW has been reported by Yeh et al[96]. A multi-layer stack consisting of 12 pairs of GaAs-AlGaAs was used for the observation of surface waves at 1.15 µm wavelength.

BSWs can be compared to surface plasmon polaritons (SPPs) but benefit from many advantages[97, 98]. SPPs propagate at the interface of a metallic layer and a surrounding medium. The metallic layer properties depend on the material used and cannot be modified except for their thickness. In a dielectric multi-layer, the operating wavelength is not bound to the materials and can be selected at will according to the structure design[99]. BSWs can also propagate over distances at least one order of magnitude larger than SPPs (> 2.5 mm), because of the stronger absorption occurring in metals[100].

The objective of this work is to demonstrate the feasibility of a BSW platform in the MIR for spectroscopic measurements on a surface. The high electric field enhancement at the interface provided by a BSW multi-layer is a key advantage for the detection of analytes on a surface.

Multi-layer designs exhibiting BSW occurrence have been demonstrated in the visible or NIR spectrum. To the best of our knowledge, this work constitutes the first demonstration of BSW in the MIR. The work presented in this chapter has been submitted to the journal ACS Photonics.
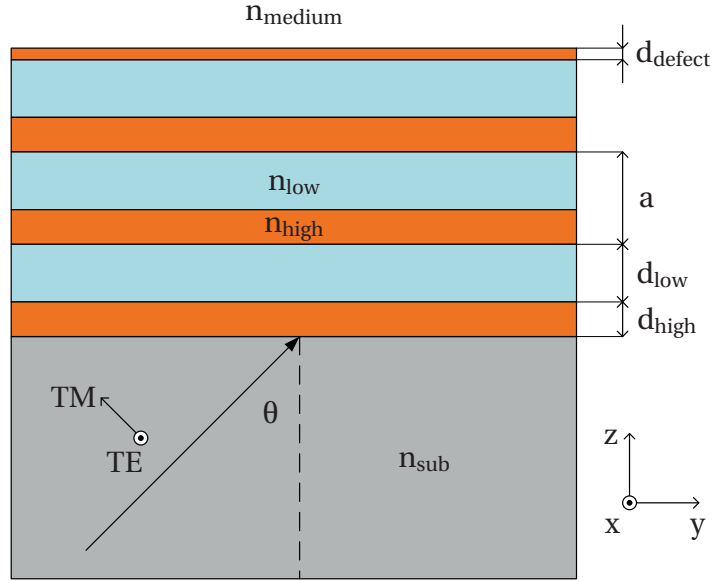
Figure 4.1 – The multi-layer structure is deposited on a substrate of index n_{sub}. The layers are made of high (n_{high}) and low (n_{low}) index materials with a thickness of d_{HIGH} and d_{LOW}, respectively. A high index defect layer of thickness d_{defect} is deposited at the top of the stack. The multi-layer is in contact with an external medium of index n_{medium}. The light is incident at an angle θ inside the substrate and can be TE or TM polarized.

4.2 Dielectric multi-layer design

4.2.1 Design principle

The multi-layer stack properties can be described similarly as a DBR or one-dimensional photonic crystal. The stack is composed of a periodic arrangement of N pairs of low and high index dielectrics such that $a = d_{high} + d_{low}$ where a is the thickness of the pair or 'lattice constant', d_{high} and d_{low} are the thicknesses of the low and high dielectric layers, respectively. When each individual layer has an optical thickness close to $\lambda_0/4$, an infinite stack acts as a perfect mirror at normal incidence due to the presence of a photonic band-gap around λ_0[101, 11]. The width of the band-gap increases with the difference of refractive indices. The mirror reflectivity increases with the number of pairs and the refractive index difference.

The addition of defects in the multi-layer periodicity allows evanescent modes within the band-gap to exist in the multi-layer structure. A finite stack is a truncation of the infinitely periodic structure, which can also be seen as a defect. When considering off-axis propagation, the complete band-gap ceases to exist. There are however combinations of wavelengths and incident angles that are still forbidden. If an isolated defect mode exists within the angle-wavelength combination, the incident light can couple in and propagate laterally. This coupling only happens under the condition that the y axis component of the incident light

wavevector matches the propagation constant of the surface mode. The abrupt termination of the multi-layer periodicity - i.e. a finite number of pairs - is equivalent to a defect on the stack surface, which leads to the existence of a surface mode[102, 99]. By carefully selecting the parameter a, it is possible to define an angle and wavelength combination where a BSW propagates in the surface defect mode of the multi-layer. The structure is described in figure 4.1. The addition of a high-index defect layer of thickness d_{defect} allows to optimize the shape of the surface mode and push the evanescent tail outside of the structure.

4.2.2 Mid-infrared materials

The materials selected for the dielectric multi-layer stack should offer good transmission in the MIR, as well as a large refractive index difference. Typical low index MIR materials are used in multi-layer structures are YF_3 and YbF_3. Common materials for the high index dielectric are ZnS or ZnSe. We selected a combination of YbF_3 and ZnSe, which provide low absorption around 7.8 μm. The measured refractive indices are 1.5208 and 2.5819 for YbF_3 and ZnSe, respectively. The substrate is made of CaF_2 which has a refractive index of 1.37. The stacks are fabricated by ion assisted electron beam physical vapour deposition by the company Helia Photonics (Scotland). While the refractive index of YF_3 is lower than the index of YbF_3 and would therefore be a better choice, the former showed signs of stress with the CaF_2 substrate and could not be deposited.

4.3 Design characteristics

The multi-layer is deposited on a 1.1 mm thick CaF_2 substrate. It is composed of three pairs of ZnSe and YbF_3 layers of 1.08 μm and 1.77 μm thickness, respectively. An additional 239 nm thick defect layer of ZnSe is deposited on top of the stack.

The designed structure is simulated by FDFD using the commercial software CST MWS. For the simulations, the dielectric stack forms a unit cell that is infinitely periodic along the x and y axis of the surface. The reflectivity of the multi-layer is simulated for different angles of incidence and wavelengths for TE polarization. The materials are assumed to be lossless, except for the last layer of the stack. The refractive indices do not account for dispersion and their values are given in section 4.2.2. The designed structure is expected to couple light at 8 μm at an incident angle of 62.5°.

4.3.1 Dispersion

Figures 4.2 and 4.3a show the simulated reflectivity of the multi-layer for different angle-wavelength combinations. The light is TE polarized. The reflectivity is maximal above the TIR angle. When the BSW coupling conditions are met above this angle, the reflectivity drops, which indicates the penetration of the incident light into the multi-layer surface mode.
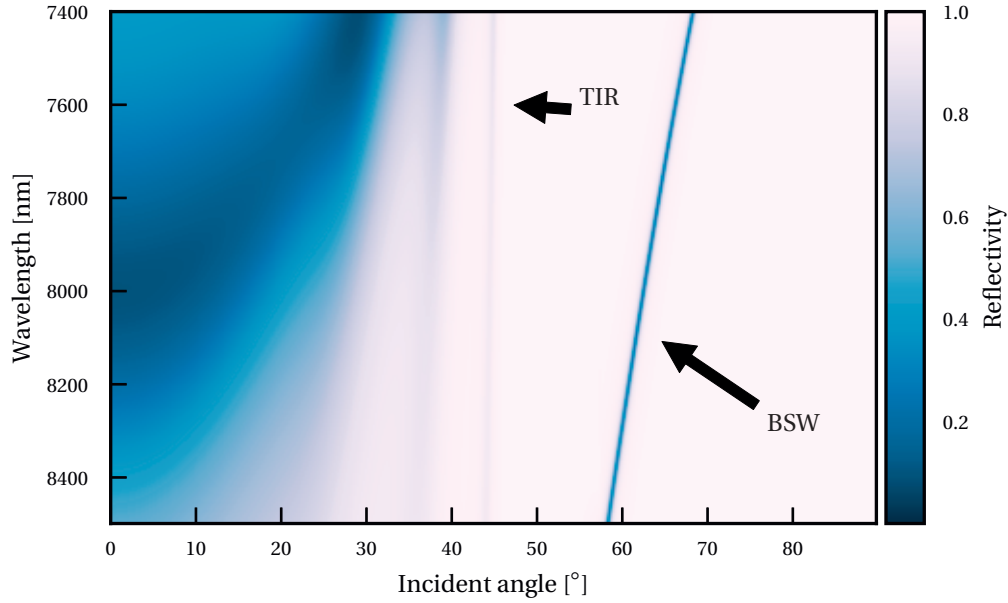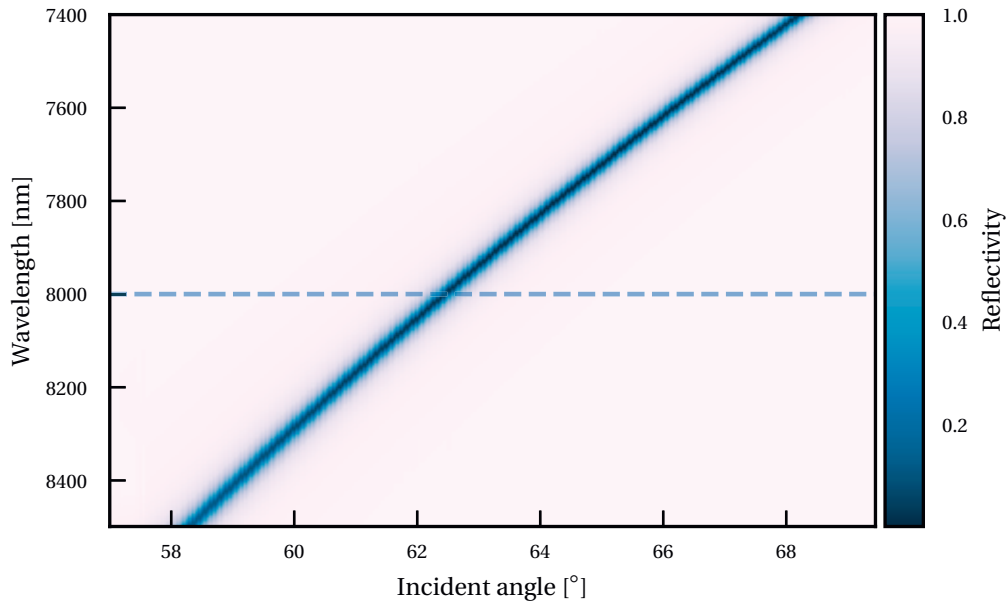
Figure 4.2 – Simulated reflectivity map in TE polarization of the multi-layer structure according to the incident angle and wavelength. The BSW coupling region can be observed after the TIR vertical line.

Figure 4.3b shows the simulated reflectivity at 8 µm according to the incident angle inside the substrate. The reflectivity dip observed at 62.5° corresponds to the light coupling into the surface mode.

4.3.2 Surface mode profile

The amplitude of the electric field is simulated at 8 µm in TE polarization with an incident angle of 62.5° and 68°. Figure 4.4 shows the square of the electric field amplitude along the multi-layer stack z axis. When the coupling conditions are met, the light propagates in the surface mode and the electric field intensity is enhanced at the interface. The electric field is exponentially decaying on both sides of the interface, which indicates the existence of a guided mode. When the coupling conditions are not met, the electric field is exponentially decaying in the air region but extended in the substrate. In this case, no guided mode can exist and the light is completely reflected[11].
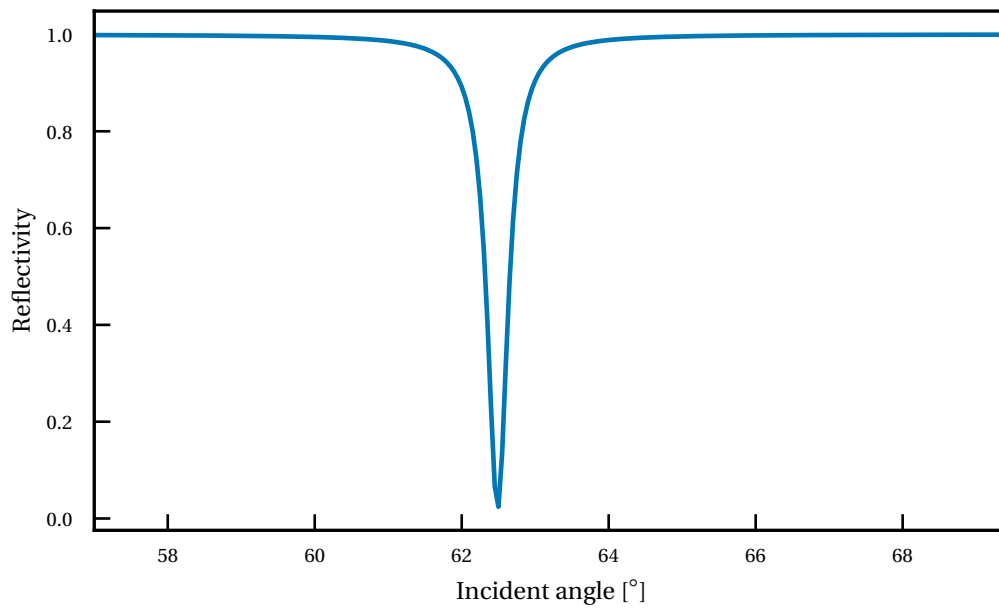
(a) Reflectivity map

(b) BSW dip at 8 μm

Figure 4.3 – Simulated reflectivity of the multi-layer stack: (a) simulated reflectivity map in TE polarization of the multi-layer structure according to the incident angle and wavelength; (b) reflectivity of the surface at 8 μm with BSW dip at a coupling angle of 62.5° corresponding to the dashed line of (a). The low reflectivity region corresponds to the incident light coupling into the surface mode.
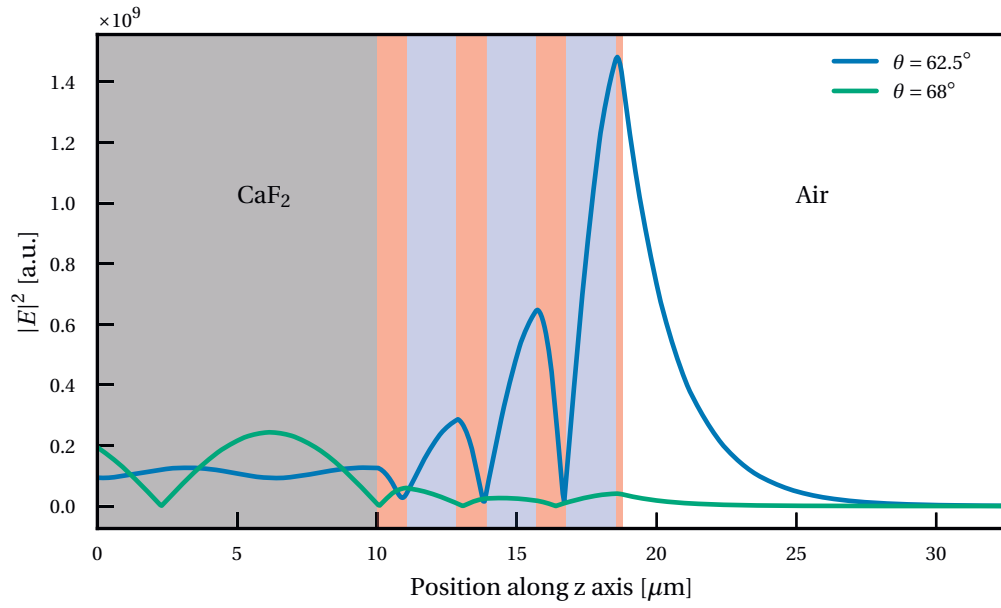
Figure 4.4 – Simulated intensity of the electric field along the axis normal to the surface of the multi-layer stack at 8 µm wavelength in TE polarization. The gray area represents the CaF$_2$ substrate. The red and blue areas represent the ZnSe and YbF$_3$ layers, respectively. The blue curve shows the electric field profile at an incident angle of 62.5°. The green curve shows the electric field profile at an incident angle of 68°.

4.4 Results

4.4.1 Setup

The reflectivity of the substrate is measured using the setup described in figure 4.5. The substrate is fixed on a CaF_2 equilateral prism in the so-called Kretschmann configuration, as described in more details in figure 4.6[103]. A droplet of paraffin oil is used as index matching liquid between the prism and the substrate. The prism is mounted on a rotational stage to allow the incidence angle of the light outside the prism θ_{prism} to be changed. The light source is a tunable QCL centered around $7.8\,\mu m$. The detailed laser setup is described in chapter 1, figure 1.11. The light is TE polarized and its amplitude is modulated by a chopper. The source is spatially filtered using a $300\,\mu m$ pinhole. The light is focused on the substrate using a parabolic mirror. The far-field amplitude of the reflected light is measured with a photovoltaic (PV) MCT detector fixed on a two-axis motorized stage placed $690\,mm$ away from the prism.

4.4.2 Measurements

The existence of a BSW on the multi-layer stack is measured through the characterization of the mode angular and spectral dispersion. The light reflected by the stack is measured at different wavelengths and incident angles on the prism. When the coupling conditions are met, the incident light propagates into the Bloch surface mode and is no longer reflected, which translates into a drop in reflected intensity, as simulated in figure 4.3b. Figure 4.7 shows the beam profile measured after reflection inside the coupling prism. The light is incident on the prism at 69°, which corresponds to an angle of 66.55° inside the substrate. The wavelength is $8.05\,\mu m$. Figure 4.7a shows the reflected profile of the prism alone. Figure 4.7b shows the reflected profile of the prism with the substrate on top. A FP resonance is visible on the picture, as well as a drop in intensity close to the 1 mm vertical position. This low intensity is due to the light coupling into the BSW.

The divergence of the incident beam allows to probe a range of up to 1.2° at the same time, depending on the outside coupling angle. The reflection spectrum according to the incident angle inside the CaF_2 substrate is measured as follows: The prism angle is first set using the rotational stage; the laser wavelength is then set to a specific value within its operating range; the photodetector is finally scanned vertically to measure the incident light intensity profile. The vertical position of the detector is converted in incident angle inside the substrate. The resulting measurements are displayed in figures 4.8, 4.9 and 4.10 for different prism coupling angles. The BSW coupling line can be observed in figure 4.8 and 4.9. The low intensity line results from the coupling into the surface mode for the specific angle-wavelength combinations. Since the prism angle is different between the two measurements, the coupling wavelengths are spectrally shifted. In figure 4.10, the coupling conditions are not met and no dip in intensity is observable over the whole range.

A FP resonance is visible across the whole measurement spectrum. This resonance is due to
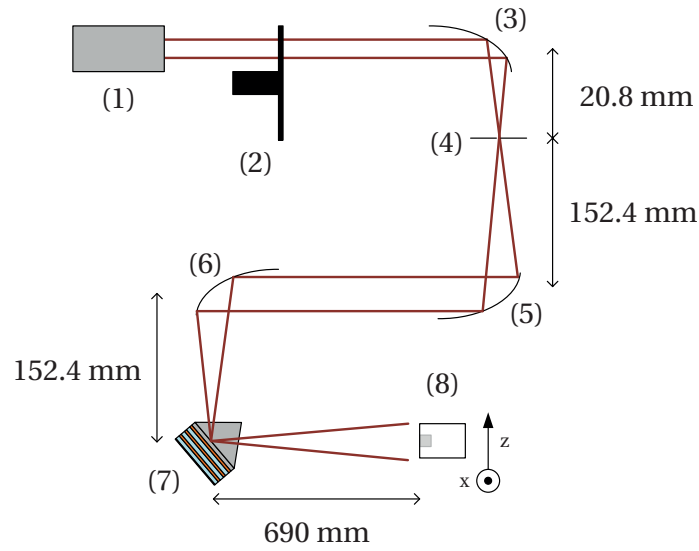
Figure 4.5 – Bloch surface wave characterization setup: (1) tunable QCL setup; (2) mechanical chopper; (3) parabolic off-axis mirror; (4) 300 µm pinhole; (5) parabolic off-axis mirror; (6) parabolic off-axis mirror; (7) CaF_2 prism and substrate with ZnSe and YbF_3 multi-layer structure on a rotational stage; (8) PV MCT photodetector on a two-axis stage.

the reflections between the prism-substrate interface and the multi-layer stack. The index matching liquid placed between the two CaF_2 elements should limit this effect. The refractive index of the paraffin oil used is different than the index of CaF_2, which generates a reflection at the prism-substrate interface.
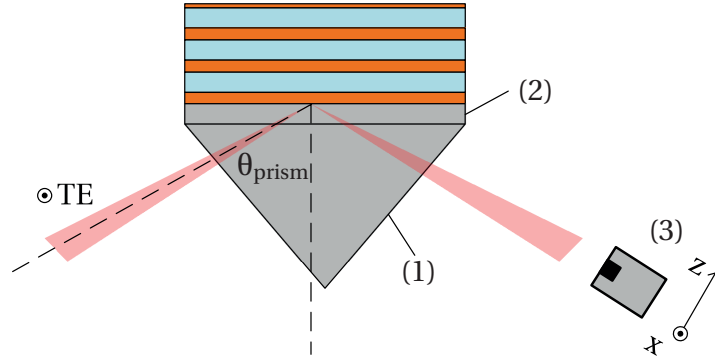
Figure 4.6 – Bloch surface wave characterization setup: (1)Equilateral CaF$_2$ prism; (2)CaF$_2$ substrate with ZnSe and YbF$_3$ multi-layer structure; (3)PV MCT photodetector on a two-axis stage. The photodetector is placed 690 mm away from the prism. TE polarized is incident on the prism at an angle θ_{prism}. This angle is slightly different than the angle of incidence θ on the multi-layer stack. The refraction at the interface between the air and the prism is neglected in this figure for simplification. The drawing is not to scale.
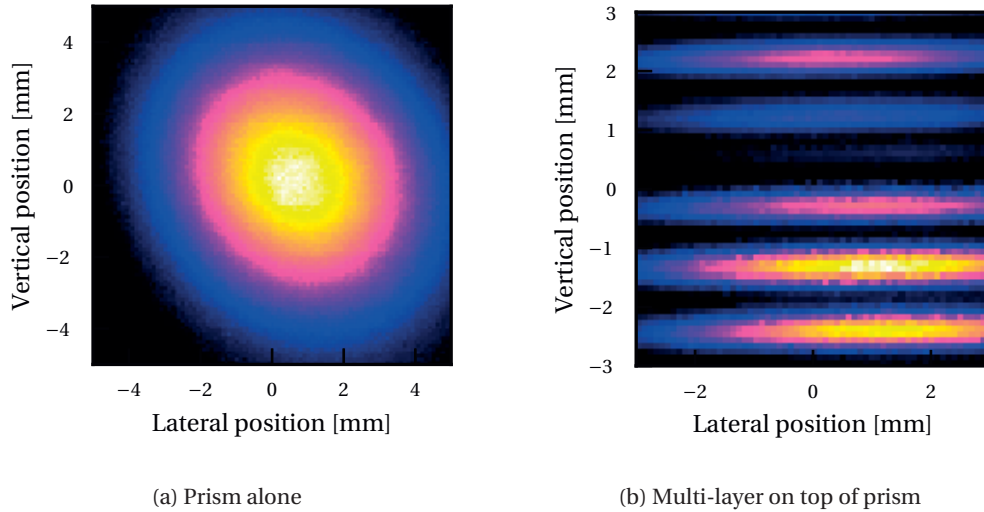

(a) Prism alone

(b) Multi-layer on top of prism

Figure 4.7 – Comparison of the reflection profiles measured at 8.05 µm wavelength at an incidence angle θ_{prism} of 69° without (a) and with (b) the substrate on top.

Figure 4.8 – Measured intensity after reflection on the substrate with multi-layer structure at an outside angle θ_{prism} of 70°. The incident angle on the graph is the angle inside the substrate. The dark line shows the angle-wavelength combinations at which the incident light couples into the surface mode and is no longer reflected. The dashed red line shows the intensity maxima of one FP resonance and allows to notice the shift occurring around the BSW coupling condition.
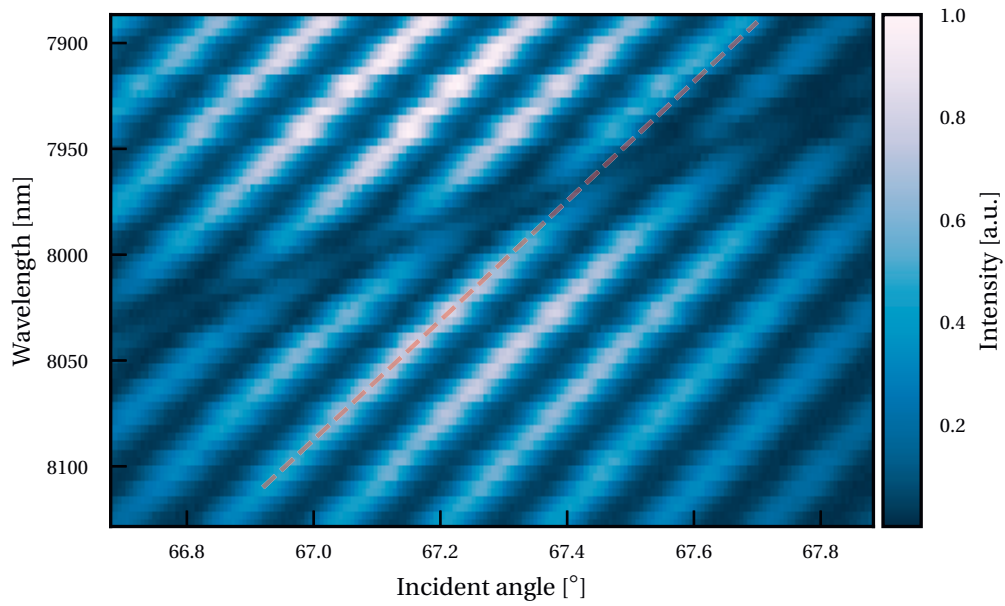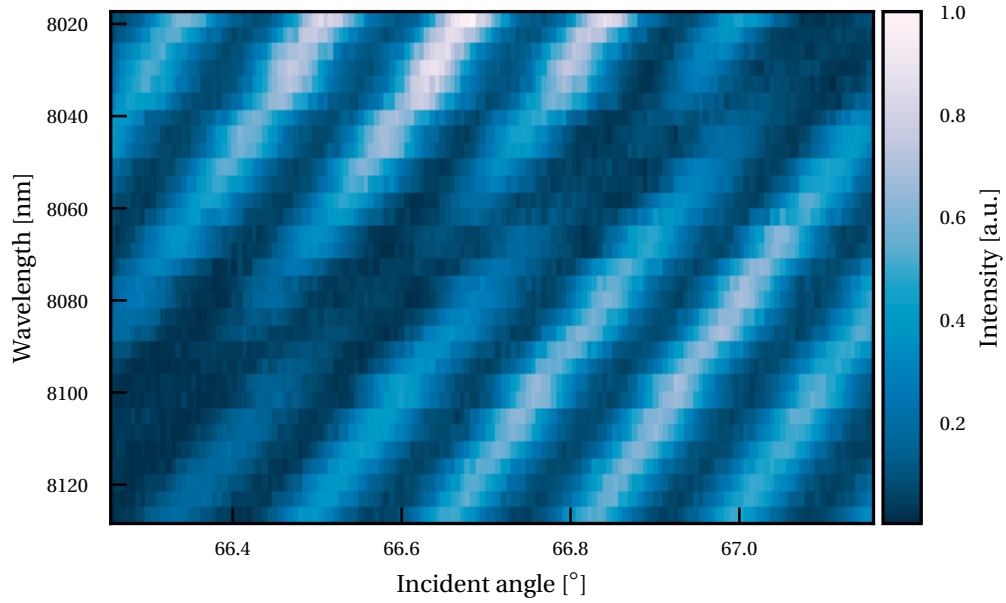
Figure 4.9 – Measured intensity after reflection on the substrate with multi-layer structure at an outside angle θ_{prism} of 69°. The incident angle on the graph is the angle inside the substrate. The dark line shows the angle-wavelength combinations at which the incident light couples into the surface mode and is no longer reflected.
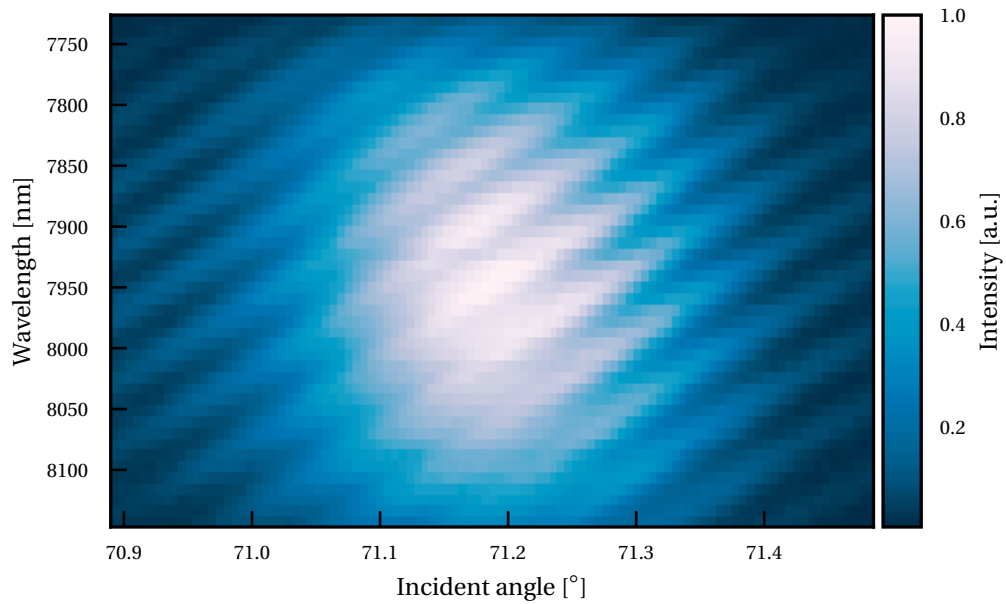

Figure 4.10 – Measured intensity after reflection on the substrate with multi-layer structure at an outside angle θ_{prism} of 75°. The incident angle on the graph is the angle inside the substrate. No coupling into the surface mode occurs at these angle-wavelength combinations.

4.4.3 Discussion

Figure 4.11 compares the simulated reflection map of figure 4.3a with the measured intensity from figure 4.8. A BSW forms on the surface of the multi-layer stack at specific incident angles and wavelengths. As expected, the spectral position of the BSW changes with the incident angle. The angle-wavelength combinations at which the incident wave couples into the surface mode are however red-shifted by approximately 0.45 μm.

Figure 4.12 shows the simulated coupling angle for the multi-layer structure as a function of defect layer thickness. It can be observed that the coupling angle is highly influenced by the precision of the fabrication. We measured the thickness of the deposited layers of a cleaved sample. The fabricated structure can be observed in figure 4.13. It can be observed that the Bragg structure is irregular and does not precisely match the design, which can explain the differences between the simulation and measurement. Taking the measured thickness values into account, a simulation of the fabricated structure is compared to the previous reflectivity measurement and displayed in figure 4.14. In this simulation, the FP resonance is also taken into account. We can observe here a better match to the measurements than in the initial design simulation, with a red-shift by only 0.18 μm or less than 3 % of the wavelength.

The FP resonance on the surface allows to observe a phase shift induced by the reflection on the multi-layer stack[104]. The intensity maxima and minima observed in figures 4.8 and 4.9 are shifted around the BSW dip. The FP maxima and minima are equally spaced in figure 4.10, away from the BSW coupling angle. The position of the maxima and minima of intensity can be determined using the Fabry-Perot equation:

$$I = \frac{I_{\max}}{1 + (2\mathscr{F}/\pi)^2 \sin^2(\phi/2)} \tag{4.1}$$

with the phase difference after a round trip

$$\phi = \frac{4\pi d}{\lambda} \tag{4.2}$$

and the finesse

$$\mathscr{F} = \frac{\pi r^{1/2}}{1 - r}, \tag{4.3}$$

where r is the reflectivity coefficient of the cavity and d is the length of the cavity[105].

The superposition of equation 4.1 and the spectral measurements of the reflectivity shows that the intensity maxima and minima are shifted around the BSW dip. This shift in spectral position of the maxima and minima $\Delta\lambda$ can be translated into a phase shift of the reflection on the multi-layer stack. Figure 4.15 shows the intensity measured at the center of the reflected spot at a 70° incidence angle on the prism. The phase shift is calculated with respect to the FP curve and plotted in orange on this figure. The wavelength is scanned over the range of
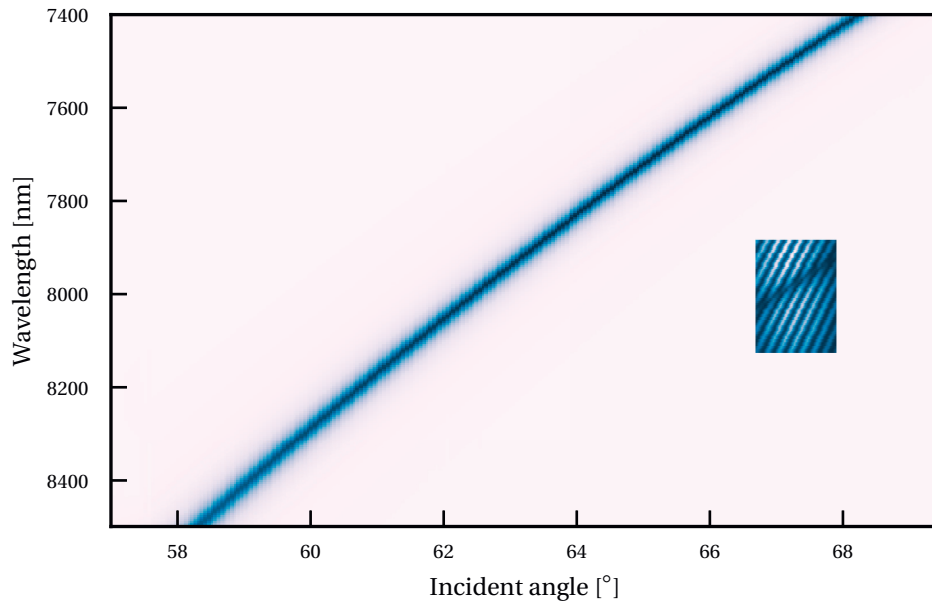
Figure 4.11 – Superposition of the simulated reflectivity and the measured intensity profile.

the tunable laser source. The FP resonance of the substrate can be observed. Equation 4.2 assumes a constant phase shift after the reflection on one of the facets of the cavity. This phase shift is however not constant around the BSW coupling condition and can be indirectly observed here.

Figure 4.12 – Simulated BSW coupling angle as a function of defect layer thickness.
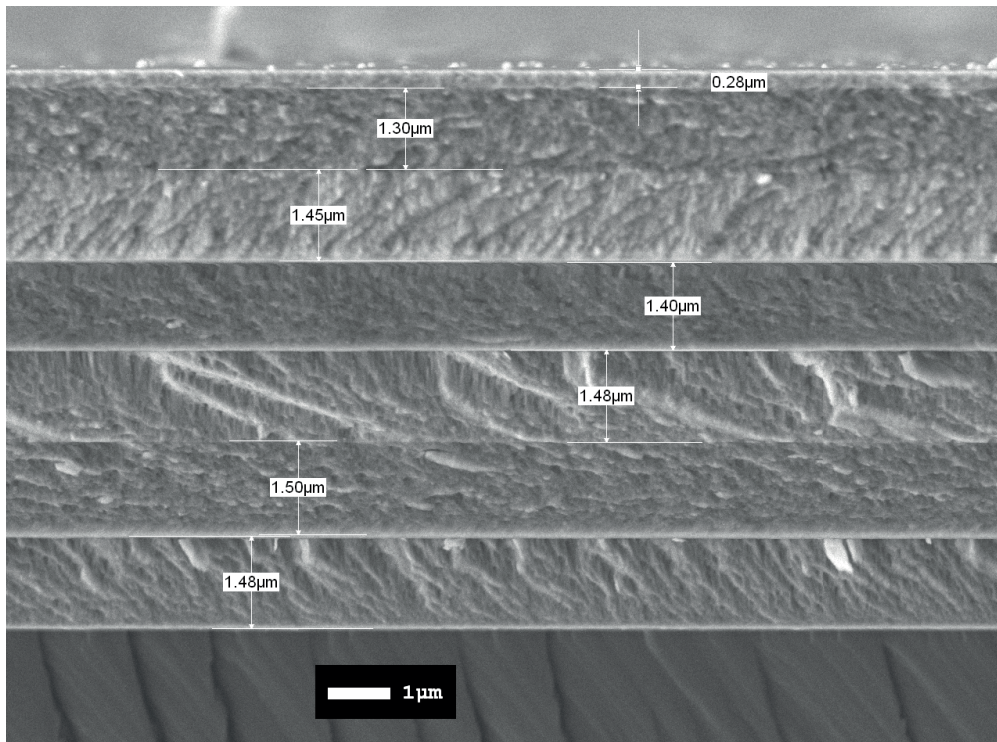
Figure 4.13 – SEM image of the fabricated multi-layer structure consisting of ZnSe and YbF$_3$ layers on top of

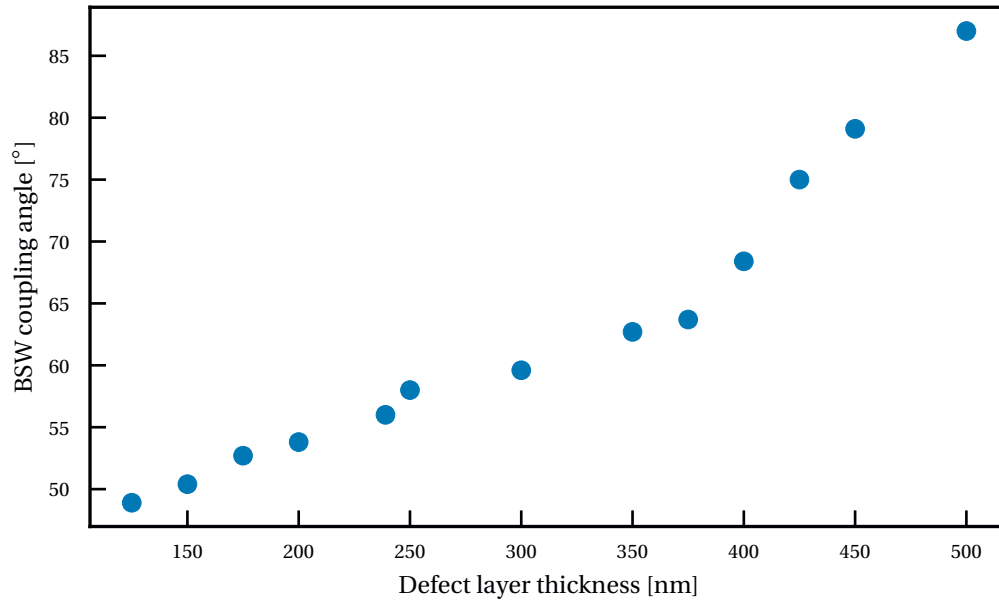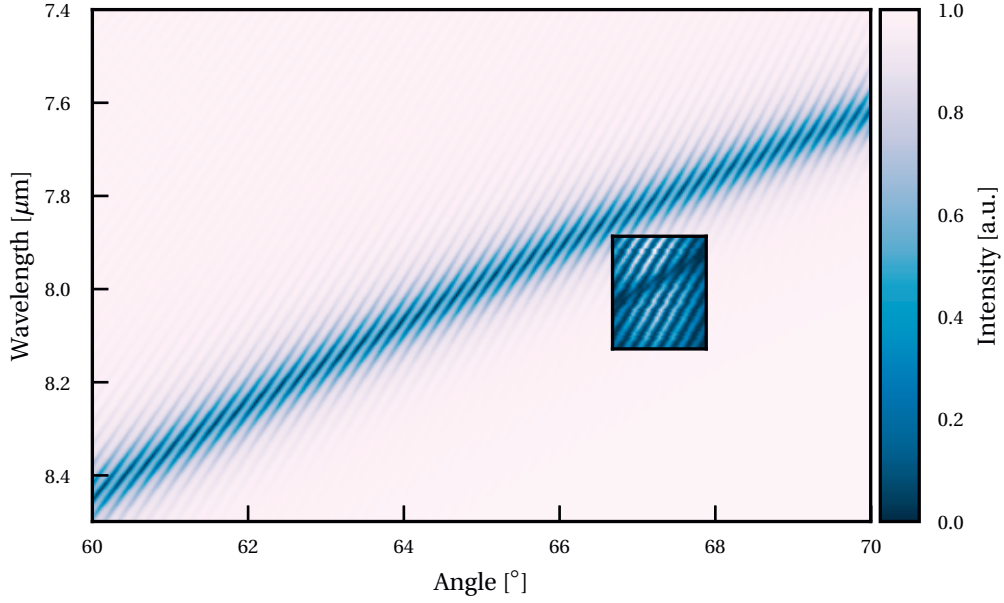Figure 4.14 – Comparison between the reflectivity simulation of the fabricated sample and the measurement. The measurement is red-shifted by about $0.18\,\mu$m compared to the simulation.
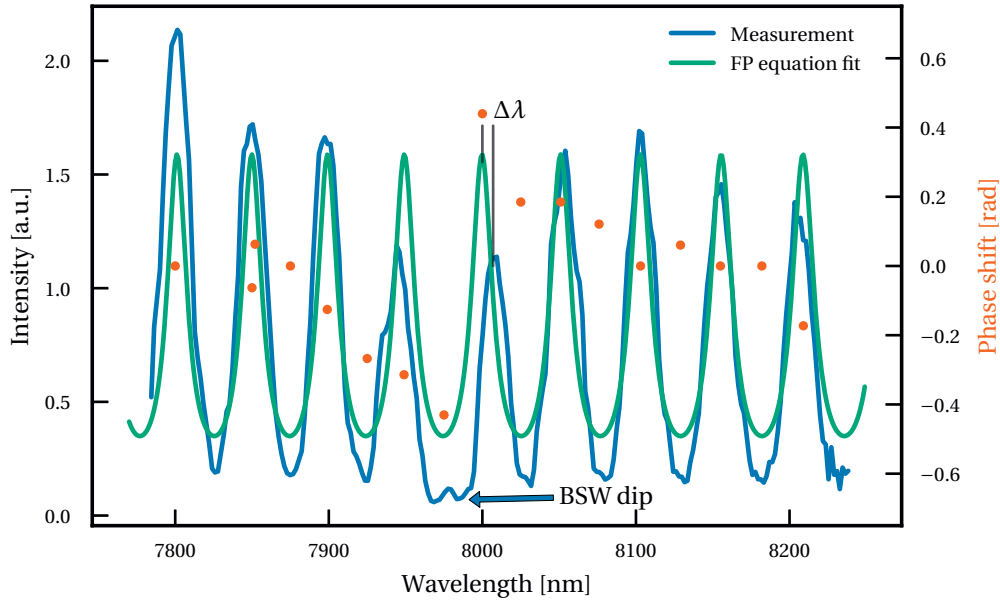
Figure 4.15 – Measured intensity of the center of the spot reflected by the prism with the multi-layer structure on top (blue curve). The incident angle on the prism is 70°. The BSW coupling dip can be observed at 7985 nm wavelength. The orange curve shows the fit of equation 4.1. The intensity maxima and minima are shifted in the vicinity of the BSW dip. The orange dots represent the phase difference between the FP fit and the measurement. The phase is determined from the wavelength shift $\Delta\lambda$ with respect to the FP curve period.

4.5 Outlook

Further developments of the platform are ongoing. A five-pair multi-layer design has been fabricated. The multi-layer is also deposited on a CaF_2 substrate. It consists of five pairs of ZnSe and YbF_3 of 0.967 µm and 1.578 µm thickness, respectively. A ZnSe defect layer of 242 nm is deposited on top of the periodic stack. Figure 4.16 shows the simulated mode profile of the five pairs structure for different incident angles inside the substrate. A higher number of pairs increases the confinement of the Bloch surface wave at the interface, which consequently reduces leakage and allows for higher propagation length.

The measurement of the propagation length of the BSW is of interest. In the NIR, the surface wave propagation has been observed by scanning near-field optical microscopy (SNOM)[106]. Since we do not have access to MIR SNOM, we propose instead to pattern a grating on top of the multi-layer surface, to out-couple part of the surface wave and observe it, as described in figure 4.17 and previously demonstrated in the visible[107, 108, 109].

Previous uses of BSW platforms for sensing applications used the angular shift of the reflection dip. The refractive index at the surface of the multi-layer changes locally with the aggregation of proteins on the surface[12, 110]. This localized refractive index changes shifts the BSW coupling condition. While very sensitive, this measurement is however not specific. The combination of a tunable MIR laser and the BSW platform could allow to make direct spectroscopic surface measurements.
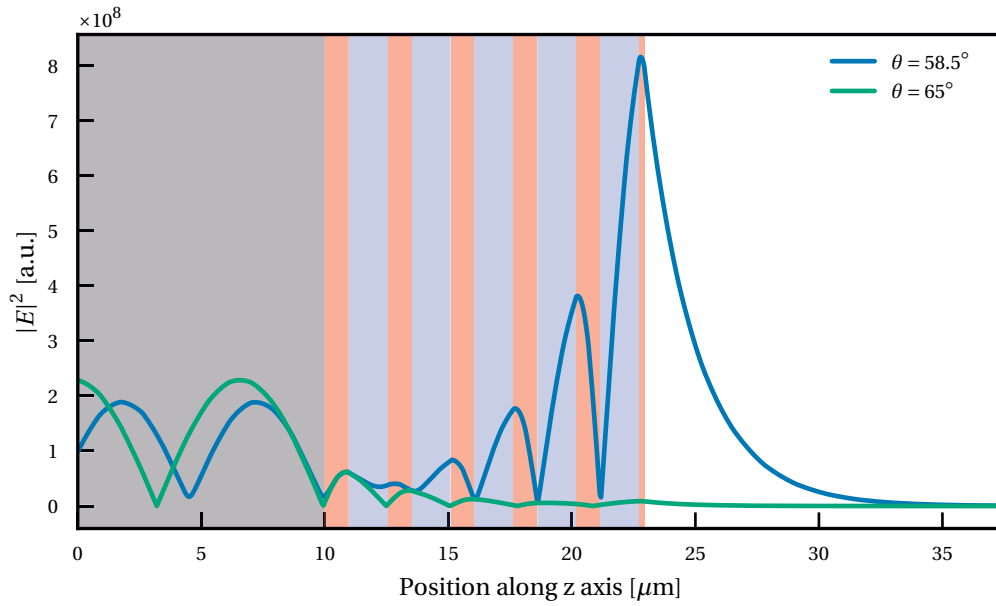
Figure 4.16 – Simulated intensity of the electric field along the axis normal to the surface of the multi-layer stack at 7.8 µm wavelength in TE polarization. The gray area represents the CaF_2 substrate. The red and blue areas represent the ZnSe and YbF_3 layers, respectively. The blue curve shows the electric field profile at an incident angle of 58.5°. The green curve shows the electric field profile at an incident angle of 65°.
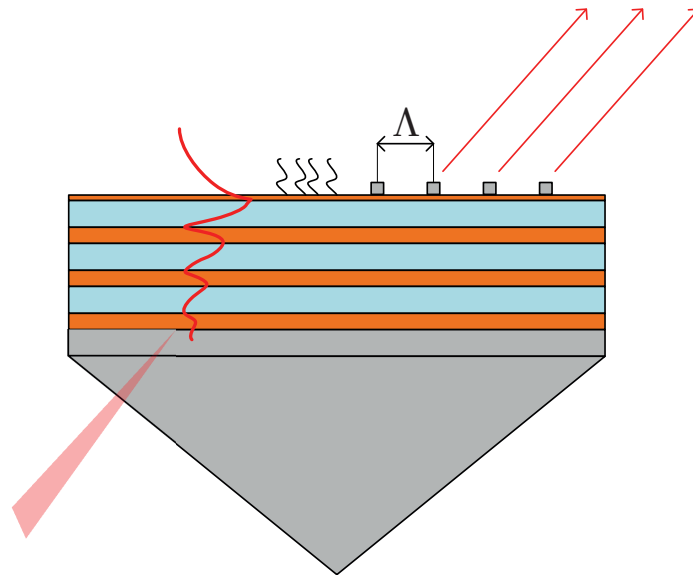
Figure 4.17 – Surface sensing scheme of an analye on the surface of the multi-layer stack. A grating of period Λ is deposited on top of the multi-layer to out-couple the surface wave after its propagation through the analyte.

4.6 Conclusion

This chapter presented the first design and characterization of dielectric multi-layer structure supporting BSWs in the MIR spectrum. The structure is made of a periodic arrangement of ZnSe and YbF$_3$ layers on top of a CaF$_2$ substrate. A complete simulation of the multi-layer structure reflectivity dispersion around 7.8 µm has been performed. A characterization of the dispersion of the BSW mode on the multi-layer was described.

A BSW platform can replace SPP sensors[98], with increased flexibility over the operating wavelength and specificity. The main advantage of the multi-layer design is its scalability and adaptability to work from visible to MIR wavelengths, as long as the materials used are transparent. The presented platform offers great potential for near-field spectroscopy in the MIR.

Conclusion

The work presented in this thesis has focused the realization of on optical elements for the mid-infrared spectral range. A complete external cavity tunable quantum cascade laser setup has been assembled. This setup has been used for the characterization two kinds of passive optical elements. The first type of elements is based on sub-wavelength features on high-index materials. These features allow to exhibit diffractive and anti-reflective properties simultaneously. The second type of elements is a multi-layer structure allowing the propagation of a Bloch surface wave at its interface with a surrounding medium. In addition, a quantum cascade laser–based cocaine sensing setup has been presented, emphasizing the interest of these light sources for compact sensing setups.

The first part of the thesis introduced the quantum cascade laser and its applications in spectroscopy. The realization of an external cavity tunable quantum cascade laser setup has been presented. The tunable range of the laser is $105\,\mathrm{cm}^{-1}$ around $7.8\,\mu\mathrm{m}$. The wavelength can be selected in steps of $0.039\,\mathrm{cm}^{-1}$. These performances are comparable with commercially available tunable lasers. This laser source has been mainly used for the characterization of passive optical components. The feasibility of a direct absorption optical sensor for the detection of cocaine in liquid phase using a quantum cascade laser has been presented. A detection limit of $1.35\,\mu\mathrm{g/ml}$ of cocaine in tetrachloroethylene has been reached. The current setup provides an improvement of two order of magnitude of the detection limit compared to the previous record with a similar laser source. The results are comparable to Fourier transform spectroscopy–based detection experiments with the advantage of a compact and transportable setup.

In a second part, a class of sub-wavelength structured surfaces on high-index materials such as silicon for the realization of passive optical elements in the mid-infrared have been presented. A general rule governing the thickness of the sub-wavelength elements has been proposed. Following this method, diffractive optical elements with an anti-reflective function can be fabricated in one single lithographic step. Such structures can be used for many applications such as beam splitters or polarizers and pave the way for cost–efficient and application–specific mid-infrared optical elements.

As an example of a potential application, the design of a low reflectivity binary diffractive optical element using the aforementioned method has been presented. This method is

particularly interesting for optical elements made of high refractive index materials such as zinc selenide, silicon or germanium, as it allows to use these materials without an additional anti-reflective coating. The performance of the proposed gratings have been analyzed with respect to design parameters such as grating depth and period. The fabrication steps of a silicon Dammann grating – a specific beam splitter design – operating around $7.85\,\mu m$ have been presented. The fabricated element has been characterized and exhibits $18\,\%$ more light transmission than a similar silicon wafer without patterning in addition of providing a diffractive optical function. Such elements could be used for the realization of specific mid-infrared illumination patterns or providing reference measurements for sensing applications.

In the final part, the design and characterization of a dielectric multi-layer structure supporting Bloch surface waves in the range of $7.6\,\mu m$ to $8.1\,\mu m$ has been presented. It is the first time that such surface waves have been observed in the mid-infrared spectrum. The characterization of the dispersion of the Bloch surface wave mode on the fabricated multi-layer surface has been performed using the tunable laser setup previously developed. The structure design is based on a periodic arrangement of ZnSe and YbF$_3$ layers deposited on a CaF$_2$ substrate. A complete simulation of the multi-layer structure reflectivity dispersion has been performed. The presented platform offers great potential for surface spectroscopy in the mid-infrared. The main advantage of the multi-layer design is its scalability and adaptability to work from visible to mid-infrared wavelengths, as long as the materials used are transparent.

Outlook

The sub-wavelength diffractive elements described in this thesis can be extended to two-dimensional patterns, allowing the realization of complex illumination patterns. Such elements could be used for example in mid-infrared microscopy setups. Birefringent structures such as half-wave plates could also be realized with the proposed fabrication method. Any binary two-level diffractive optical design can be realized with this approach. This is an important step to reduce the scarcity of mid-infrared optical components. Further developments of the fabrication process could lead to better transmission efficiencies and improved accuracy of the diffraction patterns.

The proposed Bloch surface wave platform could replace surface plasmon polaritons–based sensors, with increased flexibility over the operating wavelength and specificity. It should also provide in theory a longer interaction length with the sample. Multi-layer structures made of Si, Ge or ZnSe could be used for operation at longer wavelengths or to probe media of high refractive index such as water. Further developments of the platform such as the addition of surface patterning should be investigated. Structures such as gratings can be used to out-couple the surface wave, allowing to precisely characterize its propagation length. A Bloch surface wave–based platform is a promising building block for high sensitivity mid-infrared surface spectroscopy.

A Process parameters

Tables A.1, A.2 and A.3 describe the process recipes used on the STS Multiplex ICP RIE machine for etching, surface cleaning and resist descumming, respectively.

Table A.1 – Process parameters of the STS Multiplex ICP RIE for the etching of 600 nm wide trenches in silicon with a Cr mask. This process is repeated four times with a 5 min pause between successive runs and provides an etch depth of approximately 1 µm per run.

Process parameter	Value
Pressure	21 mtorr
ICP RF power	600 W
Platen RF power	45 W
Platen temperature	10 °C
SF_6 flow	6 sccm
C_3F_8 flow	34.5 sccm
Process time	565 s

Table A.2 – Process parameters for the STS Multiplex ICP RIE for the cleaning of the passivation layer deposited during the etching of silicon.

Process parameter	Value
Pressure	25 mtorr
ICP RF power	800 W
Platen RF power	25 W
Platen temperature	10 °C
O_2 flow	40 sccm
Process time	90 s

Table A.3 – Process parameters for the STS Multiplex ICP RIE for the removal e-beam resist (descumming).

Process parameter	Value
Pressure	25 mtorr
ICP RF power	0 W
Platen RF power	50 W
Platen temperature	10 °C
O_2 flow	20 sccm
Process time	35 s

Bibliography

[1] Jane Hodgkinson and Ralph P. Tatam. Optical gas sensing: a review. *Measurement Science and Technology*, 24(1):012004, 2013.

[2] Ilya Dunayevskiy, Alexei Tsekoun, Manu Prasanna, Rowel Go, and C. Kumar N. Patel. High-sensitivity detection of triacetone triperoxide (TATP) and its precursor acetone. *Applied Optics*, 46(25):6397–6404, September 2007.

[3] Pierre Jouy, Markus Mangold, Béla Tuzson, Lukas Emmenegger, Yu-Chi Chang, Lubos Hvozdara, Hans Peter Herzig, Philip Wägli, Alexandra Homsy, Nico F. de Rooij, Alexander Wirthmueller, Daniel Hofstetter, Herbert Looser, and Jérôme Faist. Mid-infrared spectroscopy for gases and liquids based on quantum cascade technologies. *Analyst*, 139(9):2039–2046, April 2014.

[4] Jerome Faist, Federico Capasso, Deborah L. Sivco, Carlo Sirtori, Albert L. Hutchinson, and Alfred Y. Cho. Quantum Cascade Laser. *Science*, 264(5158):553–556, April 1994.

[5] Andreas Schwaighofer, Markus Brandstetter, and Bernhard Lendl. Quantum cascade lasers (QCLs) in biomedical spectroscopy. *Chemical Society Reviews*, 46(19):5903–5924, 2017.

[6] Gustavo Villares, Andreas Hugi, Stéphane Blaser, and Jérôme Faist. Dual-comb spectroscopy based on quantum-cascade-laser frequency combs. *Nature Communications*, 5:5192, October 2014.

[7] H. P. Herzig, D. Prongué, and R. Dändliker. Design and Fabrication of Highly Efficient Fan-Out Elements. *Japanese Journal of Applied Physics*, 29(Part 2, No. 7):L1307–L1309, July 1990.

[8] Nanfang Yu and Federico Capasso. Flat optics with designer metasurfaces. *Nature Materials*, 13(2):139–150, February 2014.

[9] Yu-Chi Chang, Philip Wägli, Vincent Paeder, Alexandra Homsy, Lubos Hvozdara, Peter van der Wal, Joab Di Francesco, Nico F. de Rooij, and Hans Peter Herzig. Cocaine detection by a mid-infrared waveguide integrated with a microfluidic chip. *Lab on a Chip*, 12(17):3020–3023, 2012.

[10] Daniel Rodrigo, Odeta Limaj, Davide Janner, Dordaneh Etezadi, F. Javier García de Abajo, Valerio Pruneri, and Hatice Altug. Mid-infrared plasmonic biosensing with graphene. *Science*, 349(6244):165–168, July 2015.

[11] John D. Joannopoulos, Steven G. Johnson, Joshua N. Winn, and Robert D. Meade. *Photonic Crystals: Molding the Flow of Light (Second Edition)*. Princeton University Press, October 2011. Google-Books-ID: QrTNslcjlZEC.

[12] Sara Santi, Valeria Musi, Emiliano Descrovi, Vincent Paeder, Joab Di Francesco, Lubos Hvozdara, Peter van der Wal, Hilal A. Lashuel, Annalisa Pastore, Reinhard Neier, and Hans Peter Herzig. Real-time Amyloid Aggregation Monitoring with a Photonic Crystal-based Approach. *ChemPhysChem*, 14(15):3476–3482, October 2013.

[13] Richard Maulini. *Broadly tunable mid-infrared quantum cascade lasers for spectroscopic applications*. PhD thesis, Université de Neuchâtel, 2006.

[14] Jérôme Faist, Federico Capasso, Deborah L. Sivco, Albert L. Hutchinson, Sung-Nee G. Chu, and Alfred Y. Cho. Short wavelength (3.4m) quantum cascade laser based on strained compensated InGaAs/AlInAs. *Applied Physics Letters*, 72(6):680–682, February 1998.

[15] Raffaele Colombelli, Federico Capasso, Claire Gmachl, Albert L. Hutchinson, Deborah L. Sivco, Alessandro Tredicucci, Michael C. Wanke, A. Michael Sergent, and Alfred Y. Cho. Far-infrared surface-plasmon quantum-cascade lasers at 21.5 m and 24 m wavelengths. *Applied Physics Letters*, 78(18):2620–2622, April 2001.

[16] Sushil Kumar, Chun Wang I. Chan, Qing Hu, and John L. Reno. A 1.8-THz quantum cascade laser operating significantly above the temperature of /kB. *Nature Physics*, 7(2):166–171, February 2011.

[17] Jérome Faist, Claire Gmachl, Federico Capasso, Carlo Sirtori, Deborah L. Sivco, James N. Baillargeon, and Alfred Y. Cho. Distributed feedback quantum cascade lasers. *Applied Physics Letters*, 70(20):2670–2672, May 1997.

[18] L Hvozdara, N Pennington, M Kraft, M Karlowatz, and B Mizaikoff. Quantum cascade lasers for mid-infrared spectroscopy. *Vibrational Spectroscopy*, 30(1):53–58, September 2002.

[19] L. Tombez, S. Schilt, J. Di Francesco, T. Führer, B. Rein, T. Walther, G. Di Domenico, D. Hofstetter, and P. Thomann. Linewidth of a quantum-cascade laser assessed from its frequency noise spectrum and impact of the current driver. *Applied Physics B*, 109(3):407–414, November 2012.

[20] L. Tombez, S. Schilt, D. Hofstetter, and T. Südmeyer. Active linewidth-narrowing of a mid-infrared quantum cascade laser without optical reference. *Optics Letters*, 38(23):5079–5082, December 2013.

[21] Andrea Edelmann, Caterina Ruzicka, Johannes Frank, Bernhard Lendl, Werner Schrenk, Erich Gornik, and Gottfried Strasser. Towards functional group-specific detection in high-performance liquid chromatography using mid-infrared quantum cascade lasers. *Journal of Chromatography A*, 934(1–2):123–128, November 2001.

[22] Mattias Beck, Daniel Hofstetter, Thierry Aellen, Jérôme Faist, Ursula Oesterle, Marc Ilegems, Emilio Gini, and Hans Melchior. Continuous Wave Operation of a Mid-Infrared Semiconductor Laser at Room Temperature. *Science*, December 2001.

[23] Gail Cooper, Lisa Wilson, Claire Reid, Dene Baldwin, Chris Hand, and Vina Spieher. Validation of the Cozart microplate EIA for cocaine and metabolites in oral fluid. *Journal of Analytical Toxicology*, 28(6):498–503, September 2004.

[24] N. Samyn and C. van Haeren. On-site testing of saliva and sweat with Drugwipe and determination of concentrations of drugs of abuse in saliva, plasma and urine of suspected users. *International Journal of Legal Medicine*, 113(3):150–154, May 2000.

[25] Wen-Ling Wang, William D. Darwin, and Edward J. Cone. Simultaneous assay of cocaine, heroin and metabolites in hair, plasma, saliva and urine by gas chromatography—mass spectrometry. *Journal of Chromatography B: Biomedical Sciences and Applications*, 660(2):279–290, October 1994.

[26] Kerstin M.-C. Hans, Matthias Müller, Tigran Petrosyan, and Markus W. Sigrist. Infrared detection of cocaine and street cocaine in saliva with a one-step extraction. *Analytical Methods*, 6(3):666, 2014.

[27] Philip Wägli, Yu-Chi Chang, Alexandra Homsy, Lubos Hvozdara, Hans Peter Herzig, and Nico F. de Rooij. Microfluidic Droplet-Based Liquid–Liquid Extraction and On-Chip IR Spectroscopy Detection of Cocaine in Human Saliva. *Analytical Chemistry*, 85(15):7558–7565, August 2013.

[28] Yu-Chi Chang, Vincent Paeder, Lubos Hvozdara, Jean-Michel Hartmann, and Hans Peter Herzig. Low-loss germanium strip waveguides on silicon for the mid-infrared. *Optics Letters*, 37(14):2883–2885, July 2012.

[29] Kerstin M.-C. Hans, Susanne Müller, and Markus W. Sigrist. Infrared attenuated total reflection (IR-ATR) spectroscopy for detecting drugs in human saliva: Infrared attenuated total reflection (IR-ATR) spectroscopy for detecting drugs in duman saliva. *Drug Testing and Analysis*, 4(6):420–429, June 2012.

[30] Grégoire M. Smolik, Lubos Hvozdara, Joab Di Francesco, Pierre Jouy, Yargo Bonetti, Kerstin Hans, Markus W. Sigrist, Jérôme Faist, and Hans Peter Herzig. Cocaine detection in liquid using a fibered platform and a mid-infrared quantum cascade laser. In *Advanced Photonics (2014), paper SeTh1C.2*, page SeTh1C.2. Optical Society of America, July 2014.

[31] Beer–Lambert law (or Beer–Lambert–Bouguer law). In Miloslav Nič, Jiří Jirát, Bedřich Košata, Aubrey Jenkins, and Alan McNaught, editors, *IUPAC Compendium of Chemical Terminology*. IUPAC, Research Triangle Park, NC, 2.1.0 edition, June 2009.

[32] Kerstin M.-C. Hans, Matthias Müller, Tigran Petrosyan, and Markus W. Sigrist. Infrared detection of cocaine and street cocaine in saliva with a one-step extraction. *Analytical Methods*, 2013.

[33] C. Marxer and N. F. de Rooij. Micro-opto-mechanical 2 times;2 switch for single-mode fibers based on plasma-etched silicon mirror and electrostatic actuation. *Journal of Lightwave Technology*, 17(1):2–6, January 1999.

[34] J. Jágerská, P. Jouy, A. Hugi, B. Tuzson, H. Looser, M. Mangold, M. Beck, L. Emmenegger, and J. Faist. Dual-wavelength quantum cascade laser for trace gas spectroscopy. *Applied Physics Letters*, 105(16):161109, October 2014.

[35] G. P. Luo, C. Peng, H. Q. Le, S. S. Pei, W.-Y. Hwang, B. Ishaug, J. Um, James N. Baillargeon, and C.-H. Lin. Grating-tuned external-cavity quantum-cascade semiconductor lasers. *Applied Physics Letters*, 78(19):2834–2836, May 2001.

[36] Richard Maulini, Mattias Beck, and Jérôme Faist. Broadband tuning of external cavity bound-to-continuum quantum-cascade lasers. *Applied Physics Letters*, 84(10):1659–1661, March 2004.

[37] R Centeno, D. Marchenko, J. Mandon, S. M. Cristescu, G. Wulterkens, and F. J. M. Harren. High power, widely tunable, mode-hop free, continuous wave external cavity quantum cascade laser for multi-species trace gas detection. *Applied Physics Letters*, 105(26):261907, December 2014.

[38] M. G. Moharam and T. K. Gaylord. Rigorous coupled-wave analysis of planar-grating diffraction. *Journal of the Optical Society of America*, 71(7):811–818, July 1981.

[39] M. G. Moharam, T. K. Gaylord, Eric B. Grann, and Drew A. Pommet. Formulation for stable and efficient implementation of the rigorous coupled-wave analysis of binary gratings. *JOSA A*, 12(5):1068–1076, May 1995.

[40] M. G. Moharam, T. K. Gaylord, Drew A. Pommet, and Eric B. Grann. Stable implementation of the rigorous coupled-wave analysis for surface-relief gratings: enhanced transmittance matrix approach. *JOSA A*, 12(5):1077–1086, May 1995.

[41] Lifeng Li. Use of Fourier series in the analysis of discontinuous periodic structures. *JOSA A*, 13(9):1870–1876, September 1996.

[42] Nikolay M. Lyndin, Olivier Parriaux, and Alexander V. Tishchenko. Modal analysis and suppression of the Fourier modal method instabilities in highly conductive gratings. *JOSA A*, 24(12):3781–3788, December 2007.

[43] G. Wysocki, R. F. Curl, F. K. Tittel, R. Maulini, J. M. Bulliard, and J. Faist. Widely tunable mode-hop free external cavity quantum cascade laser for high resolution spectroscopic applications. *Applied Physics B-Lasers and Optics*, 81(6):769–777, October 2005. WOS:000232792500006.

[44] Eugene Hecht. *Optics*. 2017. OCLC: 953709783.

[45] Raymond C. Rumpf. Improved Formulation of Scattering Matrices for Semi-Analytical Methods That Is Consistent with Convention. *Progress In Electromagnetics Research B*, 35:241–261, 2011.

[46] Pochi Yeh. *Optical Waves in Layered Media*. Wiley, March 2005.

[47] D. Y. K. Ko and J. R. Sambles. Scattering matrix method for propagation of radiation in stratified media: attenuated total reflection studies of liquid crystals. *JOSA A*, 5(11):1863–1866, November 1988.

[48] M. G. Moharam and T. K. Gaylord. Diffraction analysis of dielectric surface-relief gratings. *JOSA*, 72(10):1385–1392, October 1982.

[49] Herzig. Micro-Optics: Elements, Systems And Applications, April 1997.

[50] Albertas Žukauskas, Ieva Matulaitienė, Domas Paipulas, Gediminas Niaura, Mangirdas Malinauskas, and Roaldas Gadonas. Tuning the refractive index in 3d direct laser writing lithography: towards GRIN microoptics. *Laser & Photonics Reviews*, 9(6):706–712, November 2015.

[51] Jeeva Anandan. The geometric phase. *Nature*, 360(6402):307–313, November 1992.

[52] Rajendra Bhandari. Polarization of light and topological phases. *Physics Reports*, 281(1):1–64, March 1997.

[53] Ze'ev Bomzon, Gabriel Biener, Vladimir Kleiner, and Erez Hasman. Space-variant Pancharatnam–Berry phase optical elements with computer-generated subwavelength gratings. *Optics Letters*, 27(13):1141, July 2002.

[54] Robert W. Batterman. Falling cats, parallel parking, and polarized light. *Studies in History and Philosophy of Science Part B: Studies in History and Philosophy of Modern Physics*, 34(4):527–557, December 2003.

[55] Erez Hasman, Ze'ev Bomzon, Avi Niv, Gabriel Biener, and Vladimir Kleiner. Polarization beam-splitters and optical switches based on space-variant computer-generated subwavelength quasi-periodic structures. *Optics Communications*, 209(1–3):45–54, August 2002.

[56] Stéphane Larouche, Yu-Ju Tsai, Talmage Tyler, Nan M. Jokerst, and David R. Smith. Infrared metamaterial phase holograms. *Nature Materials*, 11(5):450–454, May 2012.

[57] Chulwoo Oh and Michael J. Escuti. Achromatic diffraction from polarization gratings with high efficiency. *Optics Letters*, 33(20):2287–2289, October 2008.

[58] Nanfang Yu, Patrice Genevet, Mikhail A. Kats, Francesco Aieta, Jean-Philippe Tetienne, Federico Capasso, and Zeno Gaburro. Light Propagation with Phase Discontinuities: Generalized Laws of Reflection and Refraction. *Science*, 334(6054):333–337, October 2011.

[59] Guoxing Zheng, Holger Mühlenbernd, Mitchell Kenney, Guixin Li, Thomas Zentgraf, and Shuang Zhang. Metasurface holograms reaching 80% efficiency. *Nature Nano-technology*, advance online publication, February 2015.

[60] Jihwan Kim, Yanming Li, Matthew N. Miskiewicz, Chulwoo Oh, Michael W. Kudenov, and Michael J. Escuti. Fabrication of ideal geometric-phase holograms with arbitrary wavefronts. *Optica*, 2(11):958–964, November 2015.

[61] Arseniy I. Kuznetsov, Andrey E. Miroshnichenko, Yuan Hsing Fu, JingBo Zhang, and Boris Luk'yanchuk. Magnetic light. *Scientific Reports*, 2:492, July 2012.

[62] Andrey B. Evlyukhin, Sergey M. Novikov, Urs Zywietz, René Lynge Eriksen, Carsten Reinhardt, Sergey I. Bozhevolnyi, and Boris N. Chichkov. Demonstration of Magnetic Dipole Resonances of Dielectric Nanospheres in the Visible Region. *Nano Letters*, 12(7):3749–3755, July 2012.

[63] P. Spinelli, M. A. Verschuuren, and A. Polman. Broadband omnidirectional antire-flection coating based on subwavelength surface Mie resonators. *Nature Communicati-ons*, 3:692, February 2012.

[64] Isabelle Staude, Andrey E. Miroshnichenko, Manuel Decker, Nche T. Fofang, Sheng Liu, Edward Gonzales, Jason Dominguez, Ting Shan Luk, Dragomir N. Neshev, Igal Brener, and Yuri Kivshar. Tailoring Directional Scattering through Magnetic and Electric Resonances in Subwavelength Silicon Nanodisks. *ACS Nano*, 7(9):7824–7832, September 2013.

[65] Manuel Decker, Isabelle Staude, Matthias Falkner, Jason Dominguez, Dragomir N. Neshev, Igal Brener, Thomas Pertsch, and Yuri S. Kivshar. High-Efficiency Dielectric Huygens' Surfaces. *Advanced Optical Materials*, 3(6):813–820, June 2015.

[66] Katie E. Chong, Lei Wang, Isabelle Staude, Anthony R. James, Jason Dominguez, Sheng Liu, Ganapathi S. Subramania, Manuel Decker, Dragomir N. Neshev, Igal Brener, and Yuri S. Kivshar. Efficient Polarization-Insensitive Complex Wavefront Control Using Huygens' Metasurfaces Based on Dielectric Resonant Meta-atoms. *ACS Photonics*, 3(4):514–519, April 2016.

[67] Denis G. Baranov, Dmitry A. Zuev, Sergey I. Lepeshov, Oleg V. Kotov, Alexander E. Krasnok, Andrey B. Evlyukhin, and Boris N. Chichkov. All-dielectric nanophotonics: the quest for better materials and fabrication techniques. *Optica*, 4(7):814–825, July 2017.

[68] Amir Arbabi, Ryan M. Briggs, Yu Horie, Mahmood Bagheri, and Andrei Faraon. Efficient dielectric metasurface collimating lenses for mid-infrared quantum cascade lasers. *Optics Express*, 23(26):33310–33317, December 2015.

[69] Eric Logean, Lubos Hvozdara, Joab Di-Francesco, Hans Peter Herzig, Reinhard Voelkel, Martin Eisner, Pierre-Yves Baroni, Michel Rochat, and Antoine Müller. High numerical aperture silicon collimating lens for mid-infrared quantum cascade lasers manufactured using wafer-level techniques. volume 8550, pages 85500Q–85500Q–6, 2012.

[70] Thomas K. Gaylord, W. E. Baird, and M. G. Moharam. Zero-reflectivity high spatial-frequency rectangular-groove dielectric surface-relief gratings. *Applied Optics*, 25(24):4562–4567, December 1986.

[71] Philippe Lalanne and Dominique Lemercier-lalanne. On the effective medium theory of subwavelength periodic structures. *Journal of Modern Optics*, 43(10):2063–2085, October 1996.

[72] Philippe Lalanne and Dominique Lemercier-Lalanne. Depth dependence of the effective properties of subwavelength gratings. *Journal of the Optical Society of America A*, 14(2):450, February 1997.

[73] Deane Chandler-Horowitz and Paul M. Amirtharaj. High-accuracy, midinfrared refractive index values of silicon. *Journal of Applied Physics*, 97(12):123526, June 2005.

[74] Pochi Yeh. A new optical model for wire grid polarizers. *Optics Communications*, 26(3):289–292, September 1978.

[75] Lucila H. Cescato, Ekkehart Gluch, and Norbert Streibl. Holographic quarterwave plates. *Applied Optics*, 29(22):3286–3290, August 1990.

[76] Dale C. Flanders. Submicrometer periodicity gratings as artificial anisotropic dielectrics. *Applied Physics Letters*, 42(6):492–494, March 1983.

[77] W. Stork, N. Streibl, H. Haidner, and P. Kipfer. Artificial distributed-index media fabricated by zero-order gratings. *Optics Letters*, 16(24):1921–1923, December 1991.

[78] Michael W. Farn. Binary gratings with increased efficiency. *Applied Optics*, 31(22):4453–4458, August 1992.

[79] F. T. Chen and H. G. Craighead. Diffractive phase elements based on two-dimensional artificial dielectrics. *Optics Letters*, 20(2):121–123, January 1995.

[80] Philippe Lalanne, Simion Astilean, Pierre Chavel, Edmond Cambril, and Huguette Launois. Blazed binary subwavelength gratings with efficiencies larger than those of conventional échelette gratings. *Optics Letters*, 23(14):1081, July 1998.

[81] Philippe Lalanne and G. Michael Morris. Antireflection behavior of silicon subwavelength periodic structures for visible light. *Nanotechnology*, 8(2):53, 1997.

[82] Alexei Deinega, Ilya Valuev, Boris Potapkin, and Yurii Lozovik. Minimizing light reflection from dielectric textured surfaces. *Journal of the Optical Society of America A*, 28(5):770, May 2011.

[83] Eric B. Grann, M. G. Moharam, and Drew A. Pommet. Artificial uniaxial and biaxial dielectrics with use of two-dimensional subwavelength binary gratings. *Journal of the Optical Society of America A*, 11(10):2695, October 1994.

[84] Gregory Nordin and Panfilo Deguzman. Broadband form birefringent quarter-wave plate for the mid-infrared wavelength region. *Optics Express*, 5(8):163, October 1999.

[85] Gary J. Swanson. Binary Optics Technology: Theoretical Limits on the Diffraction Efficiency of Multilevel Diffractive Optical Elements. Technical report, 1991.

[86] G. Smolik and H. P. Herzig. Binary subwavelength structures that act simultaneously as antireflective and diffractive structure for the mid-infrared wavelength range. 2016.

[87] Grégoire M. Smolik and Hans Peter Herzig. Binary zero-order diffractive and antireflective optical elements in silicon for the mid-infrared. *Optics Letters*, 42(16):3233–3235, August 2017.

[88] H. Dammann and K. Görtler. High-efficiency in-line multiple imaging by means of multiple phase holograms. *Optics Communications*, 3(5):312–315, July 1971.

[89] H. Dammann and E. Klotz. Coherent Optical Generation and Inspection of Two-dimensional Periodic Structures. *Optica Acta: International Journal of Optics*, 24(4):505–515, April 1977.

[90] U. Krackhardt and N. Streibl. Design of dammann-gratings for array generation. *Optics Communications*, 74(1):31–36, December 1989.

[91] Drew A. Pommet, M. G. Moharam, and Eric B. Grann. Limits of scalar diffraction theory for diffractive phase elements. *Journal of the Optical Society of America A*, 11(6):1827, June 1994.

[92] Gaël David Osowiecki. *Excitation of resonant plasmonic cavities by integrated waveguides for sensing applications.* PhD thesis, École Polytechnique Fédérale de Lausanne, 2016.

[93] Franz Laermer and Andrea Schilp. Method of anisotropically etching silicon, March 1996.

[94] Mohamed Tarek Ghoneim and Muhammad Mustafa Hussain. Highly Manufacturable Deep (Sub-Millimeter) Etching Enabled High Aspect Ratio Complex Geometry Lego-Like Silicon Electronics. *Small*, January 2017.

[95] Michael David Henry. *ICP etching of silicon for micro and nanoscale devices.* PhD thesis, California Institute of Technology, 2010.

[96] Pochi Yeh, Amnon Yariv, and Alfred Y. Cho. Optical surface waves in periodic layered media. *Applied Physics Letters*, 32(2):104–105, January 1978.

[97] W. M. Robertson and M. S. May. Surface electromagnetic wave excitation on one-dimensional photonic band-gap arrays. *Applied Physics Letters*, 74(13):1800–1802, March 1999.

[98] M. Shinn and W. M. Robertson. Surface plasmon-like sensor based on surface electro-magnetic waves in a photonic band-gap material. *Sensors and Actuators B: Chemical*, 105(2):360–364, March 2005.

[99] W. M. Robertson. Experimental measurement of the effect of termination on surface electromagnetic waves in one-dimensional photonic bandgap arrays. *Journal of Light-wave Technology*, 17(11):2013–2017, November 1999.

[100] R. Dubey, E. Barakat, and H. P. Herzig. Bloch surface waves based platform for integrated optics. In *2015 IEEE Photonics Conference (IPC)*, pages 200–201, October 2015.

[101] Pochi Yeh, Amnon Yariv, and Chi-Shain Hong. Electromagnetic propagation in periodic stratified media. I. General theory. *JOSA*, 67(4):423–438, April 1977.

[102] Robert D. Meade, Karl D. Brommer, Andrew M. Rappe, and J. D. Joannopoulos. Electromagnetic Bloch waves at the surface of a photonic crystal. *Physical Review B*, 44(19):10961–10964, November 1991.

[103] Erwin Kretschmann. Die Bestimmung optischer Konstanten von Metallen durch Anregung von Oberflächenplasmaschwingungen. *Zeitschrift für Physik A Hadrons and nuclei*, 241(4):313–324, August 1971.

[104] Vincent Paeder. *Bloch Surface Wave Biosensing: Study of Optical Elements for the Early Detection of Protein Aggregation*. PhD thesis, École Polytechnique Fédérale de Lausanne, 2011.

[105] Bahaa E. A. Saleh and Malvin Carl Teich. *Fundamentals of Photonics*. Wiley, March 2007. Google-Books-ID: Ve8eAQAAIAAJ.

[106] Emiliano Descrovi, Tristan Sfez, Lorenzo Dominici, Wataru Nakagawa, Francesco Michelotti, Fabrizio Giorgis, and Hans-Peter Herzig. Near-field imaging of Bloch surface waves on silicon nitride one-dimensional photonic crystals. *Optics Express*, 16(8):5453–5464, April 2008.

[107] A. Angelini, E. Enrico, N. De Leo, P. Munzert, L. Boarino, F. Michelotti, F. Giorgis, and E. Descrovi. Fluorescence diffraction assisted by Bloch surface waves on a one-dimensional photonic crystal. *New Journal of Physics*, 15(7):073002, 2013.

[108] Emiliano Descrovi, Elsie Barakat, Angelo Angelini, Peter Munzert, Natascia De Leo, Luca Boarino, Fabrizio Giorgis, and Hans Peter Herzig. Leakage radiation interference microscopy. *Optics Letters*, 38(17):3374–3376, September 2013.

[109] Angelo Angelini, Elsie Barakat, Peter Munzert, Luca Boarino, Natascia De Leo, Emanuele Enrico, Fabrizio Giorgis, Hans Peter Herzig, Candido Fabrizio Pirri, and Emiliano Descrovi. Focusing and Extraction of Light mediated by Bloch Surface Waves. *Scientific Reports*, 4:5428, June 2014.

[110] Sara Santi. *A novel nano-optical sensing approach for real-time amyloid aggregation monitoring*. PhD thesis, Université de Neuchâtel, 2016.

Remerciements

Grégoire Smolik

Curriculum Vitae

Rte de Buchillon 10
1162 St-Prex
Switzerland
☏ +41 76 476 8423
✉ gregoire.smolik@gmail.com
🔗 gsmolik

Education

2013–2017	**PhD Thesis**, EPFL, Neuchâtel, Mid-infrared optics.
2010–2012	**Master of Science MSc**, EPFL, Lausanne, Microengineering.
	Applied Optics specialization, Minor in Space Technology
2007–2010	**Bachelor of Science BSc**, EPFL, Lausanne, Microengineering.

Experience

2013–2017	**PhD Student**, OPT *Lab,* EPFL, Neuchâtel, Switzerland.

Research on optical materials and microstructures for mid-infrared applications

- Design, realization and characterization of an external cavity tunable QCL setup
- Development and fabrication of low reflectivity MIR diffractive optics on silicon
- Management, maintenance of lab equipment
- Mid-infrared spectroscopy
  - FTIR
  - Liquid-phase laser spectroscopy
- Micronano-fabrication techniques
  - E-beam lithography
  - E-beam physical vapor deposition
  - PE-CVD
  - Reactive ion etching
  - Scanning electron microscopy

2012	**Visiting Grad Student**, UCSD, San Diego, USA.

Master Thesis abroad

- Electronics, optics, ray-tracing

Master thesis

Title	*Blink detection system for hands-free zoom*
Supervisors	Professor Joseph E. Ford, UC San Diego, California & Professor Christophe Moser, EPFL, Switzerland
Description	This thesis investigated the implementation of a blink detector integrated in a contact lens with zooming capabilities

Languages

French	Mother tongue
English	Fluent
German	Intermediate - B2 level

Computer skills

Programming	C, Python, Matlab	Other	LabView, ImageJ, Linux
CAD	Solidworks, Pro/ENGINEER		
Optics	CST Microwave Studio, RCWA, Zemax		

Interests

Video making	Realization of short movies
Sports	Climbing, sailing (D licence)

Extra

- Committee member (treasurer) of the Photonics Chapter of EPFL, organization of networking, socializing and outreach events within the optics community at EPFL

Publications

Peer-reviewed articles

[1] SMOLIK, Grégoire M. ; HERZIG, Hans P.: Binary zero-order diffractive and anti-reflective optical elements in silicon for the mid-infrared. In: *Optics Letters* 42 (2017), August, Nr. 16, 3233–3235. `http://dx.doi.org/10.1364/OL.42.003233`. – DOI 10.1364/OL.42.003233. – ISSN 1539–4794

[2] CADARSO, J. V. ; SMOLIK, Grégoire ; AUZELYTE, Vaida ; JACOT-DESCOMBES, Loïc ; BRUGGER, Jürgen: Heterogeneous material micro-transfer by ink-jet print assisted mould filling. In: *Microelectronic Engineering* 98 (2012), 619–622. `http://dx.doi.org/10.1016/j.mee.2012.04.025`. – DOI 10.1016/j.mee.2012.04.025

Conference proceedings

[1] SMOLIK, G. ; HERZIG, H. P.: Binary subwavelength structures that act simultaneously as antireflective and diffractive structure for the mid-infrared wavelength range, 2016

[2] SMOLIK, Grégoire M. ; HVOZDARA, Lubos ; DI FRANCESCO, Joab ; JOUY, P. ; BONETTI, Y. ; HANS, K. ; SIGRIST, W. ; HERZIG, Hans P.: Cocaine detection in liquid using a fibred platform and mid-infrared quantum cascade laser, 2014. – ISBN 978–1–55752–820–9

[3] BUSTO, Cadarso ; JAVIER, Victor ; SMOLIK, Grégoire ; AUZELYTE, Vaida ; JACOT-DESCOMBES, Loïc ; BRUGGER, Jürgen: Ink-jet printing assisted micro-transfer moulding, 2011

[4] FORD, Joseph E. ; ARIANPOUR, Ashkan ; SCHUSTER, Glenn ; STAMENOV, Igor ; GROISMAN, Alex ; LEGERTON, Jerry ; ZHANG, Arthur ; COOKSON, Scott ; MEYERS, William ; ALONSO, Goretty ; CUMMINGS, Joshua ; SKAW, Isaac ; SMOLIK, Gregoire ; TREMBLAY, Eric: Telescopic Contact Lenses and the Fiber-Coupled Scale Model Eye. In: *Classical Optics 2014 (2014), paper IW4A.1*, Optical Society of America, Juni 2014, IW4A.1